



Technical University of Munich
School of Engineering and Design
Deutsches Geodätisches Forschungsinstitut (DGFI-TUM)
Prof. Dr.-Ing. habil. Florian Seitz

Impact of refined geophysical models on orbits of altimetry satellites

Alkahal, Riva

Master's Thesis

Study program ESPACE - Earth Oriented Space Science and Technology

Supervisor(s) Dr. Sergei Rudenko
M.Sc. Julian Zeitlhöfler
Prof. Dr.-Ing. habil. Florian Seitz
Deutsches Geodätisches Forschungsinstitut (DGFI-TUM)
Technical University of Munich

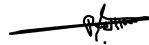
May 05, 2023

Declaration of Authorship

I confirm that this Master's thesis is my own work and I have documented all sources and material used.

This thesis was not previously presented to another examination board and has not been published.

Munich, 05/05/2023

A handwritten signature in black ink, consisting of a stylized, cursive script that is difficult to decipher but appears to be a personal name.

Location, Date, Signature

Abstract

Since global and regional sea level changes are important indicators of climate change, acquiring sea surface height measurements with utmost accuracy is crucial as reliable information for scientists and policymakers. Altimetry satellites are a valuable advancement in the space segment for providing such measurements and understanding climate change. Increasing the orbit accuracy of altimetry satellites, specifically in the radial direction, is one step towards achieving highly accurate sea level measurements. To investigate the current accuracy of altimetry satellite orbits, many factors should be considered to compare the various orbit solutions, such as the reference frames, the time systems, the step size of the time instants, the data gaps, and others. In the scope of this study, orbit analysis techniques and new background models are investigated with their impact on orbits of TOPEX/Poseidon and Jason-1/-2/-3 satellite missions covering the period from September 1992 to October 2021. Firstly, different interpolation methods for the comparison of satellite coordinates are studied. Among the Lagrange, Newton, spline, and Hermite interpolation methods, the latter provides the best accuracy of 0.3 mm in the radial direction, whereas, the fastest method is the spline interpolation method. Secondly, spectral analysis methods, such as Fourier transform, Lomb-Scargle periodogram, and wavelet transform, are examined for determining the prominent orbit frequencies and amplitudes in cases where there are gaps and noise. Since the Lomb-Scargle periodogram was designed for the purpose of irregularly sampled data, it provides better accuracy than the Fourier transform and wavelet transform methods. However, the Fourier transform is the fastest among the other tested methods. On the other hand, the wavelet transform is a powerful tool to detect signals that are changing in time. Finally, the impact of new background models on the orbits is investigated. The new thermospheric density model (NRLMSIS 2.0) is compared to the older version (NRLMSISE-00). Both models show a similar impact on the orbit parameters of the Jason satellites, with less than 1 mm difference of orbit coordinates in the radial direction. The new RL05 release of the Earth's mean gravity field model by the Centre National D'Etudes Spatiales (CNES) and the Groupe de Recherche de Géodésie Spatiale (GRGS) shows a 2% improvement in the root mean square fits of satellite laser ranging observations of Jason-3 satellite over the previous RL04 release. The differences in the orbits computed with the 2 models reach up to 1 cm for the investigated time span.

Contents

List of Figures	IV
List of Tables	XI
1 Introduction	1
2 Literature review	3
2.1 Precise orbit determination	3
2.2 Satellite tracking techniques.....	3
2.2.1 Satellite Laser Ranging (SLR).....	3
2.2.2 Doppler Orbitography and Radiopositioning Integrated by Satellite (DORIS)	5
2.3 Reference systems and frames	5
2.4 Force model.....	6
2.4.1 Gravitational forces.....	7
2.4.1.1 Acceleration due to geopotential	7
2.4.1.2 Acceleration due to other celestial objects (Sun and Moon)	9
2.4.1.3 Acceleration due to solid Earth tides and ocean tides.....	10
2.4.2 Non-gravitational forces.....	11
2.4.2.1 Acceleration due to atmospheric drag	11
2.4.2.2 Acceleration due to radiation pressure	12
2.4.3 Relativistic effects and other perturbations.....	13
3 Investigation on the optimal method for satellite coordinate interpolation	14
3.1 Numerical interpolation methods	14
3.1.1 Lagrange interpolation	14
3.1.2 Newton interpolation	15
3.1.3 Trigonometric interpolation.....	16
3.1.4 Hermite interpolation.....	16
3.1.5 Spline interpolation	17
3.1.6 Runge phenomenon	17
3.2 Interpolation methods analysis	18
3.2.1 1-second orbit interpolation.....	18
3.2.1.1 Scenario 1: step size of 30 seconds	19
3.2.1.2 Scenario 2: step size of 60 seconds	21
3.2.1.3 Scenario 3: step size of 120 seconds.....	25
3.2.2 Comparison of interpolation methods.....	30
3.2.2.1 Sliding window interpolation approach	30
3.2.2.2 Middle-point interpolation approach	38
4 Analysis of orbit differences.....	41
4.1 Program for orbit comparison of altimetry satellites	41
4.2 Spectral analysis	42
4.2.1 Fourier transform.....	42
4.2.2 Lomb-Scargle periodogram	43

4.2.3	Wavelet analysis	44
4.2.4	Testing the methods on an artificial signal.....	45
5	The impact of new background models on POD.....	57
5.1	The DGFI Orbit and Geodetic Parameter Estimation Software - Orbit Computation library.....	57
5.2	Thermospheric density models.....	57
5.2.1	Overview on the NRLMSISE-00 and NRLMSIS 2.0 thermospheric density models.....	58
5.2.2	Overview on estimated orbit parameters.....	59
5.2.3	Investigation on the estimation of empirical accelerations in the transverse component	61
5.2.4	Comparison of the NRLMSISE-00 and NRLMSIS 2.0 thermospheric density models.....	67
5.3	Earth's gravity field models	76
5.3.1	Overview on the EIGEN-GRGS.RL04.MEAN-FIELD and CNES_GRGS.RL05MF_-combined_GRACE_SLR_DORIS gravity field models	76
5.3.2	Comparison of orbit parameters obtained using EIGEN-GRGS.RL04.MEAN-FIELD and CNES_GRGS.RL05MF_-combined_GRACE_SLR_DORIS gravity field models	77
6	Conclusions	89
	List of Abbreviations	92
	Bibliography	94

List of Figures

Figure 1	Geometrical outline in Satellite Laser Ranging (Figure from Seeber 2003).	4
Figure 2	Satellite orbit and forces (f_1) due to a perturbing body (Figure from Hugentobler 2020).	10
Figure 3	The geometry of satellite in shadow (Figure from Montenbruck and Gill 2000).	13
Figure 4	Orbit differences when interpolating a 30-second solution to a 1-second solution using Newton interpolation method of order 5 (left: full interval, right: middle interval) in the TAI system.	19
Figure 5	Orbit differences when interpolating a 30-second solution to a 1-second solution using Newton interpolation method of order 6 (left: full interval, right: middle interval) in the TAI system.	20
Figure 6	Orbit differences when interpolating a 30-second solution to a 1-second solution using Newton interpolation method of order 7 (left: full interval, right: middle interval) in the TAI system.	20
Figure 7	Orbit differences when interpolating a 30-second solution to a 1-second solution using Newton interpolation method of order 8 (left: full interval, right: middle interval) in the TAI system.	21
Figure 8	Orbit differences when interpolating a 30-second solution to a 1-second solution using Newton interpolation method of order 9 (left: full interval, right: middle interval) in the TAI system.	21
Figure 9	Orbit differences when interpolating a 60-second solution to a 1-second solution using Newton interpolation method of order 5 (left: full interval, right: middle interval) in the TAI system.	23
Figure 10	Orbit differences when interpolating a 60-second solution to a 1-second solution using Newton interpolation method of order 6 (left: full interval, right: middle interval) in the TAI system.	23
Figure 11	Orbit differences when interpolating a 60-second solution to a 1-second solution using Newton interpolation method of order 7 (left: full interval, right: middle interval) in the TAI system.	24

Figure 12 Orbit differences when interpolating a 60-second solution to a 1-second solution using Newton interpolation method of order 8 (left: full interval, right: middle interval) in the TAI system. 24

Figure 13 Orbit differences when interpolating a 60-second solution to a 1-second solution using Newton interpolation method of order 9 (left: full interval, right: middle interval) in the TAI system. 25

Figure 14 Orbit differences when interpolating a 120-second solution to a 1-second solution using Newton interpolation method of order 5 (left: full interval, right: middle interval) in the TAI system. 26

Figure 15 Orbit differences when interpolating a 120-second solution to a 1-second solution using Newton interpolation method of order 6 (left: full interval, right: middle interval) in the TAI system. 26

Figure 16 Orbit differences when interpolating a 120-second solution to a 1-second solution using Newton interpolation method of order 7 (left: full interval, right: middle interval) in the TAI system. 27

Figure 17 Orbit differences when interpolating a 120-second solution to a 1-second solution using Newton interpolation method of order 8 (left: full interval, right: middle interval) in the TAI system. 27

Figure 18 Orbit differences when interpolating a 120-second solution to a 1-second solution using Newton interpolation method of order 9 (left: full interval, right: middle interval) in the TAI system. 28

Figure 19 Sliding window approach, 5th order interpolation. 30

Figure 20 Sliding window approach, 6th order interpolation. 31

Figure 21 (Left axis) 8th order Hermite interpolation error in the Cartesian coordinates. (Right axis) TOPEX/Poseidon orbit in the Cartesian coordinates. 34

Figure 22 (Left axis) 8th order Hermite interpolation error in the RTN coordinates. (Right axis) TOPEX/Poseidon orbit in the Cartesian coordinates. 34

Figure 23 (Left axis) 5th order Lagrange interpolation error in the Cartesian coordinates. (Right axis) TOPEX/Poseidon orbit in the Cartesian coordinates. 35

Figure 24 (Left axis) 5th order Lagrange interpolation error in the RTN coordinates. (Right axis) TOPEX/Poseidon orbit in the Cartesian coordinates. 35

Figure 25 (Left axis) 7th order Lagrange interpolation error in the Cartesian coordinates. (Right axis) TOPEX/Poseidon orbit in the Cartesian coordinates.	36
Figure 26 (Left axis) 7th order Lagrange interpolation error in the RTN coordinates. (Right axis) TOPEX/Poseidon orbit in the Cartesian coordinates.	36
Figure 27 Lagrange interpolation of order 5, interpolation error in the radial component with the orbit function in the Cartesian coordinates (left). Interpolation error in the radial component with interpolation error in the Cartesian coordinates (right).	37
Figure 28 Lagrange interpolation of order 5, interpolation error in the radial component with the orbit function in the Cartesian coordinates (left). Interpolation error in the radial component with interpolation error in the Cartesian coordinates (right).	37
Figure 29 Middle-point interpolation concept.	38
Figure 30 Detection accuracy of a period of 58.765 days in a gap-free and noise-free sine signal depending on the signal lengths in days using Lomb-Scargle method (plomb on the left), standard fast Fourier transform (middle), and zero-padding fast Fourier transform (right).	48
Figure 31 Detection accuracy of an amplitude of 10 in a gap-free and noise-free sine signal depending on the signal lengths in days using Lomb-Scargle method (left), stan- dard fast Fourier transform (middle), and zero-padding fast Fourier transform (right).	49
Figure 32 Detection accuracy of a period of 9,9156 days in a gap-free and noise-free sine signal depending on the signal lengths in days using Lomb-Scargle method (left), standard fast Fourier transform (middle), and zero-padding fast Fourier transform (right).	49
Figure 33 Detection accuracy of an amplitude of 50 in a gap-free and noise-free sine signal depending on the signal lengths in days using Lomb-Scargle method (left), stan- dard fast Fourier transform (middle), and zero-padding fast Fourier transform (right).	49
Figure 34 Detection accuracy of a period of 0.078075 days in a gap-free and noise-free sine signal depending on the signal lengths in days using Lomb-Scargle method (left), standard fast Fourier transform (middle), and zero-padding fast Fourier transform (right).	50
Figure 35 Detection accuracy of an amplitude of 5 in a gap-free and noise-free sine signal de- pending on the signal lengths in days using Lomb-Scargle method (left), standard fast Fourier transform (middle), and zero-padding fast Fourier transform (right).	50

Figure 36 Detection accuracy of a period of 58.765 days in a sine signal with gaps and noise depending on the signal lengths in days using Lomb-Scargle method (left), standard fast Fourier transform (middle), and zero-padding fast Fourier transform (right). 52

Figure 37 Detection accuracy of an amplitude of 10 in a sine signal with gaps and noise depending on the signal lengths in days using Lomb-Scargle method (left), standard fast Fourier transform (middle), and zero-padding fast Fourier transform (right)..... 53

Figure 38 Detection accuracy of a period of 9.9156 days in a sine signal with gaps and noise depending on the signal lengths in days using Lomb-Scargle method (left), standard fast Fourier transform (middle), and zero-padding fast Fourier transform (right). 53

Figure 39 Detection accuracy of an amplitude of 50 in a sine signal with gaps and noise depending on the signal lengths in days using Lomb-Scargle method (left), standard fast Fourier transform (middle), and zero-padding fast Fourier transform (right)..... 53

Figure 40 Detection accuracy of a period of 0.078075 days in a sine signal with gaps and noise depending on the signal lengths in days using Lomb-Scargle method (left), standard fast Fourier transform (middle), and zero-padding fast Fourier transform (right). 54

Figure 41 Detection accuracy of an amplitude of 5 in a sine signal with gaps and noise depending on the signal lengths in days using Lomb-Scargle method (plomb on the left), standard fast Fourier transform (middle), and zero-padding fast Fourier transform (right). 54

Figure 42 3-year-long signal containing gaps and noise, with frequencies detected using wavelet transform illustrated along the time series (Note: magnitude = amplitude in this context). 56

Figure 43 Mean of the absolute values of the correlation coefficients over 343 arcs. 59

Figure 44 SLR RMS fit of Jason-2 orbit solutions computed using the models and SLR observations. 64

Figure 45 Atmospheric drag scale factor and its a posteriori standard deviation (Sigma) for Jason-2 orbit solutions..... 64

Figure 46 Earth albedo scale factor and its a posteriori standard deviation (Sigma) for Jason-2 orbit solutions. 65

Figure 47 Solar radiation scale factor and its a posteriori standard deviation (Sigma) for Jason-2 orbit solutions. 65

Figure 48	The amplitude of the cosine term of empirical acceleration in the normal direction and its a posteriori standard deviation (Sigma) for Jason-2 orbit solutions.	66
Figure 49	Empirical acceleration polygon terms in the normal direction and their a posteriori standard deviations (Sigma) for Jason-2 orbit solutions.....	66
Figure 50	Standard deviations of orbit differences of the 3 cases of not estimating the transverse component against estimating it over the whole time span of the mission. (Top) The impact on the radial component, (middle) the impact on the transverse component, (bottom) the impact on the normal component.	67
Figure 51	Atmospheric densities obtained from NRLMSISE-00 and NRLMSIS 2.0 thermospheric density models overlaid with solar flux index (top) and their differences (bottom).....	68
Figure 52	SLR RMS fit of Jason-2 orbits (left) and their differences (right) derived using the NRLMSISE-00 and NRLMSIS 2.0 thermospheric density models.....	69
Figure 53	Atmospheric drag scale factor and its a posteriori standard deviation (Sigma) for Jason-2 orbits (left) and their differences (right) derived using the NRLMSISE-00 and NRLMSIS 2.0 thermospheric density models.	70
Figure 54	Mount Stromlo SLR station range biases (left) and their differences (right) derived for Jason-2 orbits using the NRLMSISE-00 and NRLMSIS 2.0 thermospheric density models.....	71
Figure 55	Semimajor axis of Jason-2 orbits computed using the NRLMSISE-00 and NRLMSIS 2.0 thermospheric density models (left) and their differences (right).	72
Figure 56	Eccentricity of Jason-2 orbits computed using the NRLMSISE-00 and NRLMSIS 2.0 thermospheric density models (left) and their differences (right).....	73
Figure 57	Inclination of Jason-2 orbits computed using the NRLMSISE-00 and NRLMSIS 2.0 thermospheric density models (left) and their differences (right).....	74
Figure 58	Argument of perigee of Jason-2 orbits computed using the NRLMSISE-00 and NRLMSIS 2.0 thermospheric density models (left) and their differences (right).	74
Figure 59	Longitude of ascending node of Jason-2 orbits computed using the NRLMSISE-00 and NRLMSIS 2.0 thermospheric density models (left) and their differences (right). .	74
Figure 60	Mean anomaly of Jason-2 orbits computed using the NRLMSISE-00 and NRLMSIS 2.0 thermospheric density models (left) and their differences (right).	75

Figure 61 SLR RMS fits of TOPEX/Poseidon orbits (left) and their differences (right) derived using the EIGEN-GRGS.RL04 and CNES_GRGS.RL05 gravity field models. 78

Figure 62 SLR RMS fits of Jason-1 orbits (left) and their differences (right) derived using the EIGEN-GRGS.RL04 and CNES_GRGS.RL05 gravity field models. 79

Figure 63 SLR RMS fits of Jason-2 orbits (left) and their differences (right) derived using the EIGEN-GRGS.RL04 and CNES_GRGS.RL05 gravity field models. 80

Figure 64 SLR RMS fits of Jason-3 orbits (left) and their differences (right) derived using the EIGEN-GRGS.RL04 and CNES_GRGS.RL05 gravity field models. 81

Figure 65 Empirical acceleration: amplitude of the normal sine term and its a posteriori standard deviation of TOPEX/Poseidon orbit (left) and Jason-1 orbit (right) derived using the EIGEN-GRGS.RL04 and CNES_GRGS.RL05 gravity field models..... 82

Figure 66 Yarragadee SLR station range biases (left) and their differences (right) derived for TOPEX/Poseidon orbits using the EIGEN-GRGS.RL04 and CNES_GRGS.RL05 gravity field models. 82

Figure 67 Yarragadee SLR station range biases (left) and their differences (right) derived for Jason-1 orbits using the EIGEN-GRGS.RL04 and CNES_GRGS.RL05 gravity field models. 83

Figure 68 Yarragadee SLR station range biases (left) and their differences (right) derived for Jason-2 orbits using the EIGEN-GRGS.RL04 and CNES_GRGS.RL05 gravity field models. 83

Figure 69 Yarragadee SLR station range biases (left) and their differences (right) derived for Jason-3 orbits using the EIGEN-GRGS.RL04 and CNES_GRGS.RL05 gravity field models. 83

Figure 70 Standard deviations of orbit differences in the radial direction of TOPEX/Poseidon (left) and Jason-1 (right) satellites. 84

Figure 71 Standard deviations of orbit differences in the radial direction of Jason-2 (left) and Jason-3 (right) satellites..... 84

Figure 72 Geographical distribution of orbit differences in the radial direction of TOPEX/Poseidon (left) and Jason-1 (right) satellites averaged over a $1^\circ \times 1^\circ$ grid of latitude and longitude. 85

Figure 73 Geographical distribution of orbit differences in the radial direction of Jason-2 (left) and Jason-3 (right) satellites averaged over a $1^\circ \times 1^\circ$ grid of latitude and longitude. 85

Figure 74	Magnitude scalogram of the wavelet transform over the time span between 2002.7 and 2005.8 of the TOPEX/Poseidon (left) and Jason-1 (right) orbit differences.....	86
Figure 75	Magnitude scalogram of the wavelet transform over the time span between 2016.5 and 2019.8 of the Jason-2 (left) and Jason-3 (right) orbit differences.	86
Figure 76	Radial orbit differences (top) of TOPEX/Poseidon (left) and Jason-1 (right) and their spectral analysis results using the Lomb-Scargle periodogram (bottom).	87
Figure 77	Radial orbit differences (top) of Jason-2 (left) and Jason-3 (right) and their spectral analysis results using the Lomb-Scargle periodogram (bottom).	87

List of Tables

Table 1	Orders 5 to 9, standard deviations and means of orbit differences when interpolating 30, 60, and 120-second step size solutions to the 1-second solution. FI: Full interval, MI: Middle interval, SS: Step size. All values are in mm.....	29
Table 2	Interpolation statistics using Lagrange interpolation method of different orders with the sliding window approach.	32
Table 3	Interpolation statistics using Newton interpolation method of different orders with the sliding window approach.	33
Table 4	Interpolation statistics using Hermite interpolation method of different orders with the sliding window approach.	33
Table 5	Interpolation statistics using Lagrange interpolation method of different orders with the sliding window and the middle-point approaches.....	39
Table 6	Interpolation statistics using Newton interpolation method of different orders with the sliding window and the middle-point approaches.	39
Table 7	Interpolation statistics using Hermite interpolation method of different orders with the sliding window and the middle-point approaches.....	40
Table 8	Interpolation statistics using spline interpolation with and without the middle-point (MP) approach.....	40
Table 9	Detection accuracy of specific periods in a gap-free and noise-free sine signal depending on the signal lengths in days. In bold are the values of minimum absolute relative differences.	47
Table 10	Detection accuracy of specific amplitudes in a gap-free and noise-free sine signal depending on the signal lengths in days. In bold are the values of minimum absolute relative differences.	48
Table 11	Detection accuracy of specific periods in a sine signal with gaps and noise depending on the signal lengths in days. In bold are the values of minimum absolute relative differences.....	51
Table 12	Detection accuracy of specific amplitudes in a sine signal with gaps and noise depending on the signal lengths in days. In bold are the values of minimum absolute relative differences.	52

Table 13 Comparison of the Lomb-Scargle method (Plomb) with the wavelet transform method, detecting 4 different frequencies on a 3-year-long signal.	55
Table 14 Estimated orbit parameters.....	58
Table 15 Force models used for POD.....	60
Table 16 Comparison of POD parameters of 4 Jason-2 orbits computed for NRLMSISE-00 and estimating the empirical acceleration in the transverse direction (T) versus not estimating the polygons, not estimating the periodic terms, or not estimating both terms.	63
Table 17 Comparison of POD parameters of 2 TOPEX/Poseidon orbits computed for NRLMSISE-00 versus NRLMSIS 2.0.....	70
Table 18 Comparison of POD parameters of 2 Jason-1 orbits computed for NRLMSISE-00 versus NRLMSIS 2.0.	71
Table 19 Comparison of POD parameters of 2 Jason-2 orbit solutions computed for NRLMSISE-00 versus NRLMSIS 2.0.....	72
Table 20 Comparison of POD parameters of the 2 Jason-3 orbit solutions computed for NRLMSISE-00 versus NRLMSIS 2.0.....	73
Table 21 Comparison of POD parameters of 2 TOPEX/Poseidon orbit solutions computed using EIGEN-GRGS.RL04 vs CNES_GRGS.RL05	78
Table 22 Comparison of POD parameters of 2 Jason-1 orbit solutions computed using EIGEN-GRGS.RL04 vs CNES_GRGS.RL05.....	79
Table 23 Comparison of POD parameters of 2 Jason-2 orbit solutions computed using EIGEN-GRGS.RL04 vs CNES_GRGS.RL05.....	80
Table 24 Comparison of POD parameters of 2 Jason-3 orbit solutions computed using EIGEN-GRGS.RL04 vs CNES_GRGS.RL05.....	81

1. Introduction

Climate change is one of the biggest societal, economic, and environmental concerns that are detrimental to the future of humanity. The Global Climate Observing System (GCOS) was established as an outcome of the second World Climate Conference that took place in 1990. It is responsible for observations related to climate change and regularly delivers guidelines for its enhancement¹. GCOS has identified Essential Climate Variables (ECVs), which consist of 3 main domains, atmospheric, oceanic, and terrestrial domains, that include 54 different ECVs. Under the oceanic domain lies the ECV “sea level”. Accurate monitoring of sea level is crucial to understand its global and regional variations.

Since 1975, altimetric measurements tests from space have been initialized with the launch of Geodynamic Experimental Ocean Satellite 3 (GEOS 3) by the National Aeronautics and Space Administration (NASA) followed by the Seasat mission in 1978 (Stammer and Cazenave, 2017). However, reliable results with very high precision were not obtained until the early 1990s with the European Remote Sensing-1 (ERS-1) satellite and Topography Experiment (TOPEX)/Poseidon mission. TOPEX/Poseidon had a fifth-generation altimeter equipped with a C-band (5.3 GHz) channel specified for ionospheric measurements. Combining the C-band with Ku-band (13.6 GHz), the mission was able to deliver an improved quality of sea level height measurement, as well as to provide wind speed, ionospheric correction, and significant wave height². Furthermore, it was the first altimetry mission to carry Doppler Orbitography and Radiopositioning Integrated by Satellite (DORIS) receiver, which led to an improved orbit determination. The 3-band microwave radiometer for measuring the atmospheric water vapor, as well as the progress in modeling of the incoming signal, noise, and biases, allowed TOPEX/Poseidon and its successor missions to deliver sea level measurements with an accuracy of 2-3 cm and higher (Seeber, 2003), compared to the accuracy of the early age missions (GEOS 3, Seasat, and GEOSAT) that was around 100 cm (Stammer and Cazenave, 2017).

Satellite altimeters measure the range between the sea surface and the satellite. Therefore, in order to obtain the sea surface height, precise knowledge of the position, specifically, the altitude of the satellite, is essential to achieve high-accuracy measurements. Recent altimetry missions, starting from TOPEX/Poseidon, to Sentinel-6A, carry Global Navigation Satellite System (GNSS) receivers, Satellite Laser Ranging (SLR) retroreflector arrays and DORIS receivers for Precise Orbit Determination (POD). There are other positioning techniques, such as Precise Range and Range Rate Equipment (PRARE) which was used by ERS-2 mission, and the Tracking and Data Relay Satellite System (TDRSS), which was used by TOPEX/Poseidon (Montenbruck and Gill, 2000).

In addition, perturbing forces acting on the center of mass of the satellites, i.e. gravitational forces, and on the surface of the satellites, i.e. non-gravitational forces, should be taken into account to

¹ <https://gcos.wmo.int/en/about>

² <http://www.altimetry.info/missions/past-missions/topexposeidon/tp-instruments/topex-altimeter-or-nra/>

present precise orbits with reduced errors. Therefore, accurate modeling of dynamic forces should always be a top priority in POD (Wu et al., 1991). Today, new models are being developed, such as realizations of the International Terrestrial Reference System (ITRS), Earth's gravity field models, ocean tides, and atmospheric models. In this thesis, the newest models will be used in the POD of altimetry satellites together with SLR observations using a software developed at Deutsches Geodätisches Forschungsinstitut (DGFI-TUM) called: the DGFI Orbit and Geodetic Parameter Estimation Software - Orbit Computation library (DOGS-OC). Specifically, the new thermospheric density model (NRLMSIS 2.0; Emmert et al. 2021) will be compared to the older version (NRLMSISE-00; Picone et al. 2002), the Mass Spectrometer Incoherent Scatter (MSIS) radar series which were developed at the Naval Research Laboratory (NRL) (Picone et al., 2002). Furthermore, a new release of the mean Earth's gravity field EIGEN-GRGS.RL04.MEAN-FIELD has been developed at the Centre National D'Etudes Spatiales (CNES) and the Groupe de Recherche de Géodésie Spatiale (GRGS) called the CNES_GRGS.RL05MF_combined_GRACE_SLR_DORIS. The 2 Earth's gravity field models will also be analyzed. The models will be compared by computing 2 altimetry satellite orbits with each model (2 thermospheric density models and Earth's gravity models). Comparing different orbit solutions requires each solution to have common time instants. Therefore, interpolation of the orbit is necessary to perform the comparison. Spline, Newton, Lagrange, trigonometric, and Hermite interpolation methods are used in literature for Global Positioning System (GPS) orbit interpolation (Neta et al., 1996; Yousif and El-Rabbany, 2007; Wang et al., 2018). One of the main tasks is the investigation of an appropriate interpolation method in order to find the highest precision method that will least influence the analysis and provide optimal results. The orbit comparison analysis is done using a MATLAB program developed at the DGFI-TUM, described in Section 4.1. The obtained orbit differences are then analyzed over the entire mission time span using spectral analysis methods to determine the discrepancies between the current models. Spectral analysis methods, such as Fourier transform, Lomb-Scargle periodogram, and wavelet transform, are discussed in detail and assessed in terms of accuracy and efficiency.

The structure of the thesis will be as follows: first, the state of art of orbit determination methods, reference systems, tracking techniques, and background models is discussed in Chapter 2. Then, different interpolation methods are evaluated in Chapter 3. After that, spectral analysis methods and their assessment are discussed in Chapter 4. Finally, the impact of the new background models on the orbits of altimetry satellites is examined in Chapter 5, and the conclusions are given in Chapter 6.

2. Literature review

2.1. Precise orbit determination

Precise knowledge of the altitude of a satellite altimeter is critical for its essential performance, which is measuring sea level height. In 1994, the error budget for the TOPEX/Poseidon satellite was set to 12.5 cm, however, with the rapid progress of POD, this accuracy has been reduced to 2 cm. Higher standards were expected for Jason-1, the successor to TOPEX/Poseidon satellite mission. In 2003, a 1 cm radial orbit error was achieved using GPS data (Luthcke et al., 2003). As mentioned earlier, there are several tracking techniques that are mainly used in the POD of altimetry satellites, based on the size of the ground network, as well as the preference of analysis centers to process data from these techniques.

Realization of the International Terrestrial Reference System (ITRS) depends on the combination of the observations from all of the 3 techniques, SLR, DORIS, and GNSS, in addition to another technique which will not be discussed in the course of this work, the Very Long Baseline Interferometry (VLBI). Orbit determination directly from the observation system is called kinematic orbit determination. With this method, the satellite position is obtained at each measurement epoch. On the other hand, dynamic orbit determination considers the perturbing forces acting on the satellite. In order to obtain the satellite position, numerical integration of the equations of motion is required. The main difference between the 2 methods lies in the number of parameters to be estimated in the process. As the dynamic orbit determination relies on a limited number of unknowns, i.e. the dynamic parameters to be estimated as well as the initial position of the satellite, the kinematic method estimates a new position at each epoch. Therefore, the number of parameters to be estimated is much larger. Another method is called reduced dynamic orbit determination. This method is a combination of kinematic and dynamic methods, where the initial position of the satellite is unknown, and dynamic parameters are considered. It allows a stochastic component to be involved, and the parameters to be estimated are unlimited and may vary depending on the problem (Beutler, 2005). This method takes advantage of the 2 other methods and helps in overcoming the deficiencies in the force models. For more information about reduced dynamic orbit determination of Low Earth Orbit (LEO) satellites, see Arnold et al. (2019).

2.2. Satellite tracking techniques

2.2.1. Satellite Laser Ranging (SLR)

Since the introduction of SLR in 1964, it was the first technique used for POD of altimetry satellites (Stammer and Cazenave, 2017). It is based on measuring the two-way flight time of short laser pulses of 532 nm wavelength between the ground station and the satellite's retroreflector arrays (Eq. 2.1), and from there, the range d is computed.

$$d = \frac{1}{2} \Delta t c, \quad (2.1)$$

where Δt is the time travel of the signal, and c is the speed of light.

SLR is a vital technique for geodetic applications, such as the determination of Earth Orientation Parameters (EOP), and hence, for the realization of the ITRS. Despite having an essential role in POD, the limitation of using solely SLR for POD is the inhomogeneous distribution of its network. A precise orbit is also dependent on the precise knowledge of the station coordinates, as well as clear weather for an accurate measurement (Montenbruck and Gill, 2000). However, it is more sensitive than DORIS when comparing POD background models. Furthermore, the number of observing sites and observations in an orbital arc are much lower than of DORIS, i.e. less computation time is required. Therefore, using SLR-only orbits is suitable for the aim of this study. There are additional parameters and corrections that should be introduced to the ranging equation (Eq. 2.2) to fulfill the simple model shown in Figure 1.

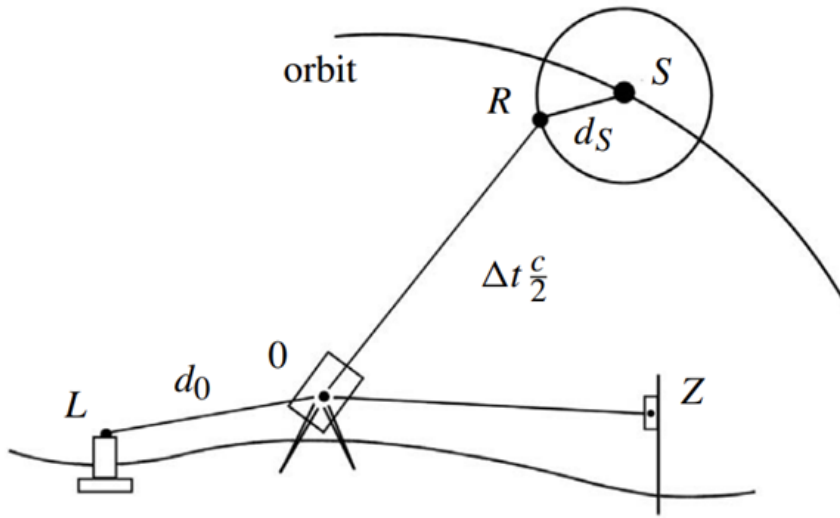


Figure 1: Geometrical outline in Satellite Laser Ranging (Figure from Seeber 2003).

The following equation reads,

$$d = \frac{1}{2} \Delta t c + \Delta d_0 + \Delta d_s + \Delta d_b + \Delta d_r + \eta, \quad (2.2)$$

where Δd_0 is the offset between the station marker and the position of the telescope, it is often known as the eccentricity.

Δd_s is the offset between the satellite's center of mass and the optical center of the retroreflector.

Δd_b is the signal delay at the ground station. The geometric reference point "0" on the telescope can be different from the electric zero point of the measurement. Therefore, it is calibrated to a known target (Z) for older systems, and new systems are calibrated from inside the laser system.

Δd_r is the atmospheric delay. The correction is applied using predefined atmospheric models.

Finally, η is defined as a combination of other systematic and random errors.

In theory, the above-mentioned corrections should be at least with an accuracy of one order of magnitude higher than the required accuracy of the measurement (Seeber, 2003).

2.2.2. Doppler Orbitography and Radiopositioning Integrated by Satellite (DORIS)

DORIS uses microwave signals directed from the ground station to the satellite, with the Doppler effect, the frequency is highest when the satellite is at the closest point to the ground station (directly above the station) where the distance between the satellite and the station can be computed. The first altimetry mission, which had a DORIS antenna onboard, was TOPEX/Poseidon, followed by Jason-1, Envisat, and others (Tavernier et al., 2006). The main objective of the technique is POD. The technique has taken an important role in other geodetic and geophysical applications, such as tracking the Earth's crust and determining the geocenter motion and polar motion. Thanks to the global homogeneous station distribution, DORIS plays a significant role in the realization of the ITRS. Given the good distribution of the network, firstly, it is active under any weather condition. Secondly, it allows a reduced-dynamic orbit determination; with accurate dynamic models, a precise orbit can be achieved (Willis et al., 2006). DORIS orbits are more sensitive in the along-track component, where the time tag offset is mostly dominant, unlike SLR orbits which are most sensitive in the radial component (Willis et al., 2006). The satellite receiver is equipped with an ultra-stable oscillator (USO) with stability of 5×10^{-13} Hz over a period of 10-100 s (Jayles et al., 2006).

2.3. Reference systems and frames

Terrestrial reference frames are realizations of the terrestrial reference system conceptualized by the International Earth Rotation and Reference Systems Service (IERS) by defining the origin, orientation, scale, and time evolution. The origin is the center of mass of the Earth, also known as the geocenter. The orientation is that of the 3-dimensional, orthogonal, and right-handed vector space, defined by the Bureau International de l'Heure (BIH) orientation at 1984.0. The scale is the common unit of length of the basis vector in meter (SI). A condition of a no-net-rotation with respect to horizontal tectonics motions over the Earth is applied to secure the evolution of the frame's orientation (Bloßfeld, 2015).

Since the first realization in 1988, observations from all 4 space geodetic techniques mentioned above were used for station positions and velocities (Petit and Luzum, 2010). Stations are in motion for many reasons, such as geophysical movements, instrumental deformations, or anthropogenic activities. This causes a non-linear change of station positions, and it is referred to as instantaneous station position ($\vec{X}(t_i)$). Station positions with regular variations are known as regularized ($\vec{X}_R(t_i)$) and can be obtained from the mean station position and velocity ($\vec{X}_{ITRF}, \vec{X}_{ITRF}$) at an epoch t_i

with respect to a reference epoch t_0 (Bloßfeld, 2015),

$$\vec{X}_R(t_i) = \vec{X}_{ITRF} + (t_i - t_0)\dot{\vec{X}}_{ITRF}, \quad (2.3)$$

then, $(\vec{X}(t_i))$ is obtained by adding n correction parameters $\Delta\vec{X}_n(t_i)$

$$\vec{X}(t_i) = \vec{X}_R(t_i) + \sum_n \Delta\vec{X}_n(t_i). \quad (2.4)$$

The correction parameters are modeled using geophysical tidal and non-tidal loading models, such as solid Earth tides, ocean tides, atmospheric pressure loading, ocean pole tidal loading, and mean pole motion predefined by the IERS conventions (Bloßfeld, 2015). The loading models were not applied to ITRF2008 because the models were not sufficiently examined, and full-time span data was not available (Seitz et al., 2012). The reference frames are recomputed every 3 to 5 years by 3 IERS Combination Centers: the Institute Nationale de l'Information Géographique et Forestière (IGN) in Paris, the DGFI-TUM in Munich, and the Jet Propulsion Laboratory (JPL) in Pasadena. Each Combination Center uses a different combination strategy, resulting in slightly different realizations.

As discussed before, POD comprises observations from SLR retroreflectors, DORIS, and GNSS receivers mounted on the satellite. Therefore, up-to-date station positions are crucial to obtain the desired accuracy, and hence, the most recent ITRS realization has to be used as a reference frame for the orbit determination solution. Furthermore, stability in the reference frame solutions in measuring the mean sea level change should be within 0.1 mm/y. It has been demonstrated that any shift in the Z component of the reference frame affects the satellite orbits (mean orbit error in Z component DZ) and the global mean sea level (GMSL). This is formulated by the function as in Couhert et al. (2015),

$$GMSL \text{ error} = -0.16 \cdot DZ. \quad (2.5)$$

Rudenko et al. (2018) studied the impact of the recent 3 different ITRS realizations on satellite orbits by computing SLR observation residuals. They found an improvement in the mean Root Mean Square (RMS) fit of SLR observations of up to 8.1% when using ITRS realizations in 2014 with Non-Tidal Loading (NTL), instead of realization for SLR stations in 2008 (SLRF2008). This can affect the global inter-annual mean sea level up to 4% of the sea level signal from satellite altimetry within a timescale of 3 to 8 years (Rudenko et al., 2019).

2.4. Force model

The general form of the differential equation of motion of a satellite orbiting the Earth can be expressed by Newton's law of gravity

$$\ddot{\vec{r}} = -\frac{GM}{r^3}\vec{r}, \quad (2.6)$$

where \vec{r} is the acceleration vector of the satellite, GM is the product of the gravitational constant and the mass of the Earth, r is the geocentric distance of the satellite, and \vec{r} is the geocentric position vector of the satellite. The previous equation is only valid theoretically, where the Earth is a homogeneous spherical object, and only the central gravitational force is acting on the satellite. Generally, this term is known as the two-body term. In real life, many perturbing forces affect the satellite motion and should be added as an acceleration to the differential equation above.

$$\vec{r} = \vec{r}_E + \vec{r}_S + \vec{r}_M + \vec{r}_e + \vec{r}_o + \vec{r}_D + \vec{r}_{SP} + \vec{r}_a + \vec{r}_r + \vec{r}_{others} \quad (2.7)$$

These are accelerations caused by

- Geopotential coefficients of the mass distribution within the Earth (\vec{r}_E).
- Surrounding celestial bodies, such as, Moon (\vec{r}_M), Sun (\vec{r}_S), and major planets of the solar system.
- Solid Earth tides (\vec{r}_e) and ocean tides (\vec{r}_o).
- Atmospheric drag (\vec{r}_D).
- Solar radiation pressure (\vec{r}_{SP}).
- Earth's albedo and Earth's infra-red radiation (\vec{r}_a).
- Relativistic effects (\vec{r}_r).
- To absorb unmodeled parameters, empirical parameters (\vec{r}_{others}) are introduced and estimated.

Perturbing forces are classified into gravitational and non-gravitational forces. In the following subsections, each of the above-mentioned forces will be described briefly.

2.4.1. Gravitational forces

2.4.1.1 Acceleration due to geopotential

In celestial mechanics, the acceleration can be expressed by the gradient of the potential U (Montenbruck and Gill, 2000),

$$\vec{r} = \nabla U. \quad (2.8)$$

As the Earth is non-spherical, the mass distribution is non-homogeneous. Hence, the point mass distribution within the Earth should be considered when studying the gravitational potential. The acceleration due to gravitational potential is represented in terms of the spherical harmonic expansion of Earth's gravity field,

$$\vec{r} = \nabla \frac{GM}{r} \sum_{n=0}^{\infty} \sum_{m=0}^n \frac{R^n}{r^n} \bar{P}_{nm}(\sin \phi) (\bar{C}_{nm} \cos m\lambda + \bar{S}_{nm} \sin m\lambda), \quad (2.9)$$

where R is the radius of the Earth, \bar{P}_{nm} is the normalized Legendre polynomial, \bar{C}_{nm} and \bar{S}_{nm} are normalized spherical harmonic coefficients with n and m being the degree and order, and ϕ and λ are the geocentric latitude and longitude of the satellite, (cf. Hofmann-Wellenhopf and Moritz (2006)). It is worth noting that each degree and order of spherical harmonic coefficients have a physical representation. The coefficient of degree 2 and order 0 is the commonly known Earth's oblateness. It has a major impact on the satellite orbits, which can reach up to kilometer level. Higher order terms have less influence on high-altitude satellites. However, they still have a high impact on LEO satellites.

Kaula (1966) first developed the perturbation theory of satellites orbiting the Earth and formulated the equation that relates between orbital Keplerian's elements and the perturbing parameters. Rosborough and Tapley (1987) presented the geopotential perturbations for the radial, transverse, and normal components of a satellite. An important milestone in developing the geopotential models was using a combination of terrestrial observations with laser and Doppler tracking and altimetry measurements, such as the model GEM-T3 (Lerch et al., 1992). After the launch of TOPEX/Poseidon satellite, an improved geopotential model based on tracking of the satellite by SLR, DORIS, and GPS systems was developed. This model is known as the JGM-3, and it was proven to have improved the accuracy of the TOPEX/Poseidon orbit (Tapley et al., 1996). In 2000, the Challenging Minisatellite Payload (CHAMP) satellite was launched. The mission aimed at magnetic field and static and temporal global gravity field recovery by having an accelerometer onboard to measure non-gravitational acceleration. In addition, the Earth's gravity field can be determined from a pure perturbation due to gravity by using satellite to satellite tracking technique (GPS-SST)¹. With data from CHAMP, LAser GEOdynamic Satellite (LAGEOS), and the french Satellite de Taille Adaptée avec Réflecteurs Laser pour les Études de la Terre (STARLETTE), the European Improved Gravity model of the Earth by New techniques (EIGEN) model was generated (Reigber et al., 2002). Afterwards, in 2002, the Gravity Recovery and Climate Experiment mission (GRACE) was launched (Tapley et al., 2004). This mission was dedicated solely to gravity field recovery by measuring the range rate with the K-band ranging system between the twin satellites. Higher resolution gravity field models were developed in addition to the 10-day time-variable gravity field models (Bruinsma et al., 2010). Another worth mentioning mission, which was launched in 2009, is the Gravity field and Ocean Circulation Explorer (GOCE) (Floberghagen et al., 2011). GOCE is the first mission which applied gravity recovery by gradiometric measurements. With GOCE, very high accurate geoid determination was achieved (1 cm geoid from global models) (Gruber and Willberg, 2019).

It has been found that time-variable gravity models have a significant role when studying the error budget of the radial component fit between CNES and JPL's GPS reduced-dynamic orbits (Cerrri et al., 2010). In a later study, the impact of the geopotential models on orbits of satellite altimetry has been studied with a comparison of static and time-variable gravity models (Rudenko et al., 2014). The study addressed the challenge of modeling the time variable gravity field in the period before GRACE mission, i.e. from 1985 to 2003. In conclusion, the EIGEN-6S2 model provided a lower SLR RMS of fits among other models in comparison (2.022 cm for TOPEX/Poseidon).

¹ <https://www.eoportal.org/satellite-missions/champstar-space-three-axis-accelerometer-for-research-mission>

Another study suggested that, in order to overcome the uncertainties and improve the extrapolation at the pre-GRACE era, a combination of cannon-ball satellites SLR measurements, together with DORIS measurements should be done (Esselborn et al., 2018). The recent releases of the EIGEN gravity field model, EIGEN-GRGS.RL04 and CNES_GRGS.RL05MF_combined_GRACE_SLR_DORIS, both include SLR measurements for extrapolating at the pre-GRACE era. The newest model, CNES_GRGS.RL05MF_combined_GRACE_SLR_DORIS, also includes DORIS observations (Lemoine et al., 2023). These 2 models will be compared in terms of their impact on the orbits of altimetry satellites in Section 5.3.

2.4.1.2 Acceleration due to other celestial objects (Sun and Moon)

The Sun and Moon cause a third-body gravitational perturbation in the satellite orbit. In an inertial system, the equation of motion is written as in Montenbruck and Gill (2000):

$$\ddot{\vec{r}} = GM_s \frac{\vec{s} - \vec{r}}{|\vec{s} - \vec{r}|^3}, \quad (2.10)$$

where M_s is the mass of the perturbing body, \vec{r} is the geocentric position of the satellite, and \vec{s} is the geocentric position of the body. The equation of motion in an Earth fixed frame reads

$$\ddot{\vec{r}} = GM_s \left(\frac{\vec{s} - \vec{r}}{|\vec{s} - \vec{r}|^3} - \frac{\vec{s}}{|\vec{s}|^3} \right). \quad (2.11)$$

Since the distance between the satellite and other celestial bodies is very large, the following approximation can be applied,

$$\frac{1}{|\vec{s} - \vec{r}|^3} = \left(\frac{1}{s^2 + r^2 - 2rs \cos \psi} \right)^{\frac{3}{2}} \approx \frac{1}{s^3} \left(1 + 3 \frac{r}{s} \cos \psi \right) + O\left(\frac{r^2}{s^2}\right), \quad (2.12)$$

with ψ is the angle between \vec{r} and \vec{s} .

The acceleration then reads,

$$\ddot{\vec{r}} \approx -GM_s \frac{r}{s^3} \left(\frac{\vec{r}}{r} - 3 \frac{\vec{s}}{s} \cos \psi \right), \quad (2.13)$$

having $\frac{r}{s^3}$ as the tidal acceleration.

Depending on where the satellite is located, either \vec{r} is parallel or perpendicular to \vec{s} , the acceleration then simplifies to, respectively:

$$\ddot{\vec{r}} \approx +2GM_s \frac{\vec{r}}{s^3} \quad \text{and} \quad \ddot{\vec{r}} \approx -GM_s \frac{\vec{r}}{s^3}. \quad (2.14)$$

As seen in Figure 2, if the satellite, the Earth, and a celestial body are all on the same line, a repulsive force applies (satellite moves away from Earth), which is explained by the positive sign of the acceleration in Eq. 2.14. On the contrary, when the satellite is in a perpendicular position with respect to the Earth and the celestial body, it moves towards the Earth.

2.4 Force model

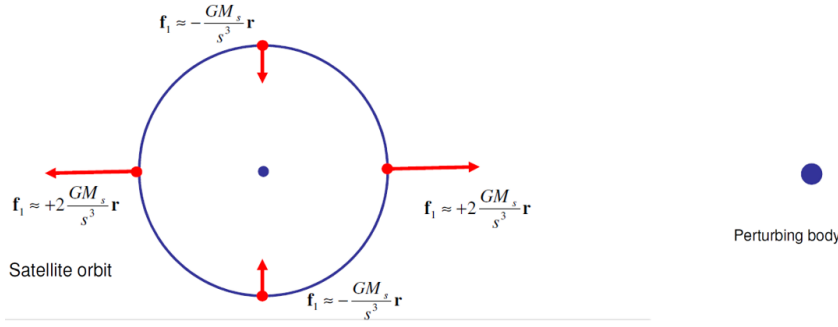


Figure 2: Satellite orbit and forces (f_1) due to a perturbing body (Figure from Hugentobler 2020).

2.4.1.3 Acceleration due to solid Earth tides and ocean tides

The Sun and Moon indirectly impact the Earth, since it is not a rigid body. These are called indirect gravitational perturbations. Although the impact of these perturbations on the satellite orbits is not as prominent as other perturbations (Seeber, 2003), mismodeling of Earth and ocean tides can result in an error of 3 cm as estimated for the error budget of the orbit of TOPEX/Poseidon satellite (Nerem et al., 1993). Recent models contribute to the radial error budget by around 2 mm when compared to orbits computed with other models (Cerri et al., 2010).

The acceleration due to a permanent solid Earth tide can be given by the following equation of motion:

$$\vec{r} = \frac{k_2}{2} \frac{GM_s}{s^3} \frac{R^5}{r^4} (3 - 15 \cos^2 \psi) \frac{\vec{r}}{r} + 6 \cos \psi \frac{\vec{s}}{s}, \quad (2.15)$$

with k_2 being the Love number introduced last century by Love (1909) to describe the elasticity of the Earth. M_s is the mass of the body causing the tidal force (e.g., the Sun or the Moon). R is the radius of the Earth. And ψ is the angle between \vec{r} and \vec{s} . Solid Earth tide models are usually used in POD, such as the models defined by the International Earth Rotation Service (IERS), where more detailed equations with spherical harmonic expansions can be found (Petit and Luzum, 2010).

Ocean tides have a lower impact on the POD (Montenbruck and Gill, 2000). However, there are still some improvements of the SLR RMS of fits by around 0.14% when applying new models for ENVISAT, for example Rudenko et al. (2017). The following equation represents the geopotential variations due to ocean tides (Seeber, 2003). As with the solid Earth tide equation, the full expansion of the equation can be found in Montenbruck and Gill (2000).

$$\Delta U = \frac{G\rho_0 h(P, t) d\sigma}{R} \sum_n (1 + k'_n) P_{n0} \cos \theta, \quad (2.16)$$

where ρ_0 is the average density of water at a height h at a surface point P and time t . k'_n are the deformation coefficients and P_{n0} are the Legendre polynomials, and θ is the geocentric angle between the initial point and the surface point P .

2.4.2. Non-gravitational forces

Non-gravitational forces are surface forces, i.e. they act on the surface of the satellite and are directly proportional to the area-to-mass ratio. Accurate knowledge of the surface properties of the satellite as well as its attitude is of utmost importance for precise modeling of the non-gravitational forces and hence the orbit.

2.4.2.1 Acceleration due to atmospheric drag

The force due to atmospheric drag acts in the opposite direction to the direction of motion. Therefore, it decelerates the satellite and causes a decay in the orbit. An important contributing factor is the air density. Other factors, such as the shape, size, and orientation of the satellite, also have an impact on the modeling of the drag. The equation of motion can be expressed as follows (Montenbruck and Gill, 2000),

$$\vec{r} = -\frac{1}{2}C_d\frac{A}{m}\rho v_r^2\vec{e}_v, \quad (2.17)$$

where $\frac{A}{m}$ is the area-to-mass ratio of the satellite. C_d is the drag coefficient, it is the air resistance factor that usually can be considered as a constant between 1.5 and 2 (where 2 is for a spherical satellite). ρ is the density of the air. v_r is the velocity of the atmosphere relative to the satellite body. And \vec{e}_v is the unit vector of the relative velocity. The perpendicular forces (e.g., due to lift) have less impact than the forces in the along-track direction, and hence can be neglected (Doornbos, 2011).

The velocity of the atmosphere is generally defined with the cross product of Earth's rotation rate ($\vec{\omega}_e$) and the position of the satellite. However, a precise model of the velocity would take into account the wind velocity (\vec{v}_w), which varies depending on the location (maximum at the equator, minimum at the poles) (Panzetta et al., 2019). The following expression is given for the relative velocity,

$$\vec{v}_r = \vec{v}_{sat} - (\vec{\omega}_e \times \vec{r}_{sat} + \vec{R}_{EI}\vec{R}_{LE}\vec{v}_w), \quad (2.18)$$

where \vec{R}_{LE} and \vec{R}_{EI} are the rotation matrices from local coordinates to the Earth fixed system and from the Earth fixed system to the inertial system, respectively.

Considering the importance of the density, the height of the satellite plays a significant role since both the density and the temperature change with height. Other factors, such as solar activity, time of the day, and geomagnetism should also be considered. There are specific models developed for forecasting the thermospheric density in the atmosphere and can be used in POD. According to Doornbos (2011), there are 2 types of thermosphere models: physical models and empirical models. Physical models, as the name suggests, are based on physical equations. These are computationally highly intensive, and they require experts to interpret the output. Therefore, they are not used in applications such as orbit determination. Empirical models are based on a predefined database parameters that consists of parameters fitted to observations. When input parameters are defined, interpolation and extrapolation of the database parameters are performed. Then the model provides the total density and temperature (Doornbos, 2011). Thermosphere density models used

in POD are: Jacchia-Bowman model (Bowman et al., 2008), Drag Temperature Model (DTM) series (Bruinsma, 2015), and Mass Spectrometer Incoherent Scatter (MSIS) series (Hedin, 1991). The recent models from the MSIS series, namely, NRLMSISE-00 and NRLMSIS 2.0, will be discussed and evaluated in terms of their impact on the orbits of altimetry satellites in Section 5.2.

2.4.2.2 Acceleration due to radiation pressure

There are direct and indirect radiation pressures. Direct radiation pressure, also known as solar radiation pressure, is the most prominent radiation pressure. The solar radiation pressure is directly proportional to the solar flux. The total force experienced by the satellite is then directly proportional to the solar flux and the surface area.

Since the solar flux is not constant throughout the year and depends on the distance from the sun, the solar radiation pressure (P_{\odot}) is also not constant and varies by around $\pm 3.3\%$. Another important factor is the reflectivity of the surface, and it can be expressed as ϵ (Montenbruck and Gill, 2000).

The following acceleration expression can be obtained:

$$\vec{r} = -P_{\odot} \frac{1AU^2}{r_{\odot}^2} \frac{A}{m} \cos \theta [(1 - \epsilon) \vec{e}_{\odot} + 2\epsilon \cos \theta \vec{n}] \quad (2.19)$$

The solar radiation pressure is scaled to $\left(\frac{AU}{r_{\odot}}\right)^2$ due to the elliptic orbit of the Earth, where AU stands for Astronomical Unit and r_{\odot} is the actual distance between the center of the Earth and the Sun. θ is the incidence angle computed from: $\cos \theta = \vec{n}^T \vec{e}_{\odot}$. \vec{n} and \vec{e}_{\odot} are unit vectors pointing into the direction of the Sun.

This equation is valid if the satellite is always in the sunlight. However, the satellite will have an eclipse period, and this should be considered by multiplying the equation with a factor of 1 if it is in the sunlight, 0 if it is in umbra (eclipse), and between 0 and 1 if it is in penumbra, see Figure 3 for the geometry. As in the case of air drag models, due to the complexity of the physical properties and the extensive computation of physical models, empirical models are preferred. The modeled acceleration also depends on the orientation angle of the satellite with respect to the Sun as well as to the Earth to ensure that the antenna of the satellite is pointing towards the Earth and the solar panels are pointing towards the sun.

The indirect radiation pressure is known as the albedo radiation, which is the sunlight radiation reflected from the Earth, and the thermal radiation pressure, which is the push caused by the internal heating of the satellite when it is emitted. The acceleration function due to the Earth's albedo radiation is as follows, in which the visible part of the Earth to the satellite is partitioned into

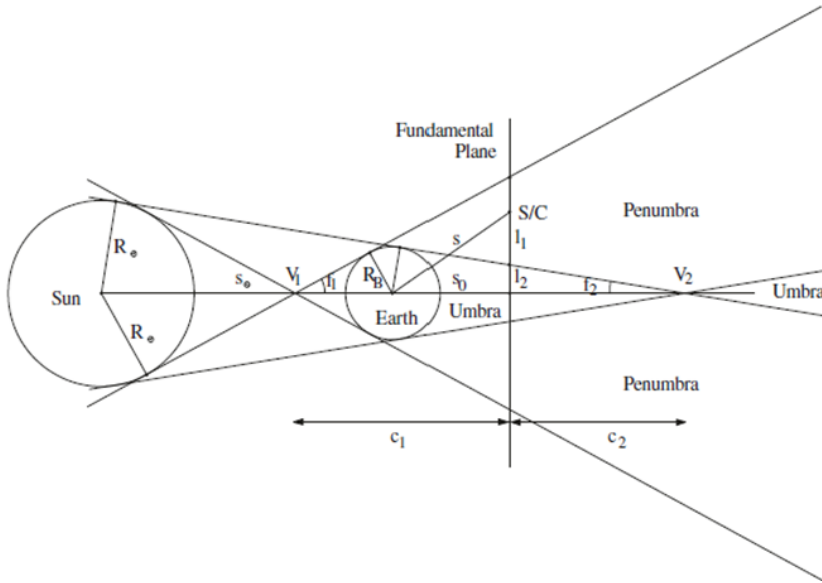


Figure 3: The geometry of satellite in shadow (Figure from Montenbruck and Gill 2000).

$j = 1, \dots, N$ segments or surface elements:

$$\vec{r} = \sum_{j=1}^N C_R (v_j a_j \cos \theta_j^E + \frac{1}{4} \epsilon_j) P_{\odot} \frac{A}{m} \cos \theta_j^s \frac{dA_j}{\pi r_j^2} \vec{e}_j, \quad (2.20)$$

with j as the number of surface elements. C_R is the solar radiation coefficient. v_j is the Earth element shadow function. dA_j is the Earth area elements. θ_j^E and θ_j^s are the angles of Earth and satellite surfaces normal to the incident radiation. \vec{e}_j is the unit vector pointing from the Earth surface element to the satellite and the distance is r_j . a_j and ϵ_j are albedo and emissivity, respectively. These 2 terms vary with latitude. As discussed in Knocke et al. (1988), they can be modeled with 0^{th} , 1^{st} , and 2^{nd} zonal harmonic. The given model is used in recent studies addressing POD, such as in Zeithöfler et al. (2023).

2.4.3. Relativistic effects and other perturbations

The relativistic effects are modeled by Petit and Luzum (2010). They are caused by space-time dragging due to the mass and the rotation of the Earth. As described in Seeber (2003), they have less influence on the orbits compared to other perturbations, with an order of $10^{-8} m/s^2$ for TOPEX/Poseidon satellite. Other perturbations which may have been mismodeled or unmodeled forces can be represented with empirical acceleration.

3. Investigation on the optimal method for satellite coordinate interpolation

Satellite orbit solutions may be given in different time systems and with different step sizes. This yields up to 30 seconds of time shift in one orbit product with respect to another. A comparison of such orbits requires an interpolation method with an accuracy of a sub-millimeter level in order to be able to make a proper judgment on the orbit product quality. The choice of the interpolation method depends on several factors, such as the required level of accuracy, the difference between the orbit step sizes, and the desired speed of computation. In the literature, investigations of various interpolation methods were carried out on GPS satellite orbits and ephemerides, of which the step size is 15 minutes. Zheng and Zhang (2020) carried out a comparative analysis of the commonly used methods, i.e. Lagrange, Neville-Aitken, Newton, and Hermite interpolation algorithms with respect to their accuracy and efficiency. Further, they developed a new strategy in which they achieved a sub-millimeter accuracy by using Hermite interpolation with what they called a “sliding window” (cf. Section 3.1.6). Yousif and El-Rabbany (2007) tested the performance of Lagrange, Newton divided difference, cubic spline, and trigonometric interpolation. They found that the cubic spline method had the worst accuracy, while Newton and Lagrange interpolation methods provided identical results, and the trigonometric interpolation method resulted in the best accuracy. Wang et al. (2018) conducted a similar comparison between Lagrange, Newton, Chebyshev, Hermite, and cubic spline interpolation methods on a GPS satellite orbit over a period of 6.5 hours. They concluded that Newton interpolation is the optimal method for interpolating a 30-minute step size GPS orbit to every 15 minutes. In the following, a detailed description of the 5 most commonly used interpolation methods is given.

3.1. Numerical interpolation methods

3.1.1. Lagrange interpolation

At a specific time point t_i , there exists a unique polynomial function

$$p(t_i) = f(t_i), \quad (3.1)$$

where $p(t_i)$ is the approximated value at time t_i and the given value $f(t_i)$. For a polynomial of order n , the following function is evaluated:

$$p(t) = \sum_{i=0}^n f(t_i)l_i(t), \quad (3.2)$$

with

$$l_i(t) = \frac{(t - t_0)(t - t_1) \cdots (t - t_{i-1})}{(t_i - t_0)(t_i - t_1) \cdots (t_i - t_{i-1})} \cdot \frac{(t - t_{i+1}) \cdots (t - t_n)}{(t_i - t_{i+1}) \cdots (t_i - t_n)}. \quad (3.3)$$

For order n , $n + 1$ number of points should be available to be used in the computation of the polynomial (Eq. 3.1, Eq. 3.3). For orbit interpolation, polynomial orders of 8 to 11 are used (Feng and Zheng, 2005). Neta et al. (1996) compared several polynomial interpolation methods for ephemeris data of GPS, of which the data is provided every 15 minutes. They suggested using a short-arc polynomial method, in other words, applying a sliding window approach with an 11^{th} order (of 12 points) since longer arcs result in errors larger than 1 cm. In the investigation done by Wang et al. (2018), the accuracy of the Lagrange method reached 10^{-4} m for each component (East, North, and Up). However, this might change by changing the interpolation order. One disadvantage of Lagrange interpolation is that when adding a new point, the whole function must be recalculated, and hence, it is inefficient in terms of computation time (Zheng and Zhang, 2020).

3.1.2. Newton interpolation

Newton's divided difference method is considered more efficient than the Lagrange method, since it does not perform recurrent calculations of the polynomial when new points are considered. One can only add a new term for each new point (Neta et al., 1996).

$$p(t) = a_0 + (t - t_0)a_1 + (t - t_0)(t - t_1)a_2 + \cdots + (t - t_0)(t - t_1) \cdots (t - t_{n-1})a_n, \quad (3.4)$$

where a_n is the polynomial coefficient of order n , as simplified by Yousif and El-Rabbany (2007):

$$\begin{aligned} a_0 &= p(t_0) \\ a_1 &= \frac{p(t_1) - a_0}{(t_1 - t_0)} \\ a_2 &= \frac{p(t_2) - a_0 - a_1(t_2 - t_0)}{(t_2 - t_0)(t_2 - t_1)} \\ &\vdots \\ a_n &= \frac{p(t_n) - a_0 - a_1(t_n - t_0) - a_2(t_n - t_0)(t_n - t_1) - \cdots}{(t_n - t_0)(t_n - t_1)(t_n - t_2) \cdots (t_n - t_{n-1})}. \end{aligned} \quad (3.5)$$

The shift between the 2 orbit solutions is usually equally spaced,

$$t_k = t_0 + kh, \quad (3.6)$$

where t_0 is the reference time for the interval, h is a constant step size, and k is a positive integer value. For this specific case, the Newton divided difference method takes a specific form, known as Newton's forward difference (Δf)

$$\Delta f(t_i) = f(t_{i+1}) - f(t_i) = f(t_i + h) - f(t_i), \quad (3.7)$$

of which we can compute the power of differences iteratively:

$$\Delta^k f(t_i) = \Delta(\Delta^{k-1} f(t_i)) = \Delta^{k-1} f(t_{i+1}) - \Delta^{k-1} f(t_i). \quad (3.8)$$

Finally, the polynomial can be derived from:

$$p(t) = f_0 + \frac{(t - t_0)}{h} \Delta f_0 + \frac{(t - t_0)(t - t_1)}{2h^2} \Delta^2 f_0 + \dots + \frac{(t - t_0)(t - t_1) \dots (t - t_{n-1})}{n!h^n} \Delta^n f_0. \quad (3.9)$$

Wang et al. (2018) obtained identical accuracy of the Newton method compared to the Lagrange method. However, the processing of Newton method is much faster.

3.1.3. Trigonometric interpolation

Neta et al. (1996) and Schenewerk (2003) observed that the orbits of GPS satellites are very close to periodic in inertial coordinates. Therefore, they suggested that it is possible to use trigonometric functions to interpolate such orbits. The trigonometric function is of the form

$$p(t) = a_0 + \sum_{k=1}^n (a_k \cos kt + b_k \sin kt), \quad (3.10)$$

where k here is the characteristic frequency, and a_k and b_k are polynomial coefficients. The interval of the recreated orbit should be over the exact interval of the original orbit, i.e. over a single period. In the case of GPS data, it is 24 hours. In this method, the number of fitted points and the number of coefficients to be estimated (the order of the method) can be different. As stated by Feng and Zheng (2005), for a better result, the number of points can be larger than the order of the method. The authors found that the trigonometric interpolation method delivered an RMS error of 0.3 cm for an interval of 15-minute data interpolated at step size of 30 seconds.

3.1.4. Hermite interpolation

This method is known for its capability to use the 1st order and higher order derivatives of the data. An advantage compared to other methods is that it requires less number of points to compute the function of the same order (Zheng and Zhang, 2020). A polynomial f_n at any time of interest t can be computed using $n - 1$ points, with the 1st derivative f' :

$$f_n(t) = \sum_{i=0}^{n-1} [f(t_i) + (t - t_i)(f'(t_i) - 2f(t_i)l'_i(t_i))]l_i^2(t_i), \quad (3.11)$$

with the basic function l_i and its derivative l'_i :

$$l_i(t) = \prod_{j=0, j \neq i}^{n-1} \frac{(t - t_j)}{t_i - t_j}, \quad (3.12)$$

$$l'_i(t) = \sum_{j=0, j \neq i}^{n-1} \frac{1}{t_i - t_j}, \quad (3.13)$$

having t_i and t_j to be 2 separate time instants.

Zheng and Zhang (2020) used the position and velocity values assuming that the acceleration does not change rapidly in the studied time span, they computed an accuracy in satellite position of the

order of 10^{-4} m. Another study by Wang et al. (2018) obtained an accuracy of the order of 10^{-3} m and found that the Hermite method is faster than the Newton method. According to a test study carried out by Karepova and Kornienko (2019), in order to take full advantage of the method, the first and second derivatives should be available. However, in most cases, the accelerations are not provided with the orbit solutions. Therefore, only the 1st derivative, i.e. the velocity is used in this study.

3.1.5. Spline interpolation

The above-mentioned methods interpolate over the specified time interval using a high order polynomial. Another method is to calculate the polynomial over several small intervals using the walk-along interpolation. However, this does not fully overcome the Runge phenomenon and results in a non-smooth orbit (cf. Section 3.1.6). The spline method calculates the polynomial of all small intervals at once, and the polynomial is continuous at its first ($f'(t)$) and second derivative ($f''(t)$). The spline method usually uses 3rd order polynomial, i.e. cubic spline interpolation between 2 successive points. In the following, the general formula is shown for each ephemeris value:

$$p_i(t) = A_i(t)f(t_i) + B_i(t)f(t_{i+1}) + C_i(t)f''(t_i) + D_i(t)f''(t_{i+1}), \quad i = 0, \dots, n-1 \quad (3.14)$$

where n is the number of ephemeris values and the functions A_i , B_i , C_i , and D_i read:

$$\begin{aligned} A_i(t) &= \frac{t_{i+1} - t}{t_{i+1} - t_i} \\ B_i(t) &= \frac{t - t_i}{t_{i+1} - t_i} \\ C_i(t) &= \frac{1}{6}(A_i^3 - A_i)(t_{i+1} - t_i)^2 \\ D_i(t) &= \frac{1}{6}(B_i^3 - B_i)(t_{i+1} - t_i)^2. \end{aligned} \quad (3.15)$$

To solve the $n + 1$ value problem, the function values and the values of the first derivative at the boundaries, i.e. at t_0 and t_n , should be known (Neta et al., 1996). This method is much faster compared to the other methods. However, even with the absence of the Runge phenomenon, the accuracy is lower than that of the high order polynomial methods (Lagrange, Hermite, or Newton), which reached up to 6 m in the East, 9 m in the North, and 31 m in the Up directions. The results are obtained for interpolating a GPS satellite orbit with a step size of 30 minutes, which explains the large values of the errors, and a time interval of 6.5 hours as given by Wang et al. (2018).

3.1.6. Runge phenomenon

One common drawback in high order polynomial methods is that the function starts to oscillate, and the error grows largely at both ends of the interval. This phenomenon is known as ‘‘Runge phenomenon’’. Studies in the literature suggest strategies to overcome this phenomenon, such as *sliding window* method, also known as the walk-along interpolation (Feng and Zheng, 2005; Yousif and El-Rabbany, 2007; Zheng and Zhang, 2020; Song et al., 2021). In this approach, the interpolated point shall be at the center of the data points (cf. Section 3.2.2.1). Finding an optimal order of polynomials to fit the interpolation will depend on the data type, the step size, and the

applied method. Feng and Zheng (2005) found that trigonometric interpolation performed better than Lagrange interpolation when using lower order for the interpolation of orbits of GPS satellites. With the same strategy implemented on Hermite interpolation, Zheng and Zhang (2020) found that the Runge phenomenon will stay in an acceptable range of accuracy, although the oscillating behavior is still observed in the interpolated data.

3.2. Interpolation methods analysis

As discussed in Section 3.1, various interpolation methods can be used for different scenarios. This thesis studies the interpolation methods for orbit interpolation of altimetry satellites which are generally provided with a step size of 10, 30, and 60 seconds. In the scope of this study, the interpolation methods have been applied using MATLAB functions for Lagrange¹ interpolation method, Newton² interpolation method with additional enhancement to meet the described functionality as in Section 3.1.2, Hermite interpolation method as a transformed version of an internal DGFI-TUM Fortran routine to a MATLAB function, and the spline interpolation method that is a built-in function³ in MATLAB.

For the sake of the comparison between 2 orbit solutions, one solution should be fixed to be used as a reference for interpolation, and the other solution(s), called non-reference solution(s), should be interpolated to the time instants of the reference solution. Several tests have been done in order to analyze the behavior of the methods in terms of accuracy and time efficiency. In the following, a description of the conducted tests and the approaches used is given, as well as the results obtained.

3.2.1. 1-second orbit interpolation

The 1-second orbit is a TOPEX/Poseidon satellite orbit computed with DOGS-OC specifically for determining the accuracy of the interpolation methods. The arc length is 3.5 days with a 1-second step size (YYYY-MM-DD hh:mm:ss) (from 2004-07-18 00:00:00 to 2004-07-21 12:00:00). The test discussed in this section has been performed using Newton interpolation method. The reference orbit with a step size of 1-second is used with, depending on the order, one non-reference orbit of 30 (scenario 1), 60 (scenario 2), and 120 (scenario 3) second step size. All 3 orbit solutions are generated out of the 1-second orbit to assess the accuracy of the interpolation method. In this test, interpolation orders from 5 to 9 have been tested. To differentiate between the points to be interpolated to (points of the reference solution) and the input points for the interpolation (points of non-reference solution), the input points are called nodes. That means 6 nodes are input for order 5, 7 nodes are input for order 6, and so on.

¹ https://de.mathworks.com/matlabcentral/fileexchange/66906-lagrange-x-y-x_inter

² <https://de.mathworks.com/matlabcentral/fileexchange/7405-newton-s-interpolation>

³ <https://de.mathworks.com/help/matlab/ref/interp1.html>

3.2.1.1 Scenario 1: step size of 30 seconds

The reference orbit is of a 1-second step size, whereas the non-reference orbit is of a 30-second step size. The differences between the reference and the interpolated non-reference orbits are computed and shown in the following figures, with the means and standard deviations (STD) of the differences.

Firstly, the 5th order interpolation is tested. 6 nodes are taken from the 30-second solution, namely, 2004-07-18 00:00:00, 2004-07-18 00:00:30, 2004-07-18 00:01:00, 2004-07-18 00:01:30, 2004-07-18 00:02:00, and 2004-07-18 00:02:30, in the Coordinated Universal Time (UTC) system. The nodes are used to interpolate an orbit position at each second in between. The obtained coordinates are compared with the coordinates of the reference solution and the differences in XYZ are transformed to the radial, transverse, and normal (RTN) system. The RTN orbit differences are shown in Figure 4 (left panels) in the International Atomic Time (TAI) system. The panels on the right-hand are a zoomed-in version to the middle of the interval of one-minute length, i.e. 30 seconds to the left of the middle point and 30 seconds to the right of the middle point of the interval. This is done to see how the accuracy changes over 60 seconds when considering the middle interval since most altimetry satellite orbits are of 30 or 60 seconds step size and thus, the interpolation range can reach up to 60 seconds. The standard deviation in the radial direction has slightly improved for the case of the middle interval, as compared to the case of the full interval (from 0.309 mm to 0.285 mm). Whereas, the absolute mean value has increased from 0.126 mm to 0.206 mm.

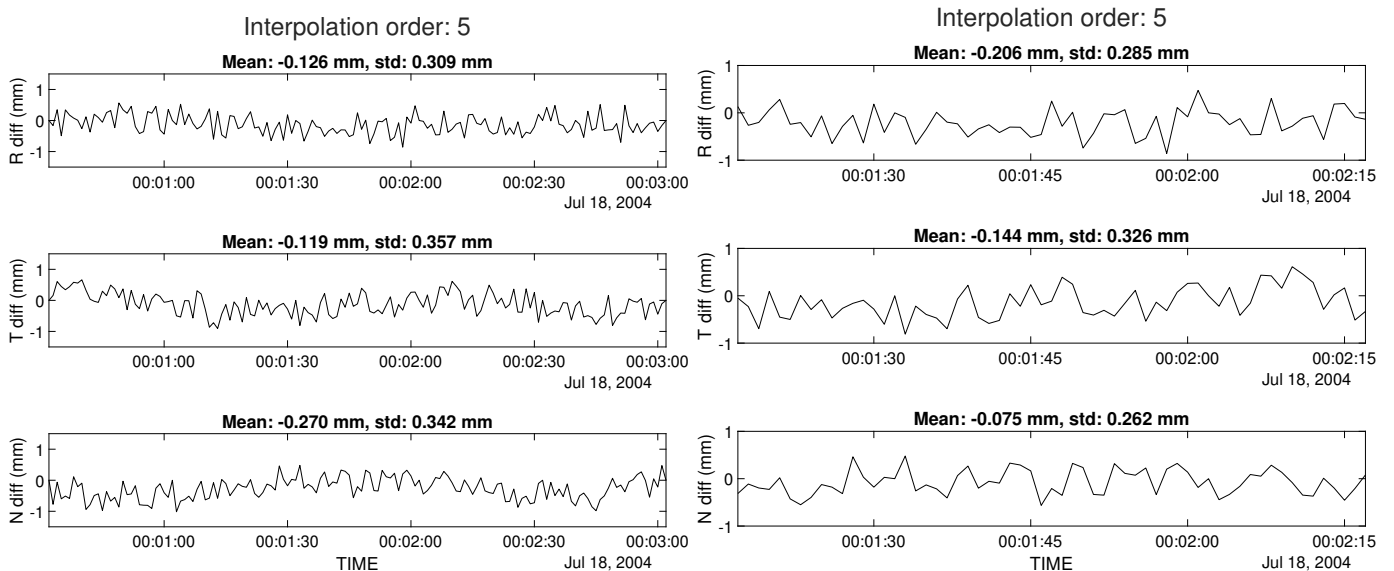


Figure 4: Orbit differences when interpolating a 30-second solution to a 1-second solution using Newton interpolation method of order 5 (left: full interval, right: middle interval) in the TAI system.

Next, the number of nodes is increased accordingly for interpolations of order 6 (Figure 5), 7 (Figure 6), 8 (Figure 7), and 9 (Figure 8).

The difference in the standard deviation of the middle interval and the full interval is larger for higher

3.2 Interpolation methods analysis

orders (7, 8, and 9). In this scenario, order 6 provides the lowest standard deviation of 0.274 mm in the middle interval, and 0.306 mm in the full interval of 7 nodes. Runge phenomenon (Section 3.1.6) is not clearly seen in the figures of the full interval because of the relatively small step size (30-second) and low polynomial order. The effect is larger in order 9. However, the accuracy is still not largely degraded. Table 1 summarizes the mean and standard deviation values of the tests.

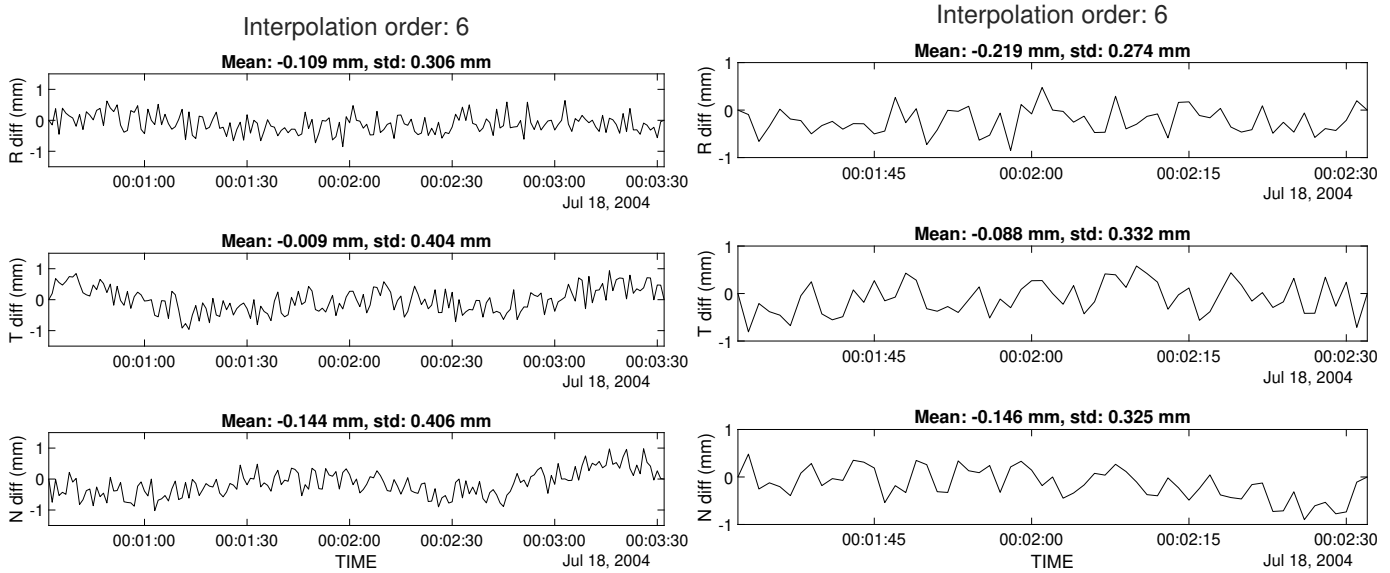


Figure 5: Orbit differences when interpolating a 30-second solution to a 1-second solution using Newton interpolation method of order 6 (left: full interval, right: middle interval) in the TAI system.

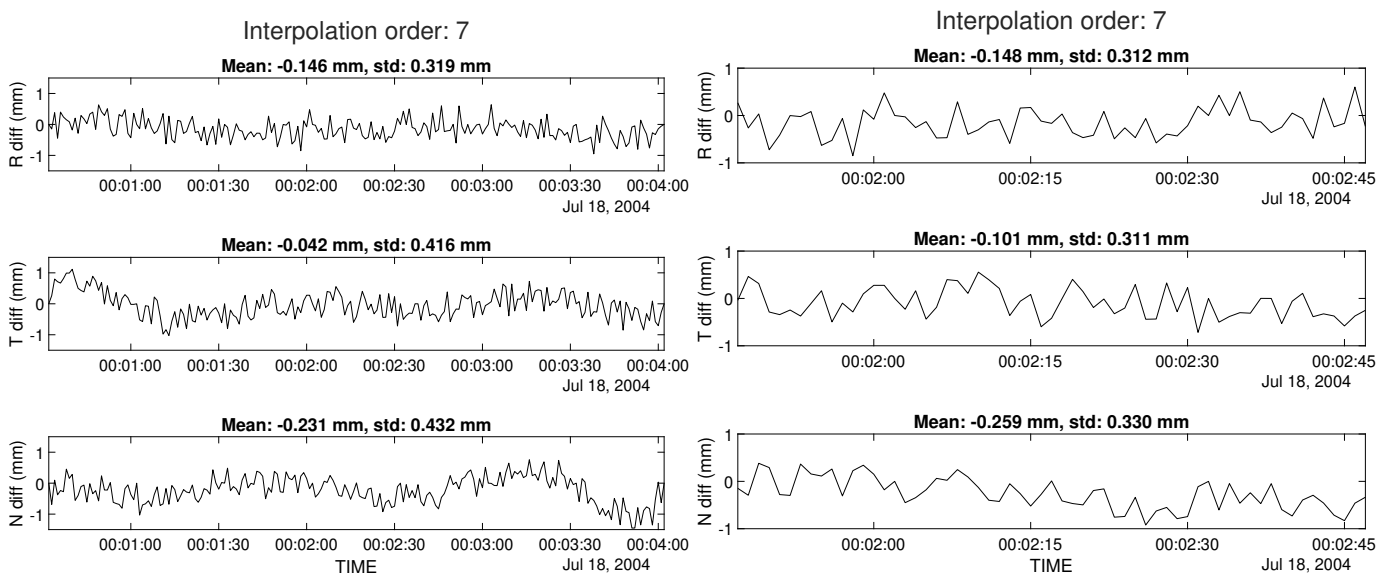


Figure 6: Orbit differences when interpolating a 30-second solution to a 1-second solution using Newton interpolation method of order 7 (left: full interval, right: middle interval) in the TAI system.

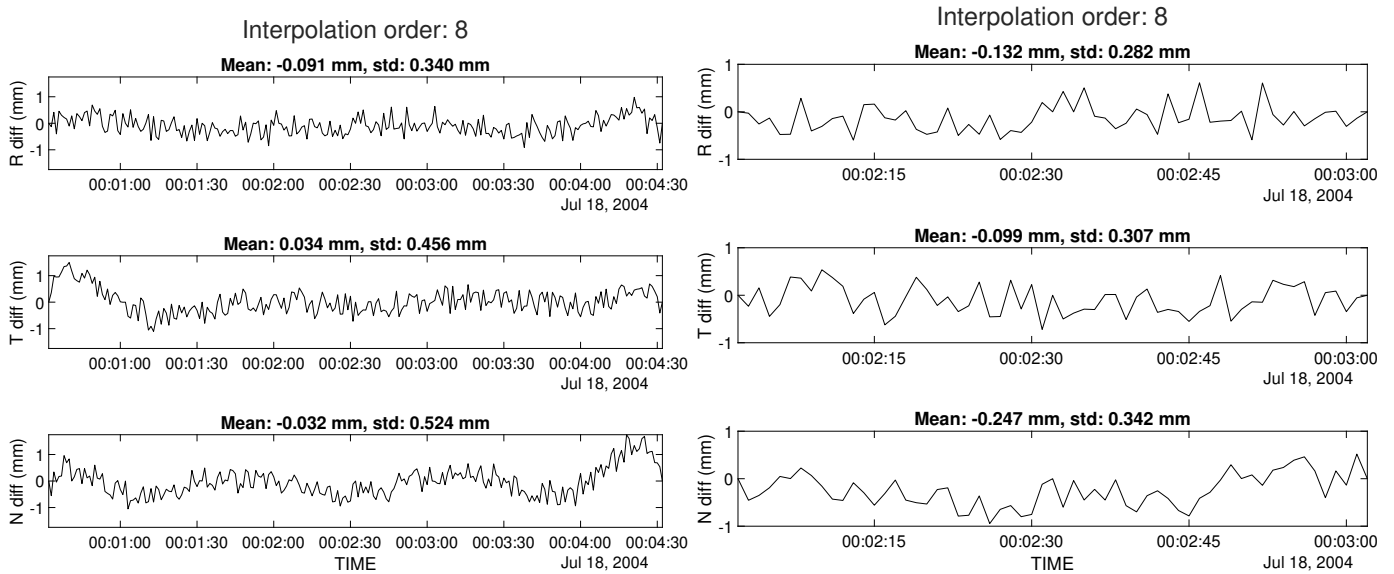


Figure 7: Orbit differences when interpolating a 30-second solution to a 1-second solution using Newton interpolation method of order 8 (left: full interval, right: middle interval) in the TAI system.

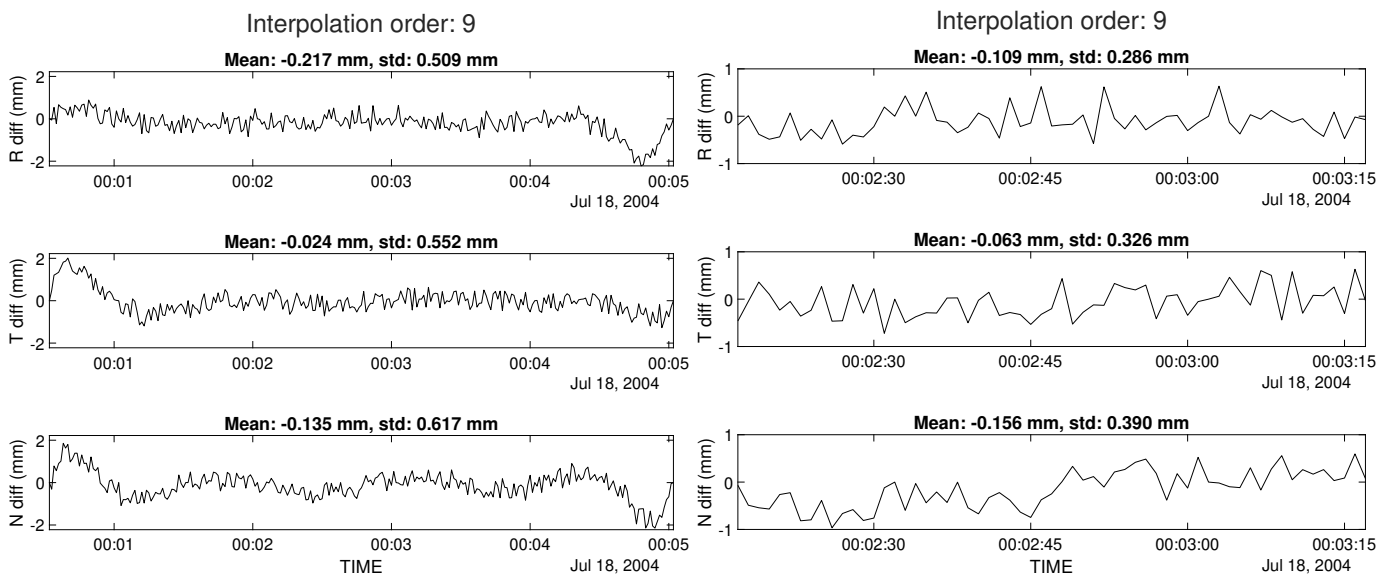


Figure 8: Orbit differences when interpolating a 30-second solution to a 1-second solution using Newton interpolation method of order 9 (left: full interval, right: middle interval) in the TAI system.

3.2.1.2 Scenario 2: step size of 60 seconds

As in scenario 1, the reference solution is of 1-second step size, the non-reference orbit, however, is of 60-second step size. In this scenario, the 5th order interpolation has the 6 nodes: 2004-07-18 00:00:00, 2004-07-18 00:01:00, 2004-07-18 00:02:00, 2004-07-18 00:03:00, 2004-07-18 00:04:00, and 2004-07-18 00:05:00 in the UTC system, and the interpolation is done over each second in between.

Figure 9 shows the differences of the interpolated orbit to the reference orbit in the RTN system

using Newton interpolation method of order 5. The differences in the radial direction showed decreased accuracy in this scenario (standard deviation in $R = 1.845$ mm), as compared to the accuracy of the 5th order in scenario 1 (standard deviation in $R = 0.309$ mm) in the full interval. The accuracy enhances when taking the middle interval (the right-hand side of Figure 9), however, it is still relatively low (standard deviation in $R = 0.418$ mm). The accuracy in the middle interval increases with increasing the order. The highest accuracy is obtained in order 8 with a standard deviation of 0.288 mm in the radial component. On the other hand, the highest accuracy in the full interval is obtained with order 6, where the standard deviation in the radial direction is equal to 0.334 mm (Figure 10). In addition, the Runge phenomenon can be observed at the edges of the full intervals (left-hand side plots of Figures 9-13).

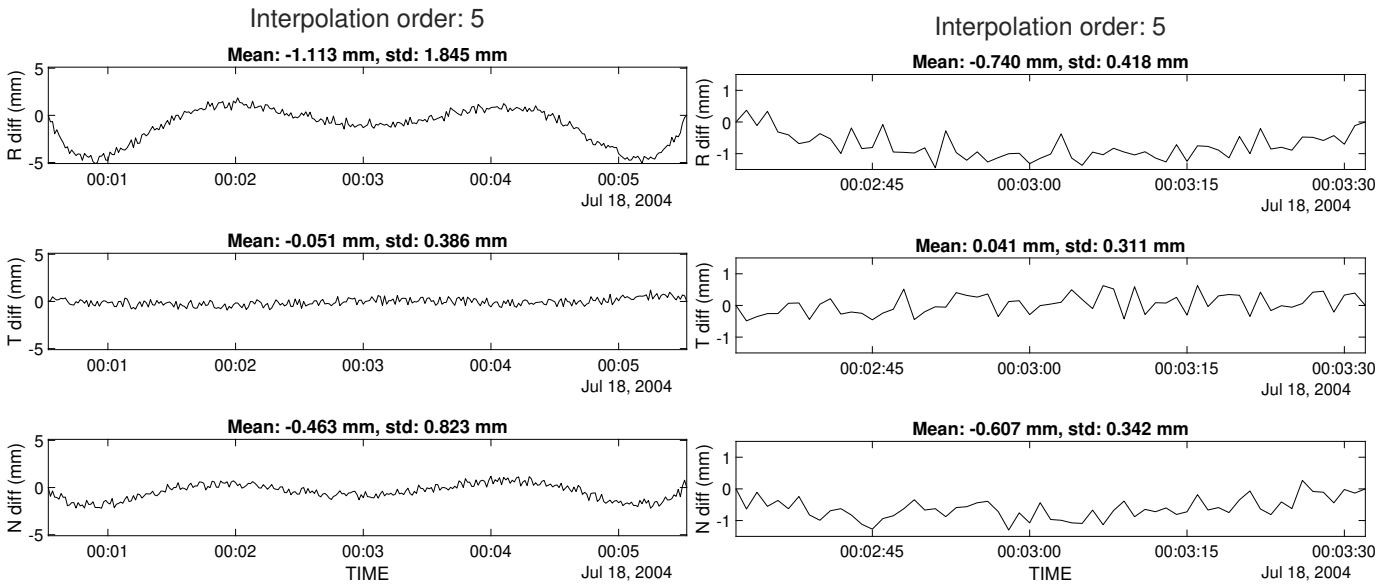


Figure 9: Orbit differences when interpolating a 60-second solution to a 1-second solution using Newton interpolation method of order 5 (left: full interval, right: middle interval) in the TAI system.

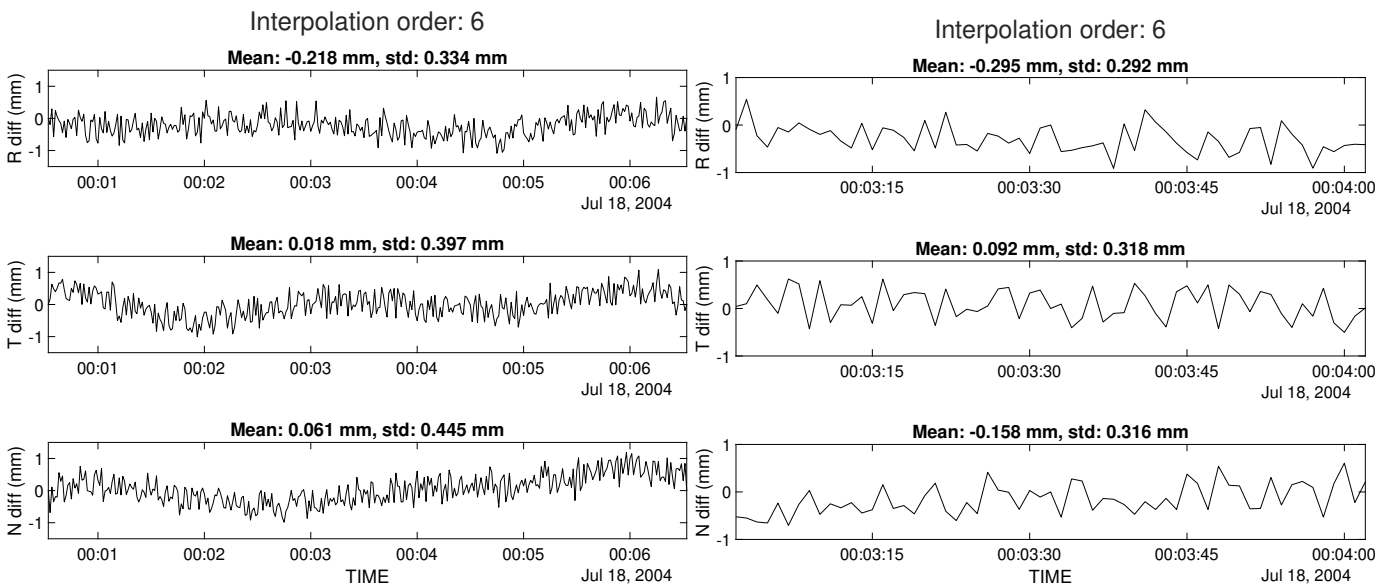


Figure 10: Orbit differences when interpolating a 60-second solution to a 1-second solution using Newton interpolation method of order 6 (left: full interval, right: middle interval) in the TAI system.

3.2 Interpolation methods analysis

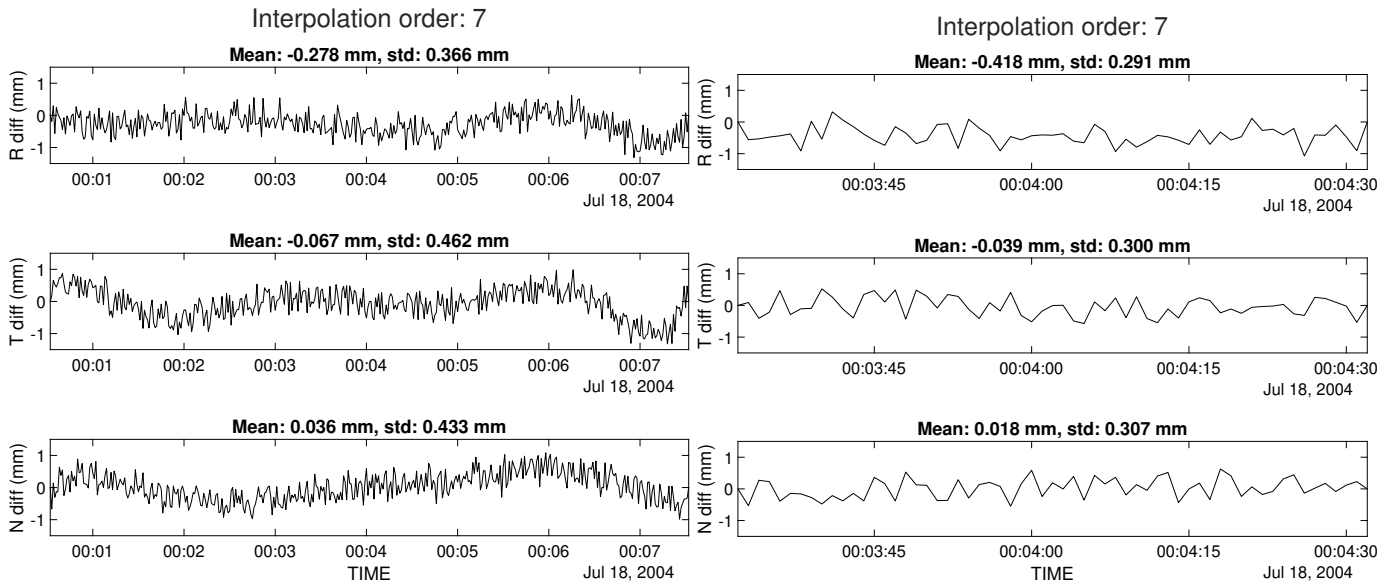


Figure 11: Orbit differences when interpolating a 60-second solution to a 1-second solution using Newton interpolation method of order 7 (left: full interval, right: middle interval) in the TAI system.

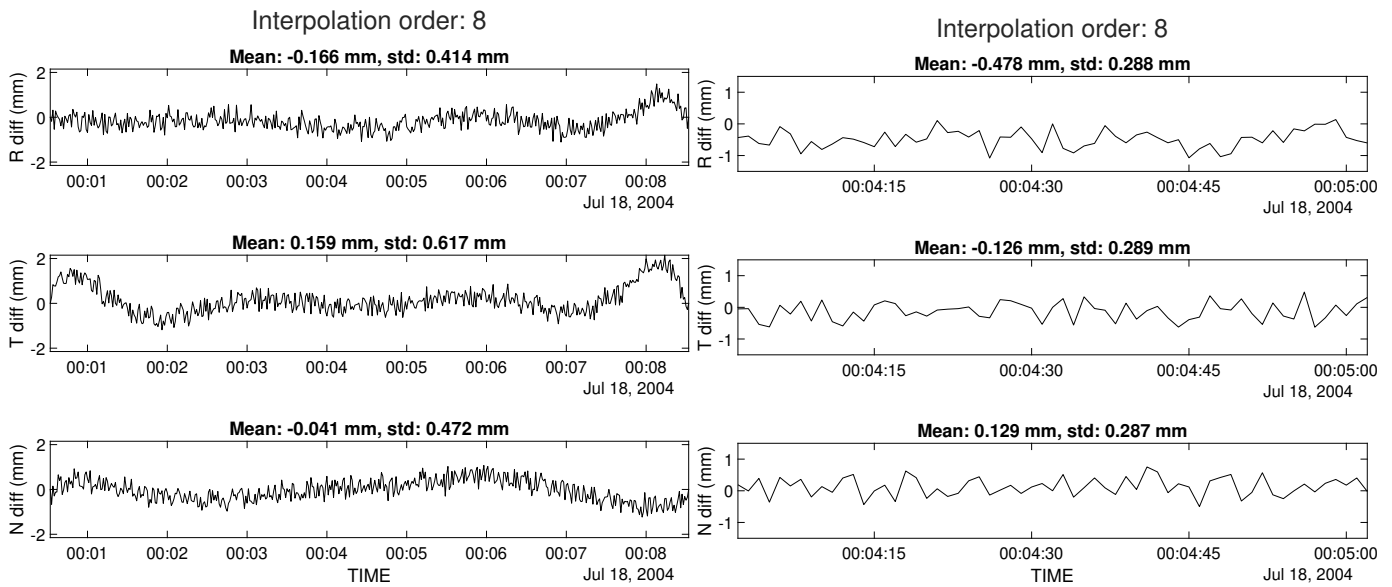


Figure 12: Orbit differences when interpolating a 60-second solution to a 1-second solution using Newton interpolation method of order 8 (left: full interval, right: middle interval) in the TAI system.

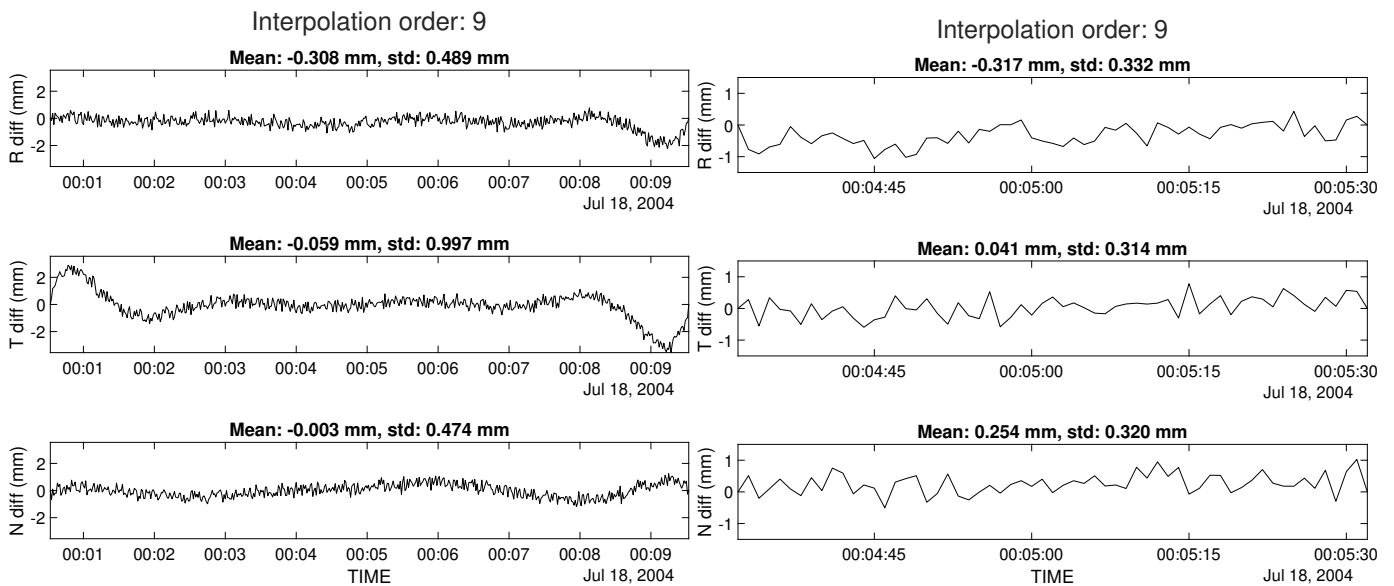


Figure 13: Orbit differences when interpolating a 60-second solution to a 1-second solution using Newton interpolation method of order 9 (left: full interval, right: middle interval) in the TAI system.

3.2.1.3 Scenario 3: step size of 120 seconds

In general, most orbits of altimetry satellites are provided with a 60-second step size. However, we want to investigate the interpolation behavior of the orbits with 120-second step size. The 5th order in this scenario has the nodes: 2004-07-18 00:00:00, 2004-07-18 00:02:00, 2004-07-18 00:04:00, 2004-07-18 00:06:00, 2004-07-18 00:08:00, and 2004-07-18 00:10:00 in the UTC system. That means, a larger number of points has to be interpolated between each node. This results in a great deterioration in the accuracy (standard deviation in R = 116.633 mm in the interpolation of the 5th order) and larger values at the edges due to the Runge phenomenon (Figures 14-18).

The middle intervals of the orders higher than 6, i.e. orders 7, 8, and 9, keep the accuracy in an acceptable range (under 0.4 mm in the radial direction). In this scenario, the highest accuracy in the full and middle intervals is obtained with order 7 with a standard deviation of 0.598 mm and 0.274 mm for the full and middle intervals, respectively (Figure 16).

3.2 Interpolation methods analysis

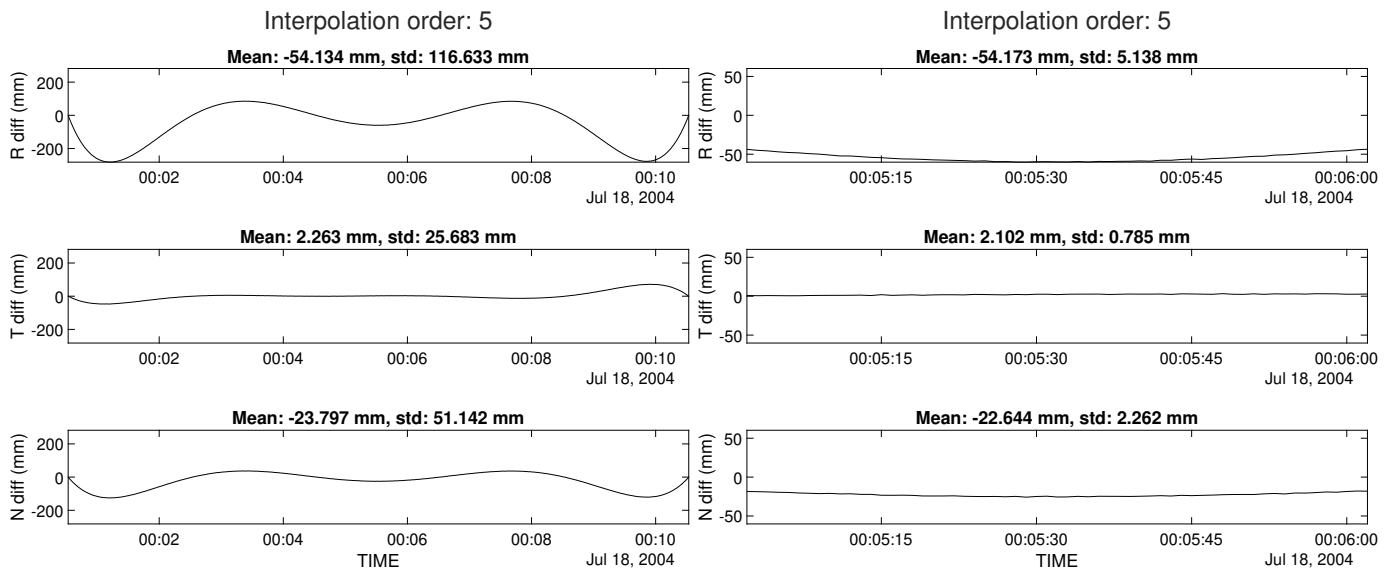


Figure 14: Orbit differences when interpolating a 120-second solution to a 1-second solution using Newton interpolation method of order 5 (left: full interval, right: middle interval) in the TAI system.

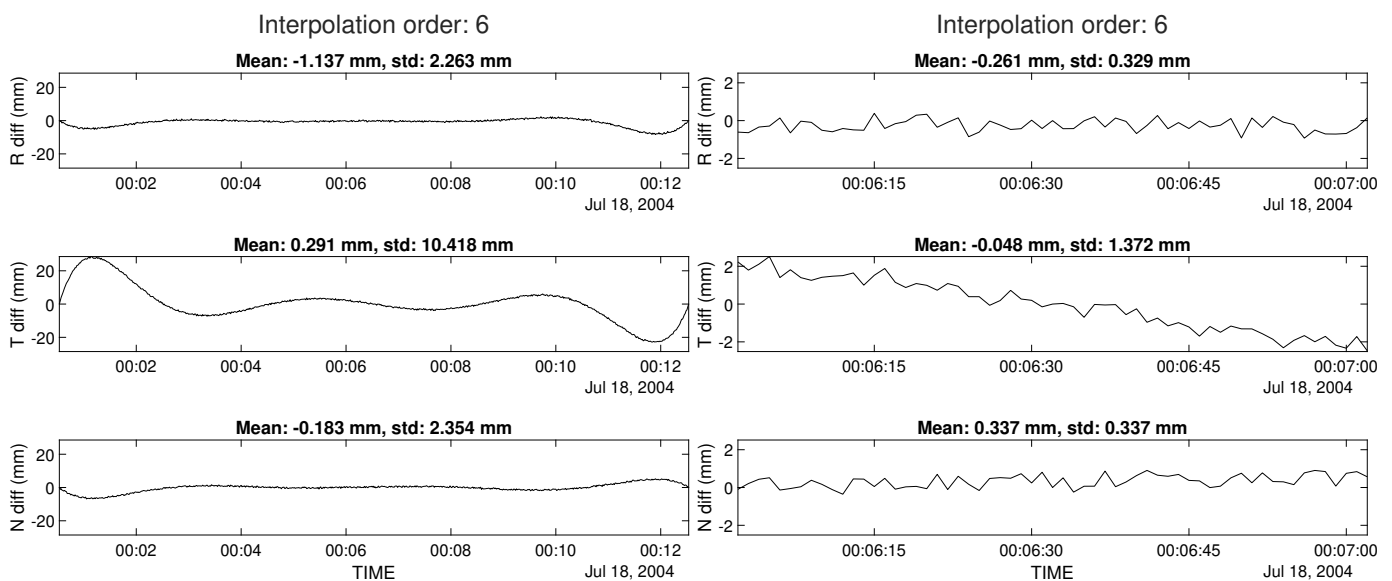


Figure 15: Orbit differences when interpolating a 120-second solution to a 1-second solution using Newton interpolation method of order 6 (left: full interval, right: middle interval) in the TAI system.

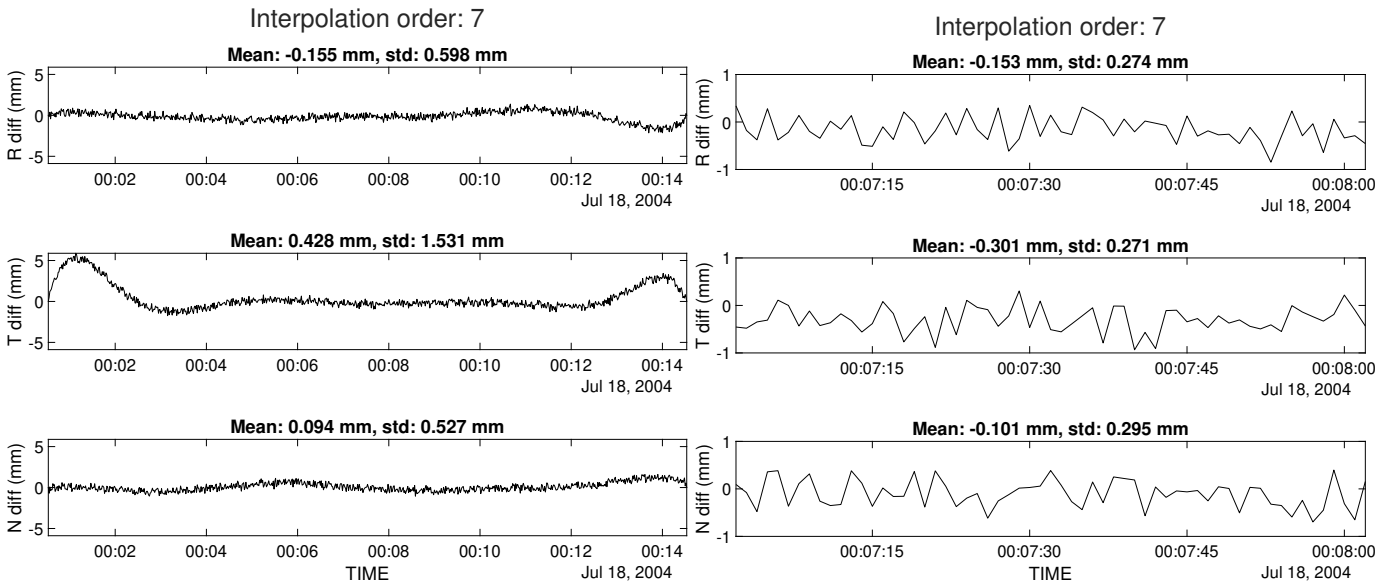


Figure 16: Orbit differences when interpolating a 120-second solution to a 1-second solution using Newton interpolation method of order 7 (left: full interval, right: middle interval) in the TAI system.

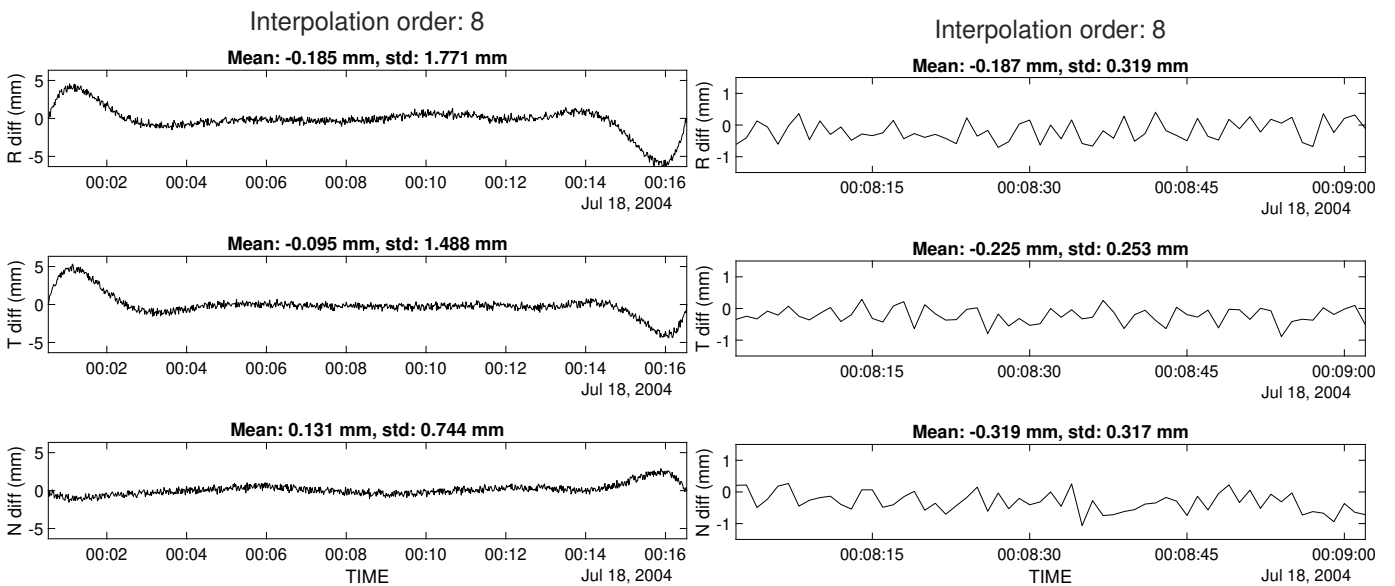


Figure 17: Orbit differences when interpolating a 120-second solution to a 1-second solution using Newton interpolation method of order 8 (left: full interval, right: middle interval) in the TAI system.

3.2 Interpolation methods analysis

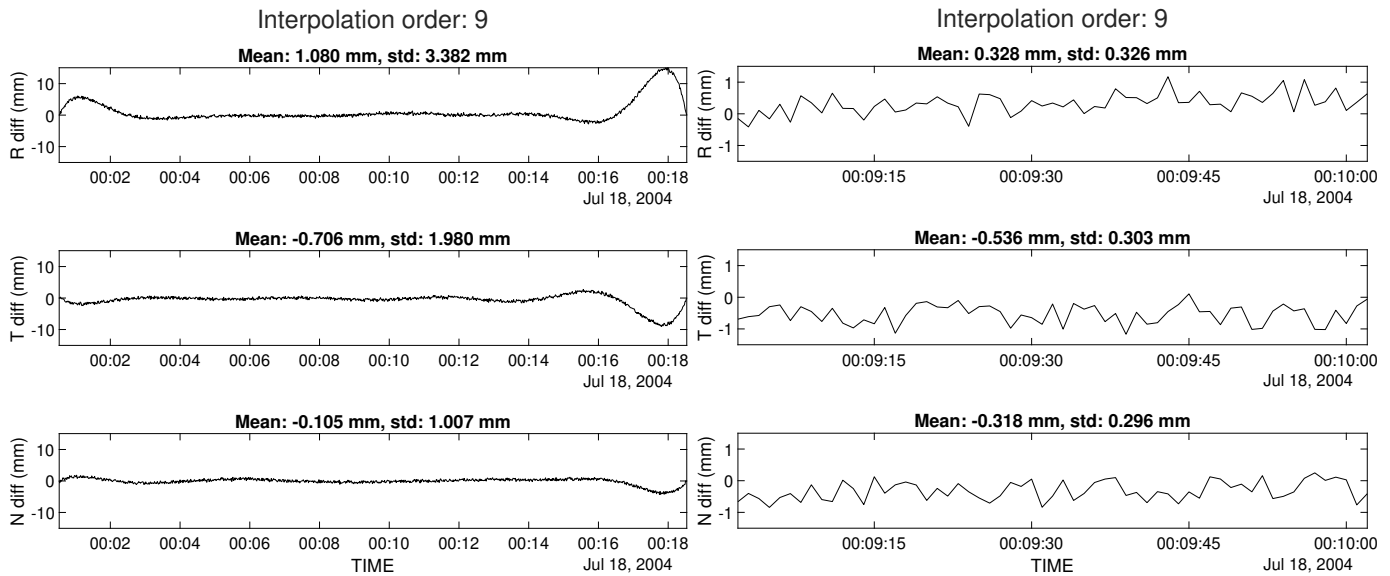


Figure 18: Orbit differences when interpolating a 120-second solution to a 1-second solution using Newton interpolation method of order 9 (left: full interval, right: middle interval) in the TAI system.

The test discussed the accuracy of the Newton interpolation method when there are 2 solutions, one solution with a 1-second step size and the other solution with a 30, 60, or 120-second step size. As a conclusion, the choice of the interpolation order depends on the step size of the orbit solutions. As the test is conducted on a specific time interval, we can only conclude that higher order of interpolation, i.e. 6, 7, or 8, can provide the most accurate results within the middle interval of the window (standard deviation between 0.274 mm and 0.319 mm) (see Table 1). This leads to the next test, where the sliding window interpolation is implemented in order to take advantage of the high accuracy in the middle interval while using the full arc length.

Table 1: Orders 5 to 9, standard deviations and means of orbit differences when interpolating 30, 60, and 120-second step size solutions to the 1-second solution. FI: Full interval, MI: Middle interval, SS: Step size. All values are in mm.

SS	30 s									60 s									120 s								
	standard deviation			absolute mean			standard deviation			absolute mean			standard deviation			absolute mean			standard deviation			absolute mean					
	R	T	N	R	T	N	R	T	N	R	T	N	R	T	N	R	T	N	R	T	N	R	T	N			
5	FI	0.309	0.357	0.342	0.126	0.119	0.270	1.845	0.386	0.823	1.113	0.051	0.463	116.633	25.683	51.142	54.134	2.263	2.263	23.797							
	MI	0.285	0.326	0.262	0.206	0.144	0.075	0.418	0.311	0.342	0.740	0.041	0.607	5.138	0.785	2.262	54.173	2.102	22.644								
6	FI	0.306	0.404	0.406	0.109	0.009	0.144	0.334	0.397	0.445	0.218	0.018	0.061	2.263	10.418	2.354	1.137	0.291	0.183								
	MI	0.274	0.332	0.325	0.219	0.088	0.146	0.292	0.318	0.316	0.295	0.092	0.158	0.329	1.372	0.337	0.261	0.048	0.337								
7	FI	0.319	0.416	0.432	0.146	0.042	0.231	0.366	0.462	0.433	0.278	0.067	0.036	0.598	1.531	0.527	0.155	0.428	0.094								
	MI	0.312	0.311	0.330	0.148	0.101	0.259	0.291	0.300	0.307	0.418	0.039	0.018	0.274	0.271	0.295	0.153	0.301	0.101								
8	FI	0.340	0.456	0.524	0.091	0.034	0.032	0.414	0.617	0.472	0.166	0.159	0.041	1.771	1.488	0.744	0.185	0.095	0.131								
	MI	0.282	0.307	0.342	0.132	0.099	0.247	0.288	0.289	0.287	0.478	0.126	0.129	0.319	0.253	0.317	0.187	0.225	0.319								
9	FI	0.509	0.552	0.617	0.217	0.024	0.135	0.489	0.997	0.474	0.308	0.059	0.003	3.382	1.980	1.007	1.080	0.706	0.105								
	MI	0.286	0.326	0.390	0.109	0.063	0.156	0.332	0.314	0.320	0.317	0.041	0.254	0.326	0.303	0.296	0.328	0.536	0.318								

3.2.2. Comparison of interpolation methods

In this test, the Newton, Lagrange, Hermite, and spline methods are compared in terms of accuracy and time efficiency. Two approaches will be used in this test; the first approach is the sliding window approach (Section 3.2.2.1), and the second approach is the middle-point approach (Section 3.2.2.2).

3.2.2.1 Sliding window interpolation approach

As mentioned previously, increasing the order and the step size between the two solutions will lead to a higher deviation of the results from the true value at both ends of the interval (Runge phenomenon, Section 3.1.6). Therefore, the sliding window implementation is an approach to achieve acceptable accuracy by only taking the point in the center of the window, interpolating to it, and omitting the points at the edges. Figure 19 illustrates an interpolation of order 5 (6 input nodes), using 2 solutions with a 60-second step size. The first (reference) orbit solution is shifted by 30 seconds compared to the second (non-reference) orbit solution. The interpolation will be done to the points of the reference orbit. In the figure, there are two sliding windows. The first one uses the first 6 nodes in the non-reference solution and interpolates to what is called as the "1st" point at time 00:02:30. The second sliding window takes the next 6 nodes by moving 1 node forward from the first sliding window. Then, it interpolates to the "2nd" point at time 00:03:30. The points outside the center of the window are omitted since the Runge phenomenon affects and decreases the interpolation accuracy of these points the most.

At uneven orders, there is an equal number of points to the left and to the right of the interpolation point. Figure 20 illustrates an example of 6th order interpolation with 7 input nodes. That means, the interpolated point is no longer exactly at the center of the window, but shifted to the closest point to the right in the reference solution.

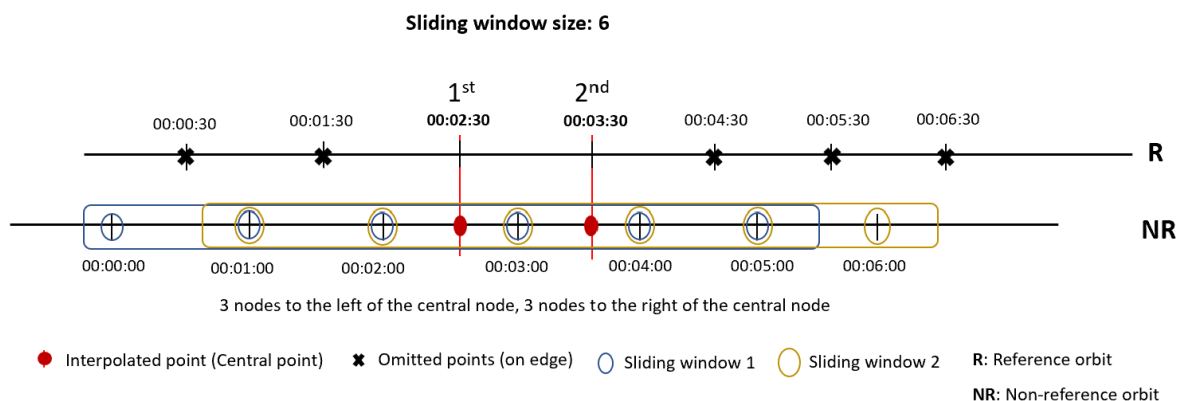


Figure 19: Sliding window approach, 5th order interpolation.

The difference in the accuracy when the number of input nodes (window size) is odd or even is directly related to the order of the method, as shown in the following tables (Tables 2-4). The test was done over an extended version of the arcs explained in Figure 19 and Figure 20. Both orbits

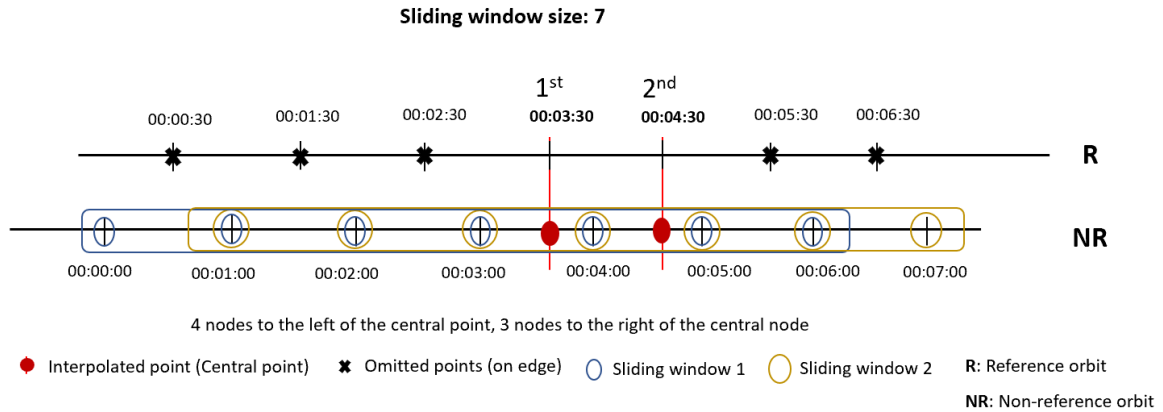


Figure 20: Sliding window approach, 6th order interpolation.

are derived from the same TOPEX/Poseidon 1-second arc. One starts from the 31st epoch and lasts until the end with a 60 second time step (from 2004-07-18 00:00:30 to 2004-07-21 11:59:30). The other orbit starts from the 1st epoch and lasts until the end with a 60-second time step (from 2004-07-18 00:00:00 to 2004-07-21 12:00:00). The second orbit is interpolated to the time instants of the first orbit and will ideally be identical to the first orbit. The difference between the interpolated orbit and the original orbit will be the interpolation error that will be shown in the figures below.

Table 2 demonstrates the comparison between each order of Lagrange interpolation. It can be seen that there is no large difference between even and odd orders. However, when we compare the results for orders 6 to 9, the odd orders (with an even number of input nodes) will have slightly higher accuracy than the even orders (with an odd number of input nodes). In this case, the best accuracy with the standard deviation in the radial component of 0.380 mm is achieved with the interpolation order 7. The results of Newton interpolation are given in Table 3. As obtained by Yousif and El-Rabbany (2007) and Wang et al. (2018), Newton and Lagrange interpolation methods show identical results. However, the duration of the computation using the Newton method is slightly shorter than using the Lagrange method (reduction of between 15% and 20% based on the order). Table 4 shows the results for the Hermite interpolation. The computation time of the Hermite method is shorter than that of the Newton method by around 30% and of the Lagrange method by around 50%. Furthermore, the accuracy of all the orders is improved. The best accuracy is achieved for order 8 with a standard deviation in the radial component of 0.339 mm. Figures 21 and 22 illustrate the interpolation error of order 8 in the Cartesian (XYZ) coordinates and in the RTN coordinates compared to the orbit function, respectively.

In all the tested orders, the mean values of the radial component are of the same magnitude, except for order 5 using the Lagrange and Newton methods (mean = 0.982 mm). In order to know what could be the reason behind this offset, the behavior of the interpolation over the Cartesian coordinates system is examined. Since both methods provide identical results, the following figures are results from the Lagrange interpolation method only. Figures 23 and 24 demonstrate the error of the interpolation over the full time series, plotted together with the real orbit values of satellite

X, Y, and Z coordinates and the radial, transverse, and normal coordinate differences, respectively. It can be seen that the smallest absolute interpolation errors in the Cartesian coordinates occur when the component is close to 0. Conversely, the largest absolute interpolation errors occur at the maximum absolute values of X, Y, and Z. This behavior is no longer distinguished for higher orders, such as order 7 (Figure 25). Furthermore, there is no more an offset in the radial direction for the order 7 in Figure 26. Therefore, using the 5th order interpolation method is not recommended in the orbit interpolation application.

A closer look at the behavior of the interpolation errors of Cartesian coordinates, as well as on the behavior of the orbit function compared to the error in the radial component can be seen in Figure 27, where in both cases the first 100 epochs are taken, i.e. between 2004-07-18 00:00:00 and 2004-07-18 01:41:30 with a 60-second time step. It can be observed that the interpolation error in the radial direction has peaks that are closer to zero around the strong curvatures in the X and Z axes and around the slope line in the Y axis. This assumption is also valid when taking another interval of 100 epochs inside the full orbit arc (Figure 28). However, the correlation between the curvature of the orbit and the interpolation error cannot be validated.

Table 2: Interpolation statistics using Lagrange interpolation method of different orders with the sliding window approach.

Order	time (s)	std R (mm)	std T (mm)	std N (mm)	abs. mean R (mm)	abs. mean T (mm)	abs. mean N (mm)
5th	1.384	0.3838	0.3742	0.4898	0.9819	0.099	0.0005
6th	1.445	0.3822	0.3785	0.3805	0.0029	0.0179	0.0022
7th	1.468	0.3801	0.3762	0.3784	0.0028	0.0098	0.0023
8th	1.495	0.3844	0.3807	0.3831	0.0036	0.0098	0.0023
9th	1.536	0.3829	0.3793	0.3815	0.0037	0.0097	0.0023

Table 3: Interpolation statistics using Newton interpolation method of different orders with the sliding window approach.

Order	time (s)	std R (mm)	std T (mm)	std N (mm)	abs. mean R (mm)	abs. mean T (mm)	abs. mean N (mm)
5th	1.279	0.3838	0.3742	0.4898	0.9819	0.0990	0.0005
6th	1.277	0.3822	0.3785	0.3805	0.0029	0.0179	0.0022
7th	1.266	0.3801	0.3762	0.3784	0.0028	0.0098	0.0023
8th	1.276	0.3844	0.3807	0.3831	0.0036	0.0098	0.0023
9th	1.276	0.3829	0.3793	0.3815	0.0037	0.0097	0.0023

Table 4: Interpolation statistics using Hermite interpolation method of different orders with the sliding window approach.

Order	time (s)	std R (mm)	std T (mm)	std N (mm)	abs. mean R (mm)	abs. mean T (mm)	abs. mean N (mm)
5th	0.978	0.3430	0.3376	0.3404	0.0037	0.0097	0.0024
6th	0.975	0.3400	0.3347	0.3379	0.0038	0.0121	0.0023
7th	0.983	0.3409	0.3355	0.3383	0.0038	0.0098	0.0023
8th	0.996	0.3388	0.3335	0.3366	0.0039	0.0119	0.0023
9th	0.994	0.3394	0.3341	0.3369	0.0039	0.0098	0.0024

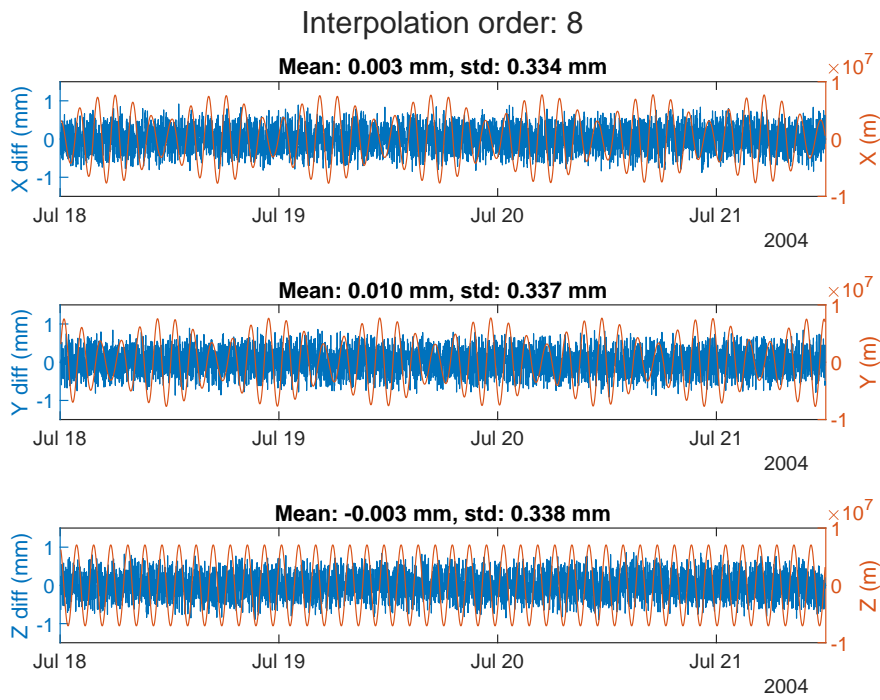


Figure 21: (Left axis) 8th order Hermite interpolation error in the Cartesian coordinates. (Right axis) TOPEX/Poseidon orbit in the Cartesian coordinates.

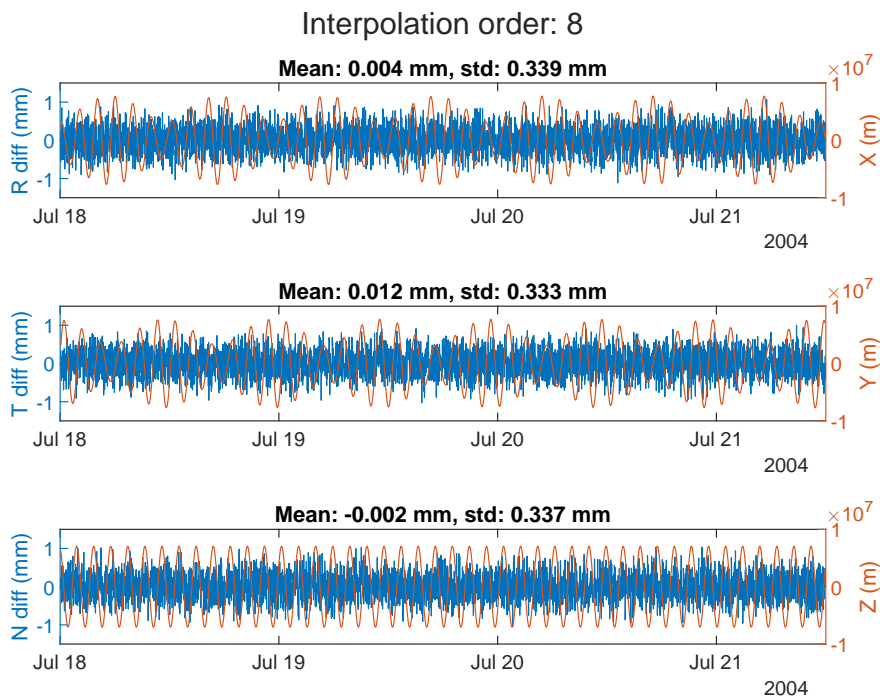


Figure 22: (Left axis) 8th order Hermite interpolation error in the RTN coordinates. (Right axis) TOPEX/Poseidon orbit in the Cartesian coordinates.

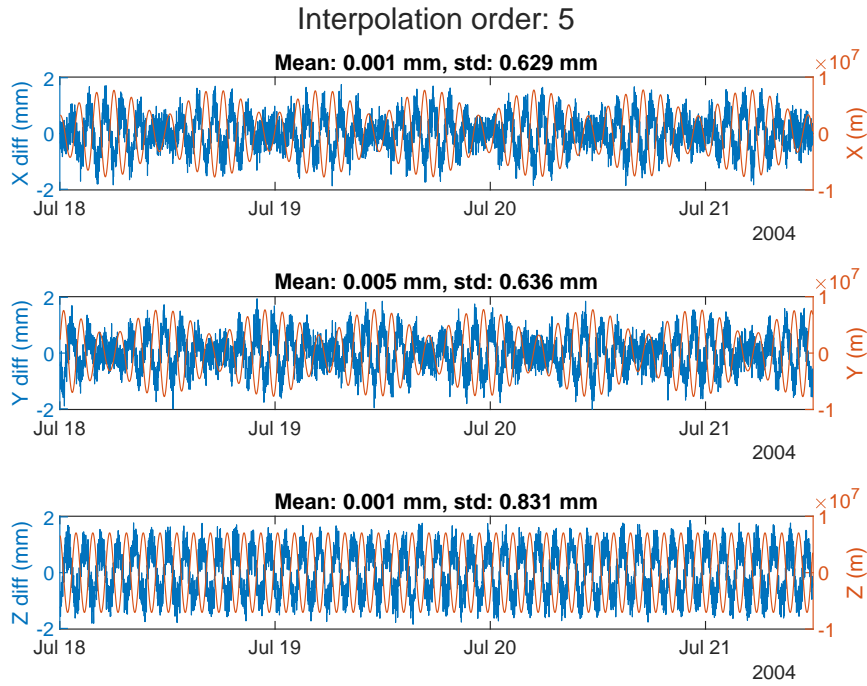


Figure 23: (Left axis) 5th order Lagrange interpolation error in the Cartesian coordinates.
(Right axis) TOPEX/Poseidon orbit in the Cartesian coordinates.

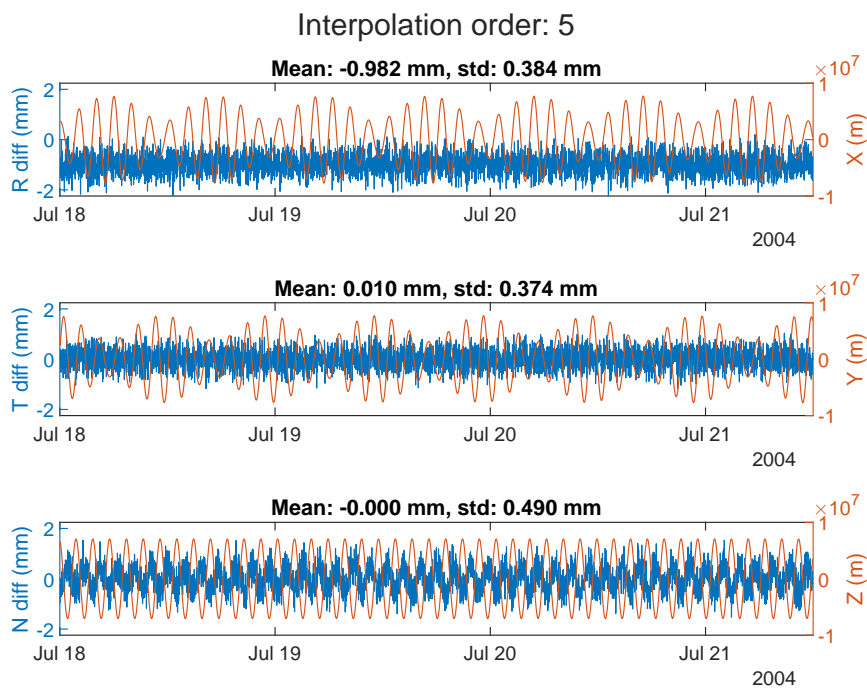


Figure 24: (Left axis) 5th order Lagrange interpolation error in the RTN coordinates.
(Right axis) TOPEX/Poseidon orbit in the Cartesian coordinates.

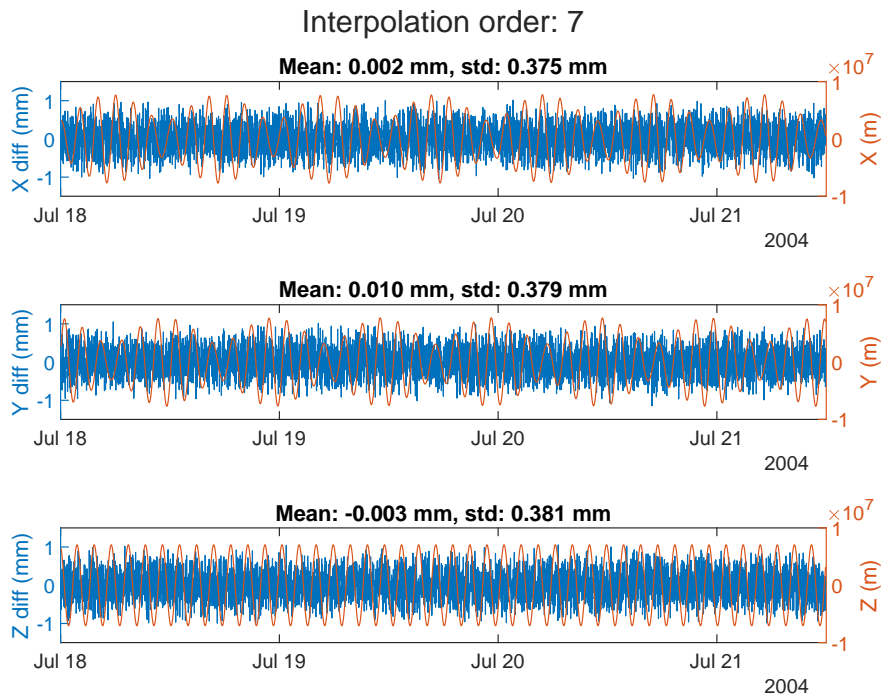


Figure 25: (Left axis) 7th order Lagrange interpolation error in the Cartesian coordinates. (Right axis) TOPEX/Poseidon orbit in the Cartesian coordinates.

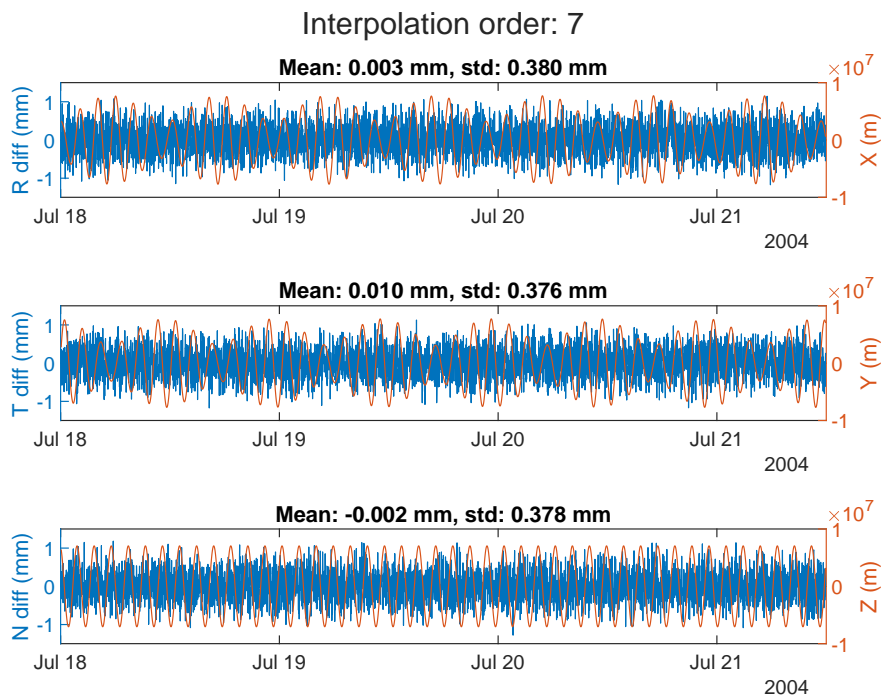
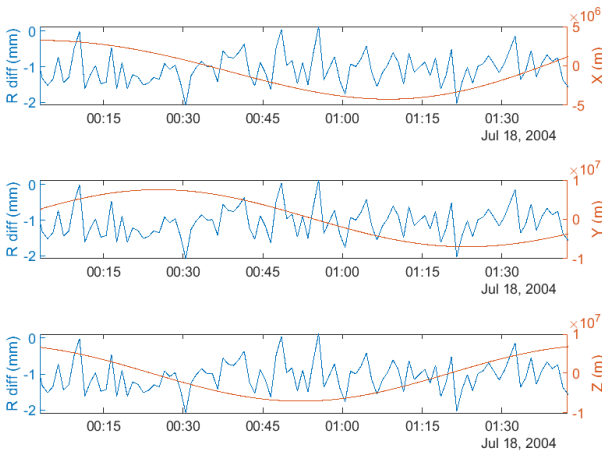


Figure 26: (Left axis) 7th order Lagrange interpolation error in the RTN coordinates. (Right axis) TOPEX/Poseidon orbit in the Cartesian coordinates.

Interpolation order: 5, mean R (mm): -1.055, std R (mm): 0.423



Interpolation order: 5, mean R (mm): -1.055, std R (mm): 0.423

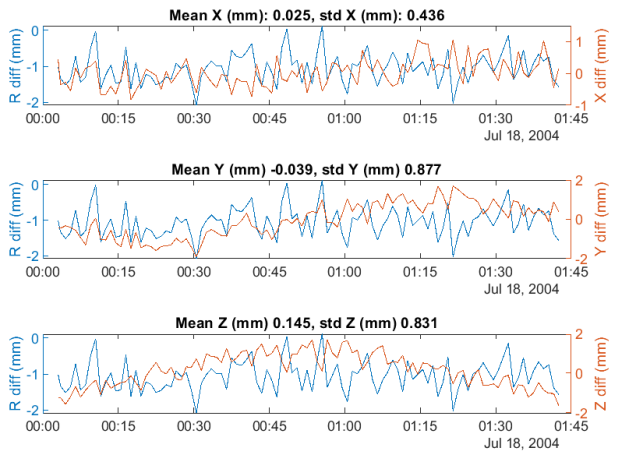
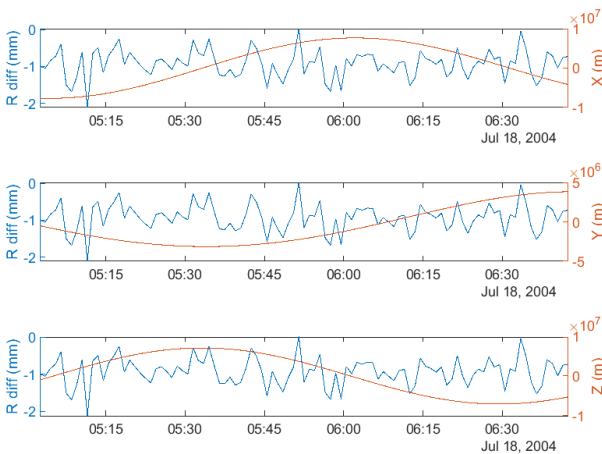


Figure 27: Lagrange interpolation of order 5, interpolation error in the radial component with the orbit function in the Cartesian coordinates (left). Interpolation error in the radial component with interpolation error in the Cartesian coordinates (right).

Interpolation order: 5, mean R (mm): -0.926, std R (mm): 0.371



Interpolation order: 5, mean R (mm): -0.926, std R (mm): 0.371

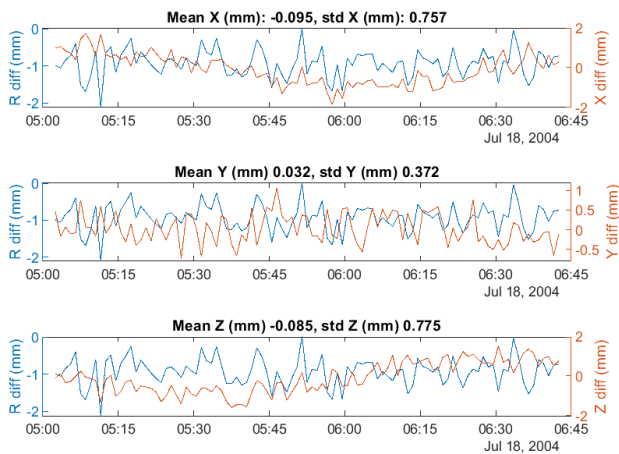


Figure 28: Lagrange interpolation of order 5, interpolation error in the radial component with the orbit function in the Cartesian coordinates (left). Interpolation error in the radial component with interpolation error in the Cartesian coordinates (right).

3.2.2.2 Middle-point interpolation approach

The basic idea of the middle-point interpolation is to interpolate both solutions, i.e. the previously called reference and non-reference solutions, to the points in the middle between the time instants of both solutions (Figure 29). This helps to reduce the time between the nodes and the interpolation points, and to eliminate the large interpolation errors when taking the differences between the 2 solutions.

Figure 29 is based on the same orbits as illustrated in Figure 19. However, a new reference orbit is introduced at the time instants being in the middle between the time instants of the two orbits. In this test, the 1-second orbit is used as a reference orbit with a 15-second step size (Section 3.2.1.1) to which the two orbits (1^{st} and 2^{nd}) are interpolated. The difference between the two interpolated orbits will be the interpolation error. Note that the sliding window is used when using either Newton or Lagrange interpolation methods in this approach. Hence, in this test, both the sliding window and the middle-point approaches are combined. The following tables (Table 5, Table 6, and Table 7) show the results obtained when using the 2 approaches together. The results of the Newton and Lagrange methods are slightly enhanced when using the middle-point approach. Specifically, in order 5, which now has the best accuracy (standard deviation in R = 0.363 mm) compared to the other tested orders. As it was also observed in the previous test (Section 3.2.2.1), the orders with the odd number have better results than the orders with the even number (5^{th} and 7^{th} compared to 6^{th} and 8^{th}). The computation time, however, is significantly longer than in the previous test, where the program is approximately 34% slower for the Lagrange method and 24% slower for the Newton method.

The results of the Hermite method are less affected by implementing the middle-point approach. The best interpolation accuracy is also achieved with order 8. An improvement of 0.7% only (standard deviation = 0.336 mm) is achieved, which is minimal as opposed to the time difference that is 18% longer compared to when applying the sliding window approach only.

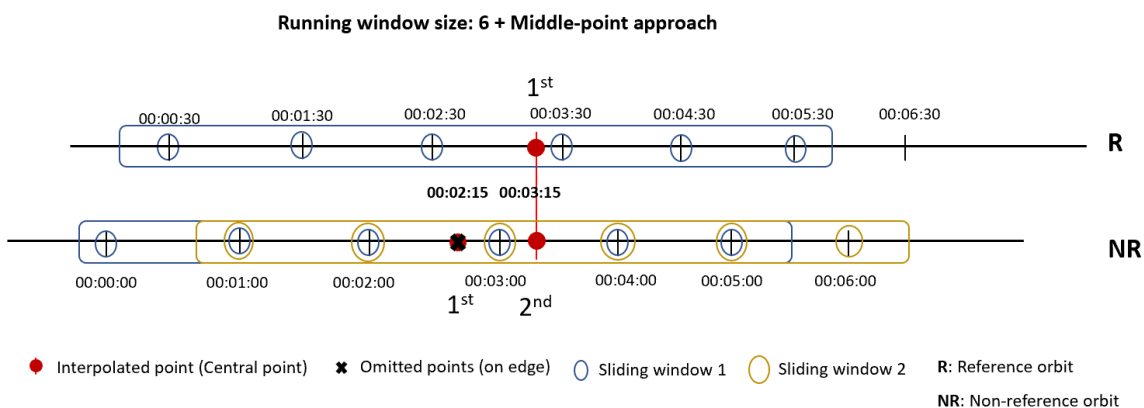


Figure 29: Middle-point interpolation concept.

Table 5: Interpolation statistics using Lagrange interpolation method of different orders with the sliding window and the middle-point approaches.

Order	time (s)	std R (mm)	std T (mm)	std N (mm)	abs. mean R (mm)	abs. mean T (mm)	abs. mean N (mm)
5th	2.107	0.3634	0.3625	0.3636	0.0035	0.0073	0.0023
6th	2.154	0.3712	0.3711	0.3720	0.0041	0.0126	0.0023
7th	2.245	0.3706	0.3693	0.3709	0.0036	0.0098	0.0023
8th	2.304	0.3755	0.3751	0.3762	0.0037	0.0098	0.0023
9th	2.368	0.3750	0.3738	0.3755	0.0038	0.0097	0.0023

Table 6: Interpolation statistics using Newton interpolation method of different orders with the sliding window and the middle-point approaches.

Order	time (s)	std R (mm)	std T (mm)	std N (mm)	abs. mean R (mm)	abs. mean T (mm)	abs. mean N (mm)
5th	1.687	0.3634	0.3625	0.3636	0.0035	0.0073	0.0023
6th	1.723	0.3712	0.3711	0.3720	0.0041	0.0126	0.0023
7th	1.741	0.3706	0.3693	0.3709	0.0036	0.0098	0.0023
8th	1.694	0.3755	0.3751	0.3762	0.0037	0.0098	0.0023
9th	1.721	0.3750	0.3738	0.3755	0.0038	0.0097	0.0023

So far, the results of the Newton, Lagrange, and Hermite interpolation methods have been discussed. Table 8 shows the results of the spline method. The spline method is usually of order 3 and does not require the sliding window, as it is a piece-wise interpolation method (see Section 3.1.5). In Table 8, the results of the spline interpolation using the middle-point approach are also displayed. It can be clearly seen that the middle-point approach brings significant improvement in the results of the spline method for the radial direction. However, the interpolation error in the transverse direction increases (from 0.01 to 6.06 mm). Additionally, as with the previous methods, the computation time is longer when using the middle-point approach. However, compared to approximately 90% enhancement in accuracy and the time when using the other methods, the slower computation time, in this case, can be overseen. The results shown are computed over the entire arc length, except

Table 7: Interpolation statistics using Hermite interpolation method of different orders with the sliding window and the middle-point approaches.

Order	time (s)	std R (mm)	std T (mm)	std N (mm)	abs. mean R (mm)	abs. mean T (mm)	abs. mean N (mm)
5th	1.201	0.3409	0.3397	0.3424	0.0037	0.0138	0.0022
6th	1.221	0.3371	0.3363	0.3388	0.0038	0.0136	0.0023
7th	1.245	0.3388	0.3377	0.3405	0.0038	0.0139	0.0023
8th	1.220	0.3363	0.3354	0.3381	0.0037	0.0139	0.0024
9th	1.216	0.3373	0.3363	0.3392	0.0038	0.0140	0.0024

for the first 7 and last 7 epochs, which are omitted to avoid the effect of the Runge phenomenon.

Table 8: Interpolation statistics using spline interpolation with and without the middle-point (MP) approach

Approach	time (s)	std R (mm)	std T (mm)	std N (mm)	abs.mean R (mm)	abs.mean T (mm)	abs.mean N (mm)
Without MP	0.0092	3.4269	0.6312	38.2162	175.1706	0.0110	0.2809
With MP	0.0155	0.4563	0.3823	1.3770	0.0031	6.0571	0.0008

In conclusion, spline interpolation is the fastest method, followed by Hermite, Newton, then Lagrange methods. The best results are provided by the 8^{th} order Hermite interpolation with and without the middle-point approach. The middle-point approach is quite slow in the cases of Hermite, Newton, and Lagrange methods, however, it is acceptable in the case of spline interpolation. As a final recommendation, for highest interpolation accuracy (0.34 mm standard deviation in the radial direction), it is suggested to use Hermite interpolation of 8^{th} order. Whereas, for fastest interpolation with a reliable accuracy (0.46 mm standard deviation in the radial direction), the middle-point spline interpolation is recommended.

4. Analysis of orbit differences

The accuracy of altimetry satellite orbits is crucial for obtaining a high accuracy sea level height. Orbits of altimetry satellites are computed by different institutions using different observing techniques and various software at different integration time steps. Further improving the orbits is key to enhancing the overall accuracy of the sea level heights. In this chapter, the program that is used for orbit comparison, as well as analysis techniques with a focus on spectral analysis approaches, are discussed.

4.1. Program for orbit comparison of altimetry satellites

The MATLAB program was developed at the DGFI-TUM for the computation of differences of altimetry satellite orbits, which were derived internally at the DGFI-TUM or externally at other institutes. The program is capable of reading files in SP1, SP3c, SP3d, and SP4 formats¹. To run the program, the user shall define the satellite name, the institutes that derived the orbits, the solution names, the time span of the desired computation, the reference time system, and other functionalities to be used by the program, such as transformation between different coordinates systems, and time systems.

Orbit interpolation is one of the most important functions that help in making the comparison between different orbit solutions possible. The user has the possibility to use one of the 4 interpolation methods, namely, spline, Lagrange, Newton, or Hermite interpolation, as well as to choose whether to use the middle-point approach or not (cf. Section 3.2.2.2). Besides that, there are many details that are necessary to consider, such as the handling of orbit maneuvers and gaps. Moreover, in order to avoid outliers around orbit maneuvers, gaps, and at the edges of the investigation interval due to the Runge phenomenon when using spline interpolation, the exclusion of the epochs at those events is crucial for precise comparison results. Another important measure with the intention to reduce interpolation errors is to unify the step sizes of different orbit solutions. This is important, especially when using the middle-point approach, where common middle points between solutions are used, and the 2 orbit solutions in comparison shall have equal step sizes (usually 30 seconds or 60 seconds).

The first orbit solution defined in the input options is going to be the reference solution, all other orbit solutions will be compared to the reference orbit. The script iterates over each orbit file of the reference solution and compares it to the overlapping arcs from other orbit solutions. As an output, for each arc, orbit differences in the Cartesian, ellipsoidal, and RTN coordinate systems, as well as the ellipsoidal coordinates, are saved in corresponding files. A summary file that contains a statistical analysis of the differences of each arc is printed, from which it is possible to compute the overall mean values of the statistics. There is another option to perform the comparison over the total defined time span. The output file will contain a summary of statistics of the full time span computation. Other output forms, such as plots of the differences at each arc or over the entire time

¹ <https://files.igs.org/pub/data/format>

span, can be handled. The options of plotting or printing in any coordinate system can be set by the user at the main function of the program.

After finalizing the computation of the orbit differences, it is possible to analyze the results with different techniques, such as studying the geographical distribution and applying a spectral analysis of the orbit differences. The geographical distribution of the orbit differences is illustrated with either of the 2 options: 1) to plot the orbit differences of several arcs according to the satellite locations in latitude and longitude, 2) or to plot an averaged value of overlapping arcs on a $1^\circ \times 1^\circ$ grid of latitude and longitude. Furthermore, a spectral analysis of possible periods in the orbit differences can be performed. For a reliable analysis, large outliers can be extracted with 2 options. By specifying a limit for the values not to exceed, e.g., any value that is larger than "10 cm" is extracted. Another option is to extract the values according to the "sigma rule", where the limit (SigVal) is calculated as follows:

$$SigVal = mean(orbit_differences) + multiplier \cdot sigma(orbit_differences), \quad (4.1)$$

and the multiplier can be any positive value.

In the following, the theory and quality test of possible spectral analysis methods are explained.

4.2. Spectral analysis

One analysis approach for detecting the dominant frequencies and periods of the orbit differences is spectral analysis. Deciding on which method is appropriate for this aim is not an easy task, since the orbits are subject to a variety of factors that might affect the results of the analysis, such as orbit maneuvers, gaps, the time the satellite spends in shadow, and other influences. There exist various broad categories of spectral analysis methods, such as Fourier methods, phase-folding methods, least-squares methods, and Bayesian approaches. The focus of this study will be on Fourier-based methods, with their advantages and disadvantages, which are discussed in the following. For further details and references on other methods, see VanderPlas (2018).

4.2.1. Fourier transform

As it is defined and derived by VanderPlas (2018), the Fourier transform decomposes complex-shaped signals to simple sinusoids. To transform a signal from the time domain to the frequency domain, the function of the continuous Fourier transform reads:

$$G(f) = \int_{-\infty}^{+\infty} g(t)e^{-2\pi ift} dt, \quad (4.2)$$

with $G(f)$ and $g(t)$ the signal in the frequency and the time domain, respectively, and $i = \sqrt{-1}$ denoting the imaginary unit. The complex exponential is derived from Euler's formula:

$$e^{ix} = \cos x + i \cdot \sin x.$$

Assuming that the signal is regularly sampled with a step size Δt , it is possible to write the integral

in Eq. 4.2 as:

$$G(f) = \sum_{n=0}^N g(n\Delta t) e^{-2\pi i f n \Delta t} dt. \quad (4.3)$$

Having n as the current sample and N as the total number of samples, the frequency range Δf can be represented as $\Delta f = 1/(N\Delta t)$. With k being the current frequency and $g_n = g(n\Delta t)$, the equation becomes:

$$G(f) = \sum_{n=0}^N g_n e^{-2\pi i k n / N} dt \quad (4.4)$$

The frequency range is defined as complying with the Nyquist limit, which states that in order for the information in a regularly sampled signal to be recovered, the total length of the signal shall be at least twice the longest period. The frequency is computed starting from 0 through the highest frequency that can be achieved considering the Nyquist limit, having the frequency range Δf as the sampling interval. The amplitude, i.e. the height of the peak of a signal, can simply be computed by taking the magnitude of the Fourier transform.

In order to quantify the contribution of each frequency in a signal, the square of the magnitude of the Fourier transform is calculated which is known as the power spectral density (VanderPlas, 2018). For a discrete number of samples, the classical periodogram, which is an estimate of the power spectral density $P(f)$, can be defined as:

$$P(f) = \frac{|\sum_{n=0}^N g_n e^{-2\pi i f t_n} dt|^2}{N} \quad (4.5)$$

The Fourier transform is a basic method for detecting the frequencies of a signal. However, this method is limited to a regularly spaced signal and is dependent on the length of the time series. In the following, other methods that are able to overcome these limitations are discussed.

4.2.2. Lomb-Scargle periodogram

The advantages of the Lomb-Scargle periodogram are that it is possible to use it for irregularly sampled data and that it is not majorly affected if the data contains gaps as in Fourier transform (VanderPlas, 2018).

The Lomb-Scargle periodogram (P_{LS}) is different from the classical periodogram in Eq. 4.5 by the functions in the denominator. These functions of time and frequency are chosen so that the distribution of the Lomb-Scargle periodogram can be computed analytically and is independent of the global time shift of the data (VanderPlas, 2018). This leads to:

$$P_{LS}(f) = \frac{1}{2} \frac{(\sum_n g_n \cos(2\pi f [t_n - \tau]) dt)^2}{\sum_n \cos^2(2\pi f [t_n - \tau])} + \frac{1}{2} \frac{(\sum_n g_n \sin(2\pi f [t_n - \tau]) dt)^2}{\sum_n \sin^2(2\pi f [t_n - \tau])}, \quad (4.6)$$

and τ is defined as:

$$\tau = \frac{1}{4\pi f} \tan^{-1} \left(\frac{\sum_n \sin(4\pi f t_n)}{\sum_n \cos(4\pi f t_n)} \right), \quad (4.7)$$

so that it secures the condition of time-shift invariance. In this case, the amplitude of the signal can be computed by taking the square root of the defined periodogram scaled to the length of the signal. The frequency is computed starting from the frequency of the sampling interval, since the Lomb-Scargle periodogram, unlike Fourier transform, cannot carry out a frequency of zero (Trauth, 2020).

With this definition, the solution of P_{LS} will be equal to the least-squares fit of a sinusoidal function to the data at every frequency, the function is composed of sine and cosine and can be written as (Trauth, 2020):

$$y(t) = A\cos(2\pi ft) + B\sin(2\pi ft). \quad (4.8)$$

However, Zechmeister and Kurster (2009) stated that the Lomb-Scargle periodogram assumes that the data has uncorrelated white noise and that the mean of the data is equal to the mean of the fitted sinusoid. To overcome these assumptions, different techniques shall be considered. Therefore, the authors introduced the generalized Lomb-Scargle periodogram, in which they resolved the problem of equal means by adding an offset " c " to the Eq. 4.8. This method is also known as the "floating-mean periodogram". The mean and the data are weighted to the inverse of the squared of the measurement's uncertainty, and then, they are subtracted from each other. The authors also suggested normalization techniques to calculate the false alarm probability so that any trend that is only related to statistical errors and not due to a real period is discarded from the periodicity detection.

Another assumption of the Lomb-Scargle periodogram is that the frequency of the data is stationary or non-evolutionary throughout the time series and in the presence of time-varying frequency, it will result in a mean state of the signal (Kalicinsky et al., 2020). The authors present a solution to the problem arising from this assumption by using a sliding window, in which the same procedure of calculating the periodogram is applied to the parts of the time series that are inside the window. This will enable the detection of amplitudes and frequencies that are varying with time. However, this approach becomes inefficient if the length of the time series is very long and inaccurate, if the high or low-frequency range is not contained inside the window.

4.2.3. Wavelet analysis

Another alternative for detecting evolutionary frequencies is to apply wavelet analysis. It is an efficient method for detecting and resolving time-varying frequencies with high accuracy. This is possible due to the fact that the wavelet, from its name, decomposes the signal into small waves $\psi_{a,b}(t)$ from a mother wavelet $\psi(t)$ under 2 conditions: the wavelet function should have a zero mean and should be localized in time and space. Eq. 4.9 shows the wavelet derived by defining the scale (a) as a dilation and the position in time (b) as a translation of the mother wavelet (Torrence and Compo, 1998; Trauth, 2020).

$$\psi_{a,b}(t) = \frac{1}{a^{1/2}} \psi\left(\frac{t-b}{a}\right) \quad (4.9)$$

The so-called wavelet transforms $W(b, a)$ of a signal is obtained by taking the integral of the convolution of the signal $y(t)$ with the mother wavelet $\psi(t)$:

$$W(b, a) = \frac{1}{a^{1/2}} \int \psi * \left(\frac{t-b}{a} \right) y(t) dt \quad (4.10)$$

There exist different mother wavelets in the literature, a commonly used mother wavelet is "Morlet wavelet" and is defined as (Torrence and Compo, 1998; Trauth, 2020):

$$\psi_0(\eta) = \pi^{-1/4} e^{i\omega_0\eta} e^{-\eta^2/2}, \quad (4.11)$$

where η is the non-dimensional time and ω_0 is defined as the number of oscillations within the wavelet (the wave number).

As the wavelet is dependent on the scale and not on the frequency, one should be careful when converting from the scale to the frequency. In the simplest case, the "Morlet wavelet" is almost equivalent to the inverse of the frequency, i.e. the period, for more details please refer to Torrence and Compo (1998). The signal's peak at a time instant is equal to the amplitude of the wavelet transform. The disadvantage of the wavelet analysis is that it requires uniformly sampled data, and hence, it cannot perform as intended in case of the existence of gaps in the data (Trauth, 2020). Another disadvantage is that it is computationally extensive.

4.2.4. Testing the methods on an artificial signal

As discussed in Sections 4.2.1-4.2.3, each method has its advantages and disadvantages. Deciding on which method to use depends on the data and the goal of the analysis. In this section, a test is conducted on an artificial sine signal by defining different periods and amplitudes. The test is set up in a way to resemble the time series of the orbit, such that it has a step size of 60 seconds, the length of the time span might reach up to 14 years, and the periods are defined to be similar to the known periods of the orbit. The 3 main periods are: 1) the half of the draconitic period ($T = 58.765$ days), the draconitic period ($T = 117.53$ days) is the period of the sun's elevation angle with respect to the orbit plane to control the satellite's orientation in order to maintain the nadir-pointing attitude and the sun-pointing of the solar arrays, 2) the repeat cycle ($T = 9.9156$ days), which is the time that the satellite takes to revisit the same ground track, and 3) the nodal period ($T = 112.4267$ minutes), also known as the revolution period, which is the time needed by an altimetry satellite to orbit around the Earth. Other details, such as the white noise and data gaps, are included, and the Nyquist limit of having the length of the signal at least 2 times the maximum period is also secured in this test. However, the number of full oscillations covered in the signal should be larger than 2 for better analysis results.

For each of the discussed methods, MATLAB has its built-in functions, namely 'fft'¹ for fast Fourier transform, 'plomb'² for Lomb-Scargle periodogram, and 'cwt'³ for the continuous wavelet transform.

¹ <https://de.mathworks.com/help/matlab/ref/fft.html>

² <https://de.mathworks.com/help/signal/ref/plomb.html>

³ <https://de.mathworks.com/help/wavelet/ref/cwt.html>

The input to the functions is a signal with one (or more) of the periods mentioned above. There are also other input options, such as the length of the signal, the sampling rate, or the time instants. The output of the 'fft' function is the Fourier transform of the signal, whereas the outputs of the 'plomb' function are the power spectral density as well as the frequency. In the case of the function 'cwt', the outputs are the wavelet transform, the period or the frequency, and the cone of influence, where the information might be inaccurate due to being at the edges¹. There is an option to increase the resolution of the fast Fourier transform and the Lomb-Scargle periodogram, as stated in the MATLAB documentation of both methods, by increasing the length of the signal. The fast Fourier transform can make use of the so-called "zero-padding" method, in which the signal is filled with zeros at the end to make the length of the signal in the power of 2, at which the 'fft' function performs even faster. On the other hand, the option for the Lomb-Scargle periodogram is similar but not exactly the same as the zero-padding method. In this case, an oversampling factor can be fixed "to interpolate or smooth a spectrum" as defined in the MATLAB documentation². However, the oversampling method requires large memory for the processing of a long time series, therefore, it is disregarded for this test. Since both methods, the Fourier transform and the Lomb-Scargle methods, are dependent on the length of the time span, the following test is performed using these 2 methods.

The test is done over artificial "sine" signals with a randomly set amplitude, and the periods are one of the periods discussed in the beginning of this section. The first scenario is done over gap-free and noise-free signals. The power spectral density and the frequencies of the signals are computed iteratively. For the repeat cycle (9.9156 days) and the nodal period (112.4267 minutes, used as 0.0781 days from now on), the test is initiated with a time series of 240 days (24 times the repeat cycle (around 10 days) in order to secure the full recovery of the signal). The length of the time series increases per iteration by 2 days until reaching a total length of 2 years. These 2 signals are studied in 2 cases, individually and in the case when they are combined together. The third signal, which is half of the draconitic period (58.765 days), is only studied individually starting from a length of time series of around 3.8 years. The length of the time series increases cumulatively every 20 days until reaching 14 years from the starting point, which is around the maximum length of time that an altimetry satellite can be in function. Tables 9, 10 and Figures 30-35 show the results of the periods and amplitudes reconstructed in the gap-free and noise-free scenario, where the first column includes the signal number, "T" denotes the period, "composed" means that the signal is reconstructed from a combination of 2 signals, and "Relative Diff. %" is calculated as:

$$RelativeDiff.\% = \frac{obtained - original}{original} \cdot 100. \quad (4.12)$$

From Table 9 and Figures 30, 32, and 34, all 3 methods provide very small relative differences varying for each signal from 0.00 to 0.16% in the absolute form. The smallest relative differences are obtained when using the zero-padding fast Fourier transform. The values obtained when implementing the Lomb-Scargle method have a periodic behavior over time, which implies that the function might stabilize and the error will be minimum at infinity. The zero-padding fast Fourier

¹ <https://de.mathworks.com/help/wavelet/ref/cwt.html>

² <https://de.mathworks.com/help/signal/ref/plomb.html>

transform results in periods in the form of a straight line, as shown in Figures 30 and 34. Table 10 and Figures 31, 33, and 35 show the results for the amplitude reconstruction. The relative differences are in favor of the zero-padding fast Fourier transform with a maximum of 0.3%, whereas the Lomb-Scargle method results in a maximum relative difference of around 3%. On the other hand, the periodic behavior of the Lomb-Scargle method can also be observed in the amplitude obtained using the zero-padding fast Fourier transform, which also includes a drift from the real value toward the end of the tested time series. The standard Fourier transform shows large deviations from the original values that can reach up to 36%.

In summary of the gap-free and noise-free scenario, the maximum deviation of the Lomb-Scargle method can reach up to around 0.5% in the period and to about 3% in the amplitude reconstruction. The standard Fourier transform results in maximum period variations of 1.7% and amplitude variations of 36%. The zero-padding fast Fourier transform variations can reach up to around 0.2% in the period reconstruction and around 0.4% in the amplitude reconstruction, making it the most accurate method when the signal is gap-free and noise-free.

Table 9: Detection accuracy of specific periods in a gap-free and noise-free sine signal depending on the signal lengths in days. In bold are the values of minimum absolute relative differences.

Signal number	Original T (days)	Plomb	Standard FFT	Zero-padding FFT
		T (days)		
		Absolute max. relative difference		
1	58.765	59.0515	59.7334	58.6725
	Relative Diff. (%)	0.4876	1.6479	0.1574
2	9.9156	9.9623	10.0834	9.9123
	Relative Diff. (%)	0.4708	1.6919	0.0329
2 composed with 3	9.9156	9.9623	10.0834	9.9123
	Relative Diff. (%)	0.4708	1.6919	0.0329
3	0.0781	0.0780	0.0781	0.0781
	Relative Diff. (%)	0.0621	0.0149	0.0000
3 composed with 2	0.0781	0.0781	0.0781	0.0781
	Relative Diff. (%)	0.0035	0.0150	0.0002

4.2 Spectral analysis

Table 10: Detection accuracy of specific amplitudes in a gap-free and noise-free sine signal depending on the signal lengths in days. In bold are the values of minimum absolute relative differences.

Signal number	Original amplitude	Plomb	Standard FFT	Zero-padding FFT
		Amplitude		
		Absolute max. relative difference		
1	10	9.7375	6.3851	9.9663
	Relative Diff. (%)	2.6249	36.1495	0.3373
2	50	48.6373	31.8390	49.8291
	Relative Diff. (%)	2.7254	36.3220	0.3417
2 composed with 3	50	48.6374	31.8388	49.8293
	Relative Diff. (%)	2.7253	36.3223	0.3415
3	5	4.8732	3.1922	4.9991
	Relative Diff. (%)	2.5353	36.1552	0.0174
3 composed with 2	5	4.8728	3.1923	4.9949
	Relative Diff. (%)	2.5447	36.1547	0.1023

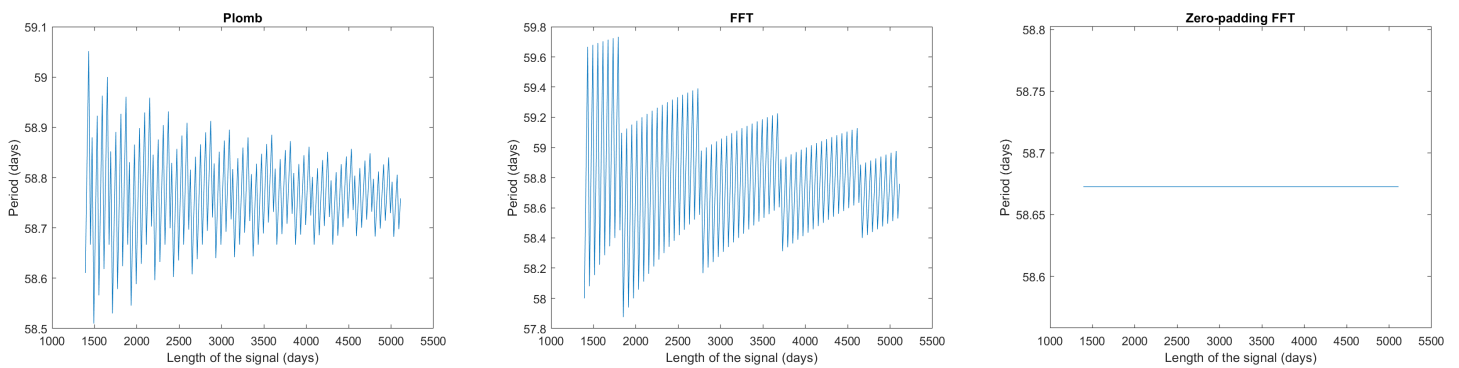


Figure 30: Detection accuracy of a period of 58.765 days in a gap-free and noise-free sine signal depending on the signal lengths in days using Lomb-Scargle method (plomb on the left), standard fast Fourier transform (middle), and zero-padding fast Fourier transform (right).

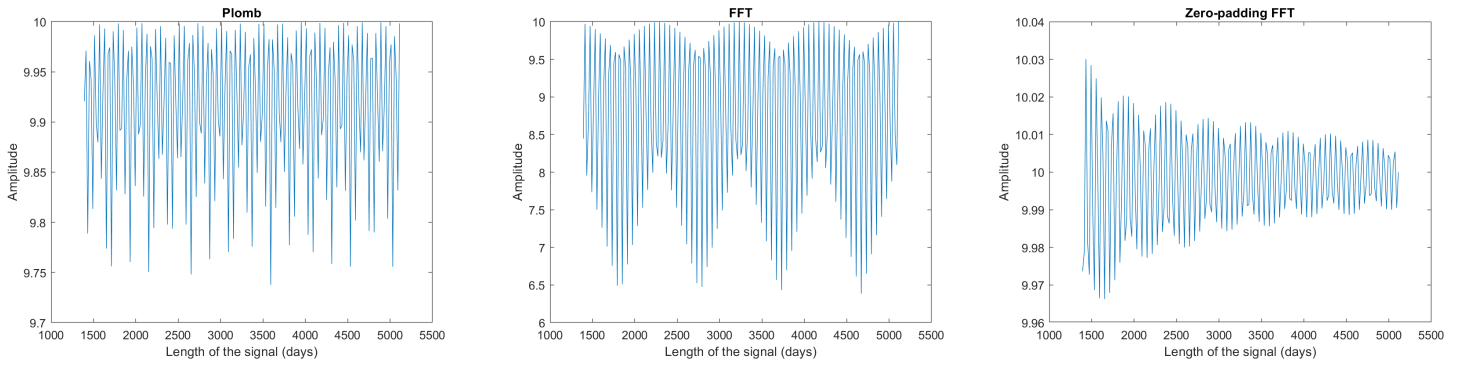


Figure 31: Detection accuracy of an amplitude of 10 in a gap-free and noise-free sine signal depending on the signal lengths in days using Lomb-Scargle method (left), standard fast Fourier transform (middle), and zero-padding fast Fourier transform (right).

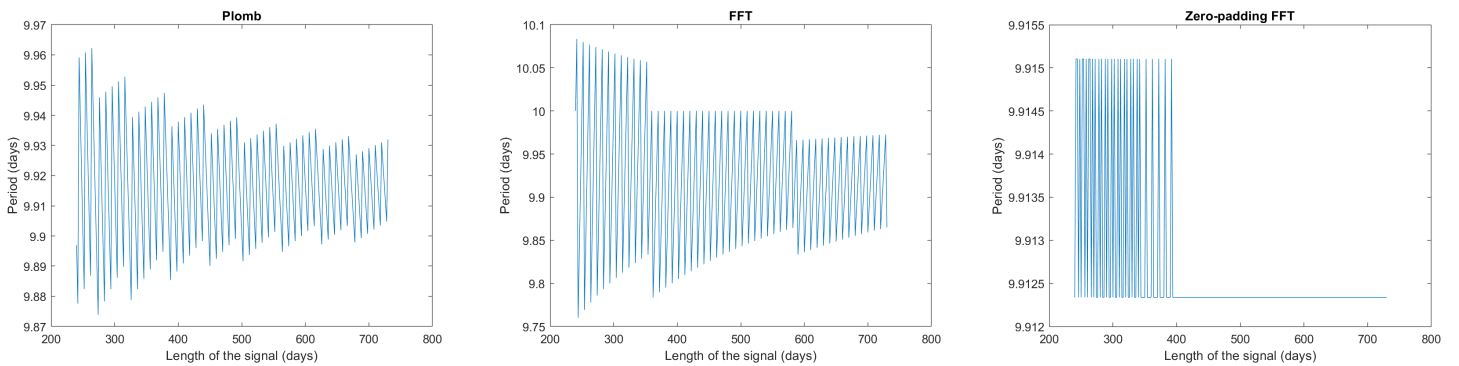


Figure 32: Detection accuracy of a period of 9,9156 days in a gap-free and noise-free sine signal depending on the signal lengths in days using Lomb-Scargle method (left), standard fast Fourier transform (middle), and zero-padding fast Fourier transform (right).

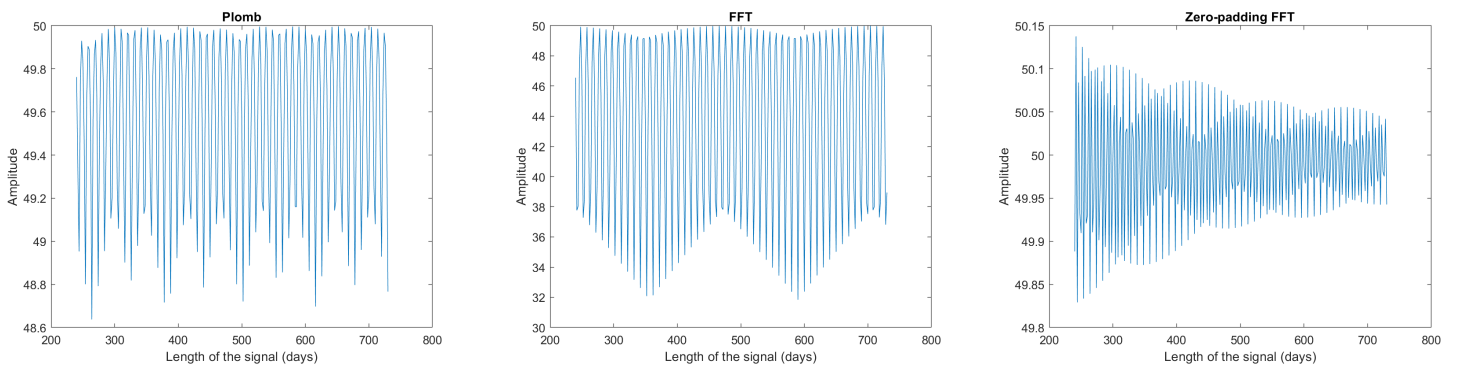


Figure 33: Detection accuracy of an amplitude of 50 in a gap-free and noise-free sine signal depending on the signal lengths in days using Lomb-Scargle method (left), standard fast Fourier transform (middle), and zero-padding fast Fourier transform (right).

4.2 Spectral analysis

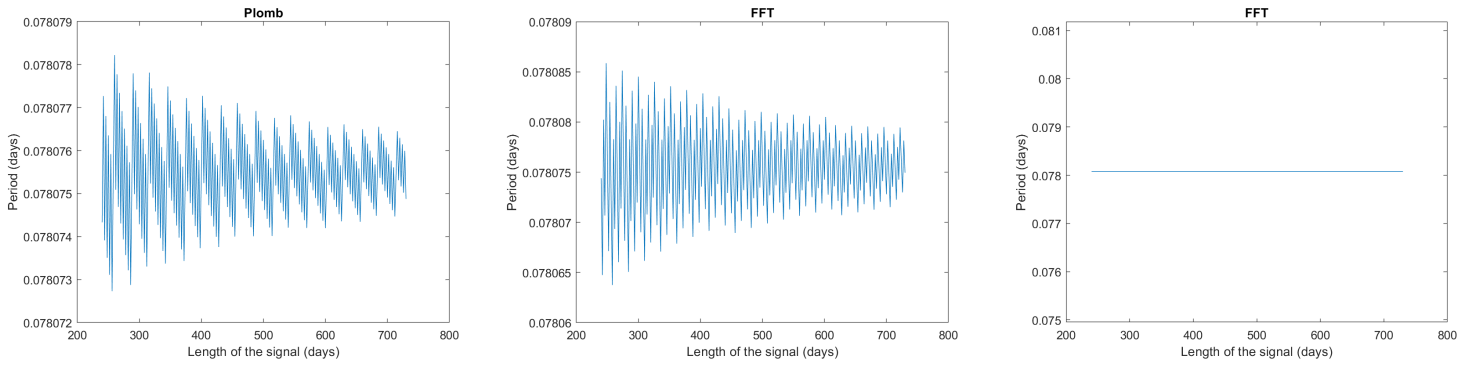


Figure 34: Detection accuracy of a period of 0.078075 days in a gap-free and noise-free sine signal depending on the signal lengths in days using Lomb-Scargle method (left), standard fast Fourier transform (middle), and zero-padding fast Fourier transform (right).

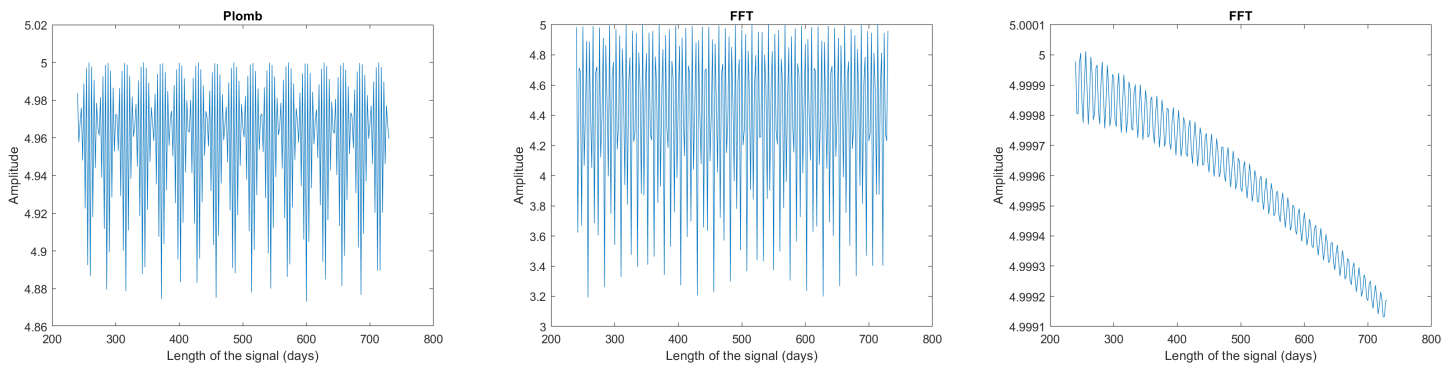


Figure 35: Detection accuracy of an amplitude of 5 in a gap-free and noise-free sine signal depending on the signal lengths in days using Lomb-Scargle method (left), standard fast Fourier transform (middle), and zero-padding fast Fourier transform (right).

The second scenario is when the signal contains gaps and Gaussian white noise. The gaps of the length of 0.4 days, 3.5 days, and 72 days are introduced to the signal at 3 days, 3 months, and 6 months from the beginning of the signal, respectively. Gaussian white noise is generated based on a predefined signal-to-noise ratio that is assumed to be 10 dB, this is done using the built-in MATLAB function 'awgn'¹. Similarly to the first scenario, Tables 11 and 12 and Figures from 36 to 41 show the results for this scenario. The results of the periods' reconstruction are displayed in Table 11, in which all the methods still have relatively small differences, however, in this case, the Lomb-Scargle method outperforms the zero-padding fast Fourier transform. In the figures, e.g., Figures 38 and 40, the effect of the gap on the fast Fourier transform method is well visible, whereas it is not observable in the Lomb-Scargle figure. The amplitude reconstruction is more challenging for these cases. In all 3 signals, the amplitude is best recovered by the Lomb-Scargle method, as seen in Table 12. The gaps-effect, specifically the 72-day-long gap is also distinguished in the amplitude figures, such as in Figure 39 and Figure 41. The reason for not detecting the influence of the gap on the signal of the 58.765 days period is that time is accumulated to a length of 14 years, and the gap is added only at the end of the first year. Therefore, it is possible for the signal to recover from the gap effect after a certain time. In summary, the Lomb-Scargle method outperforms

¹ <https://de.mathworks.com/help/comm/ref/awgn.html>

the standard and the zero-padding fast Fourier transform, when the signal contains gaps and noise. The maximum deviation of the Lomb-Scargle method can reach up to 0.5% in the period, and up to 4% in the amplitude reconstruction. On the other hand, the standard fast Fourier transform method results in maximum variations of the reconstructed periods of around 7% and amplitudes of around 53%. The zero-padding fast Fourier transform can reach up to 5% in the period and 41% in the amplitude reconstruction.

To conclude, the Lomb-Scargle method produces more stable results than the fast Fourier transform methods. This is specifically true when the signal contains gaps and noise, which is mostly the case in orbit solutions. Therefore, the Lomb-Scargle method is used for spectral analysis of orbit differences.

Table 11: Detection accuracy of specific periods in a sine signal with gaps and noise depending on the signal lengths in days. In bold are the values of minimum absolute relative differences.

Signal number	Original T (days)	Plomb	Standard FFT	Zero-padding FFT
		T (days)		
		Absolute max. relative difference		
1	58.765	59.0515	57.3012	58.2878
	Relative Diff. (%)	0.4876	2.4910	0.8121
2	9.9156	9.9623	9.2614	9.4764
	Relative Diff. (%)	0.4709	6.5978	4.4291
2 composed with 3	9.9156	9.9623	9.2614	9.4790
	Relative Diff. (%)	0.4709	6.5978	4.4036
3	0.0781	0.0781	0.0781	0.0781
	Relative Diff. (%)	0.0036	0.0505	0.0367
3 composed with 2	0.0781	0.0781	0.0781	0.0781
	Relative Diff. (%)	0.0037	0.0505	0.0367

4.2 Spectral analysis

Table 12: Detection accuracy of specific amplitudes in a sine signal with gaps and noise depending on the signal lengths in days. In bold are the values of minimum absolute relative differences.

Signal number	Original amplitude	Plomb	Standard FFT	Zero-padding FFT
		Amplitude		
		Absolute max. relative difference		
1	10	9.7316	6.2119	9.0381
	Relative Diff. (%)	2.6842	37.8813	9.6191
2	50	48.0893	23.2822	29.5438
	Relative Diff. (%)	3.8214	53.4355	40.9123
2 composed with 3	50	48.1404	23.2958	29.5626
	Relative Diff. (%)	3.7191	53.4083	40.8748
3	5	4.8434	2.4486	3.2083
	Relative Diff. (%)	3.1324	51.0290	35.8348
3 composed with 2	5	4.8181	2.4577	3.1864
	Relative Diff. (%)	3.6376	50.8464	36.2728

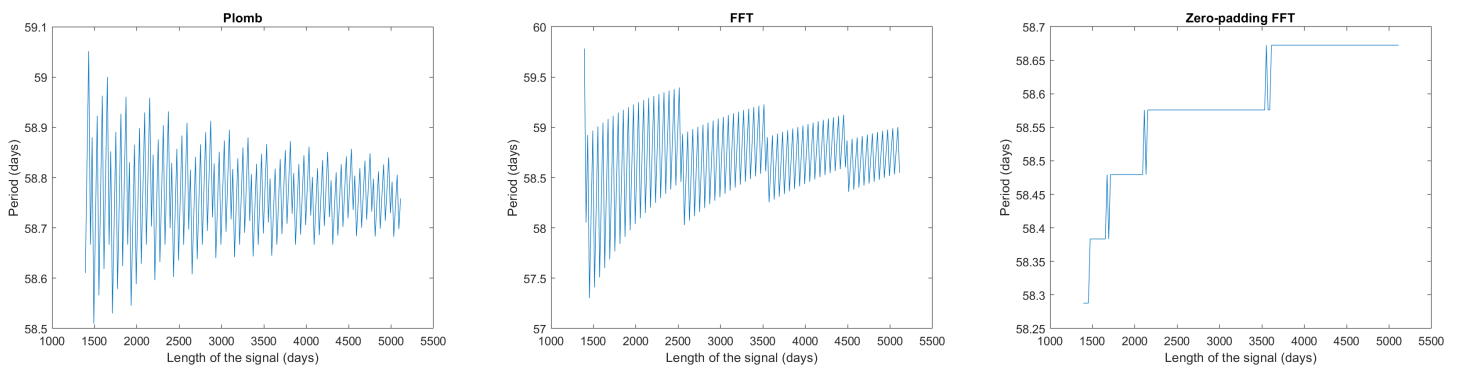


Figure 36: Detection accuracy of a period of 58.765 days in a sine signal with gaps and noise depending on the signal lengths in days using Lomb-Scargle method (left), standard fast Fourier transform (middle), and zero-padding fast Fourier transform (right).

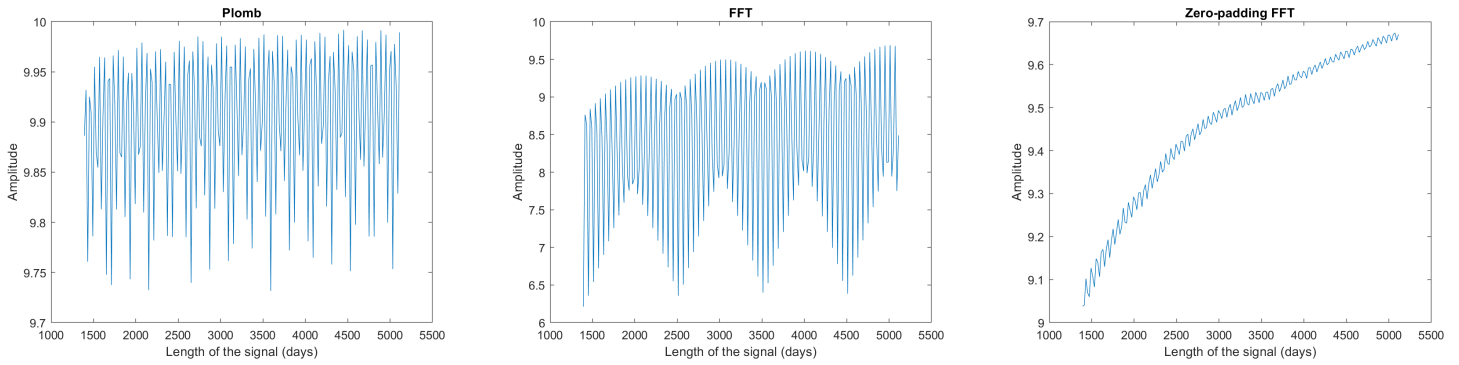


Figure 37: Detection accuracy of an amplitude of 10 in a sine signal with gaps and noise depending on the signal lengths in days using Lomb-Scargle method (left), standard fast Fourier transform (middle), and zero-padding fast Fourier transform (right).

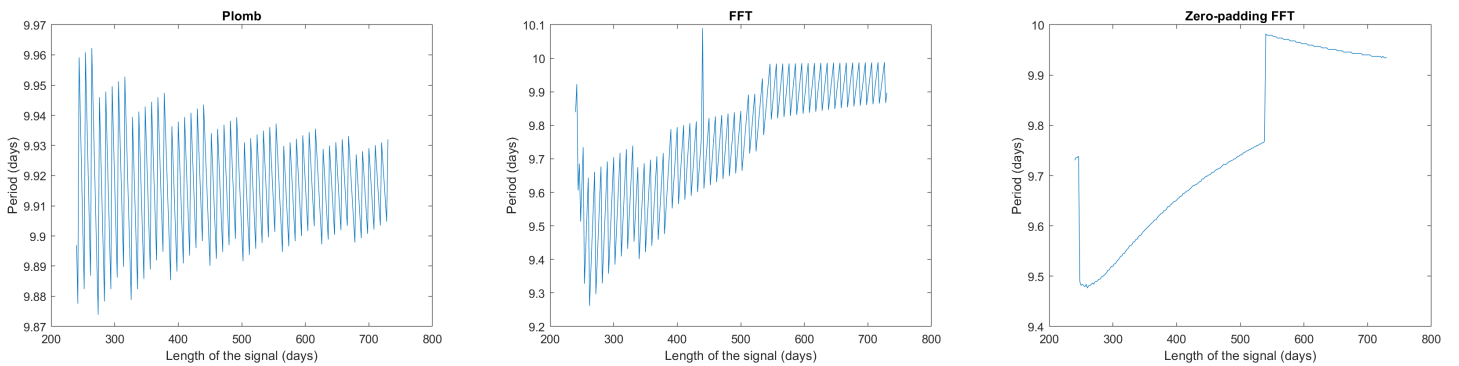


Figure 38: Detection accuracy of a period of 9.9156 days in a sine signal with gaps and noise depending on the signal lengths in days using Lomb-Scargle method (left), standard fast Fourier transform (middle), and zero-padding fast Fourier transform (right).

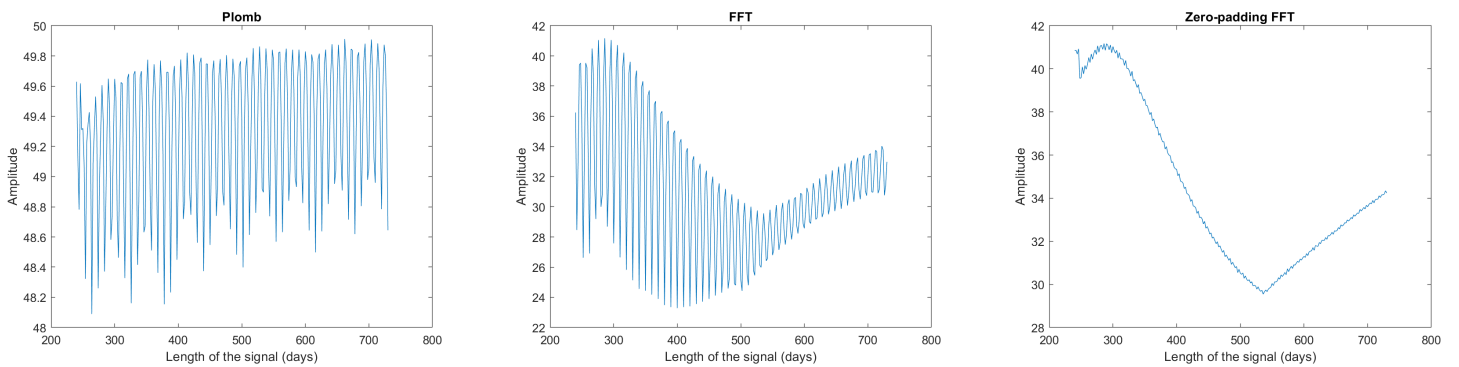


Figure 39: Detection accuracy of an amplitude of 50 in a sine signal with gaps and noise depending on the signal lengths in days using Lomb-Scargle method (left), standard fast Fourier transform (middle), and zero-padding fast Fourier transform (right).

4.2 Spectral analysis

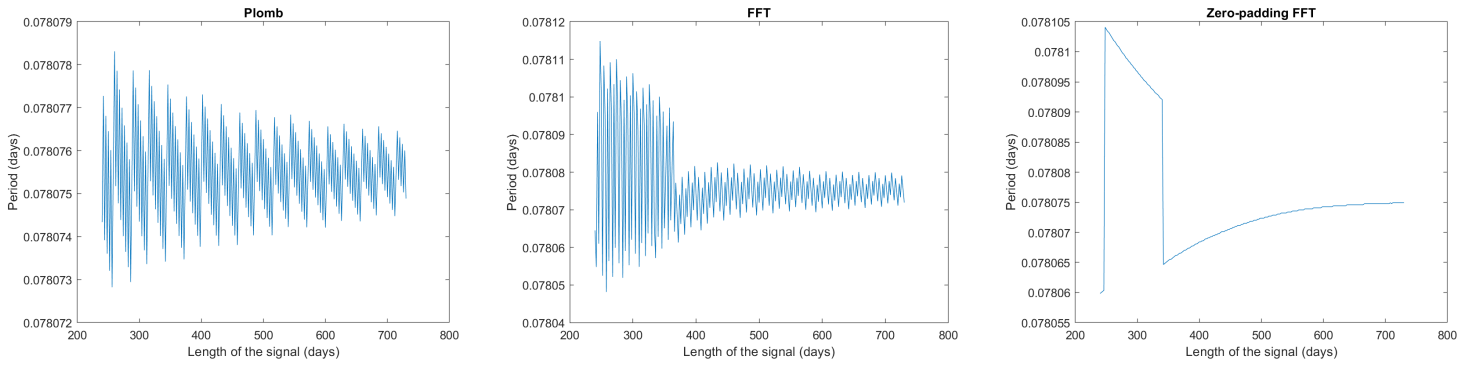


Figure 40: Detection accuracy of a period of 0.078075 days in a sine signal with gaps and noise depending on the signal lengths in days using Lomb-Scargle method (left), standard fast Fourier transform (middle), and zero-padding fast Fourier transform (right).

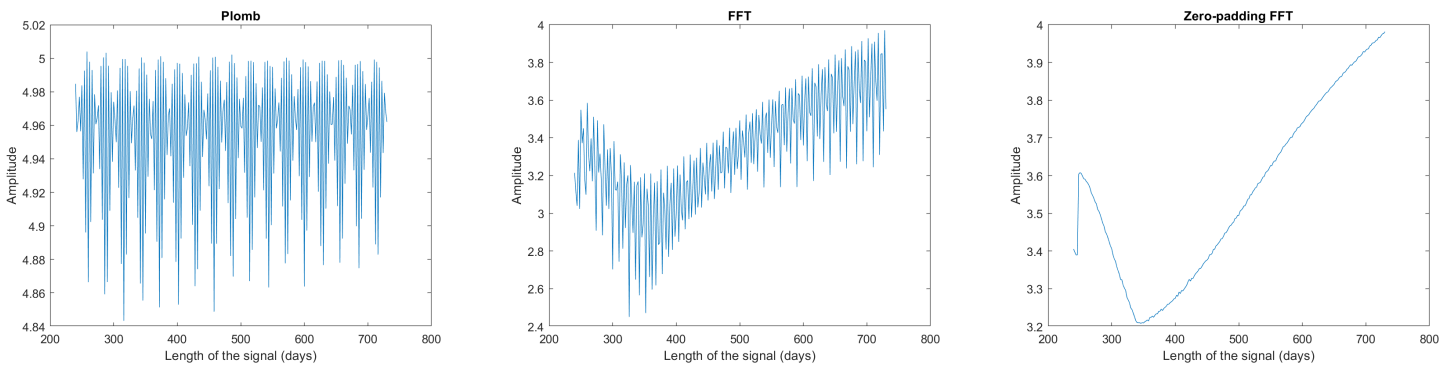


Figure 41: Detection accuracy of an amplitude of 5 in a sine signal with gaps and noise depending on the signal lengths in days using Lomb-Scargle method (plomb on the left), standard fast Fourier transform (middle), and zero-padding fast Fourier transform (right).

So far, the signal that is being tested contained frequencies that are stable or vary in period throughout the time series. However, the signals might change with time, increase or decrease in amplitude. For this kind of signal, other methods shall be used, such as the wavelet transform. In the following, a frequency that starts from day 100 and lasts for 250 days is added. The comparison is made between the wavelet transform method and the Lomb-Scargle periodogram. Table 13 shows the comparison results between the 2 methods modeling similar frequencies as the test before in addition to the new frequency with a period of 8 hours (0.3 days). The test is done over a 3-year-long signal, with 2 cases, noise-free and gap-free case (in the table NF/GF) and noise and gaps included case (in the table N/G) containing 0.4, 3.5, and 72 days data gaps and white-noise. Since the first few days of the signal fall inside the cone of influence (Figure 42), for this test, the 0.4 days gap is added at the end of the second year of the tested signal, as opposed to the previous test, where the gap was added 3 days after the start of the signal. The evolutionary period and its amplitude are detected when using the wavelet transform method with a relative accuracy of 2.4% and 2%, respectively, as compared to 0.0001% for the period and 80% for the amplitude when using the Lomb-Scargle method. Hence, the wavelet transform provides a better amplitude detection accuracy in this case. The reduced accuracy of the Lomb-Scargle method when computing the amplitude is due to the fact that the amplitude computation is dependent on the length of the time

series. Since the additional signal only lasts for about 20% of the total time length, the recovered amplitude will be 20% of the real amplitude, that is, proportional to the length of the signal.

The effect of the gaps on the results from the wavelet transform method is noticeable in Figure 42. This effect is considered the biggest disadvantage beside the computation time and resource requirement of this method. However, since the exact time of the gaps is already known in this test and in the orbit differences signal, the times of the gaps can be excluded. Therefore, the values of the amplitudes of the wavelet transform are computed by taking the mean over the time series and excluding the time points where there exist gaps and edge effects (cone of influence). Another disadvantage of the wavelet transform method is that it requires large memory to be used when dealing with signals longer than 3 years, whereas the Lomb-Scargle method can deal with 10-year-long signals, taking into account that the processing time is long. Therefore, when it comes to efficiency, the Fourier transform method is the most efficient method (1.15 seconds for a 3-year-long signal), then the Lomb-Scargle periodogram (4.15 seconds), then the wavelet transform (41.18 seconds). The Lomb-Scargle method's detection of the periods and amplitudes is very slightly influenced by the data gaps, unlike the other 2 methods. The wavelet transform can detect the non-stable periods with their amplitudes, whereas the Lomb-Scargle method may not be able to detect amplitudes of frequencies that vary in time.

In conclusion, one should carefully decide on which method to use. In the orbit analysis application, the signal might not be stable due to factors such as attitude variations, hence, the wavelet transform is the optimal method for detecting the periods and amplitudes of such a signal. Since the wavelet transform can provide results over short time series, it is suggested to use it for shorter time spans before using the Lomb-Scargle periodogram over the entire time span of the mission. This can help in understanding the behavior of the signal over the time series, then making exact conclusions from the Lomb-Scargle method.

Table 13: Comparison of the Lomb-Scargle method (Plomb) with the wavelet transform method, detecting 4 different frequencies on a 3-year-long signal.

Original		Case	Plomb		Abs. diff. Plomb		Wavelet		Abs. diff. Wavelet	
T	Amplitude		T (days)	Amplitude	dT %	dAmplitude %	T (days)	Amplitude	dT %	dAmplitude %
58.7650 days	10	NF/GF	59.2432	9.6034	0.8138	3.9663	57.6509	9.9259	1.8959	0.7408
		N/G	58.4533	9.4723	0.5304	5.2772	57.6509	9.7736	1.8959	2.2640
10 days	50	NF/GF	9.9186	49.8775	0.0298	0.2450	10.1913	49.3087	2.7808	1.3827
		N/G	9.9186	49.7755	0.0298	0.4489	10.1913	49.2630	2.7808	1.4740
0.0781 days (112.4278 mins)	5	NF/GF	0.0781	4.9784	0.0004	0.4311	0.0796	4.9656	1.9779	0.6877
		N/G	0.0781	5.0077	0.0004	0.1530	0.0796	5.0302	1.9779	0.6040
0.3333 days	30	NF/GF	0.3333	7.6060	0.0001	74.6467	0.3413	29.3823	2.4013	2.0589
		N/G	0.3333	6.0378	0.0001	79.8739	0.3413	29.6505	2.4013	1.1650

Note: N/G = the signal contains noise and gaps, NF/GF = the signal is noise-free and gap-free.

4.2 Spectral analysis

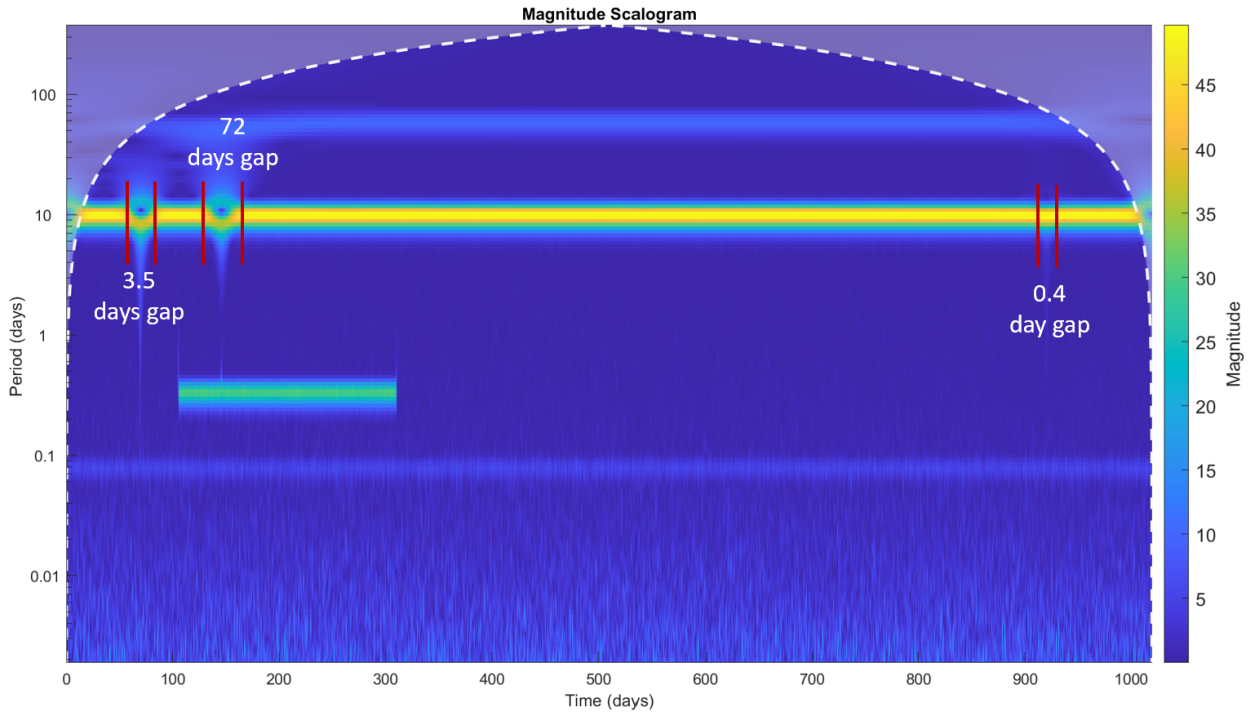


Figure 42: 3-year-long signal containing gaps and noise, with frequencies detected using wavelet transform illustrated along the time series (Note: magnitude = amplitude in this context).

5. The impact of new background models on POD

5.1. The DGFI Orbit and Geodetic Parameter Estimation Software - Orbit Computation library

The orbits at the DGFI-TUM are computed using DOGS-OC, a library in the DGFI Orbit and Geodetic Parameter Estimation Software (DOGS) which has been developed at the DGFI-TUM since 1980. DOGS is capable of processing various geodetic observation techniques and computing satellite orbits, as well as combining normal equation systems at the 3 different levels of the Gauss-Markov model, namely, the observation equation level, the normal equation level, and the parameter level (Bloßfeld, 2015). The DOGS-OC library is able to process orbits with the observation techniques DORIS and SLR. There are 4 execution modes that can be defined in the program:

MODUS = 0: numerical integration of orbits, including selected perturbing forces and recording of the position vector of the satellite (positions and velocities).

MODUS = 1: numerical integration of orbits with a simulation of the satellite's observations from stations.

MODUS = 2: numerical integration of orbits and formulating the normal equations for parameter estimations based on given observations.

MODUS = 3: numerical integration of orbits and using the least squares adjustment iteratively for fitting the orbit parameters based on given observations.

Table 14 lists the orbit parameters that are estimated within the orbit determination process, where the length of an arc is generally 3.5 days. More details on the parameters are discussed in Section 5.2.2. DOGS-OC is capable of treating non-spherical satellites, including the surface model and the satellite's attitude (orientation of the solar panels and the satellite in space). The attitude is realized based on predefined nominal models or based on quaternions that are computed using observations of star cameras (Zeitlhöfler, 2019). For the purpose of this study, the observation technique used is SLR, the execution mode, MODUS, is set to 3, and the observation-based quaternions are used for attitude realization.

5.2. Thermospheric density models

As discussed in Section 2.4.2.1, the acceleration due to drag is linearly proportional to the density (Eq. 2.17). Therefore, the accuracy of the thermospheric density models is crucial for a precise orbit. In this section, the new empirical model NRLMSIS 2.0 (Emmert et al., 2021) is compared to the older version NRLMSISE-00 (Picone et al., 2002) in terms of how accurately they fit to the SLR observations used in the orbit determination of altimetry satellites, namely, Jason-1, Jason-2, and Jason-3. The investigation is done using background models defined in the orbit determination program DOGS-OC with the only difference being the thermospheric density models used (cf. Table 15). The background models are used as in (Rudenko et al., 2023).

Table 14: Estimated orbit parameters

Parameter	Estimating period
Keplerian elements	Once per arc
Solar radiation pressure scale factor	Once per arc
Earth albedo scale factor	Once per arc
Atmospheric drag scale factor	Once per 12 hours
Empirical accelerations in the transverse and normal directions (sine and cosine)	Once per revolution
Empirical accelerations in the transverse and normal directions (polygon terms)	Once per 12 hours
SLR station range biases	Once per station per arc

First, overviews on the 2 models and on the estimated orbit parameters are given (Section 5.2.1 and Section 5.2.2), then, 2 main questions are investigated:

- 1) Since the impact of atmospheric drag is the largest in the transverse direction, does the estimation of the empirical acceleration in the transverse component increase or decrease the accuracy of the comparison? (Section 5.2.3).
- 2) Which model produces a better orbit arc RMS fit of the SLR observations? (Section 5.2.4).

5.2.1. Overview on the NRLMSISE-00 and NRLMSIS 2.0 thermospheric density models

The 2 models are part of the MSIS radar family, which aims to represent the atmospheric behavior (temperature and mass density) and the number densities of 8 species from space-based and ground-based measurements of incoherent scatter radar (ISR).

NRLMSISE-00 provides the mass densities from orbit determination due to drag and accelerometers mounted on satellites. Measurements from the Solar Maximum Mission of solar ultraviolet occultation provided molecular number density of O_2 in the middle thermosphere. In addition, new temperature measurements from the ISR, which covered the period from 1981 to 1997, were added. Lastly, the anomalous oxygen component was introduced in NRLMSISE-00, which allowed for additional mass in higher altitudes of the thermosphere. For more detailed properties, cf. Picone et al. (2002).

On the other hand, NRLMSIS 2.0 majorly focuses on lower altitudes. The oxygen density is extended with cubic splines between 50 and 85 km. New temperature measurements over the troposphere, stratosphere, and mesosphere between 2002 and 2018 were assimilated. A vital difference

is the introduction of an effective mass profile which helps in the approximation of the transition between the fully mixed region (below 70 km) and the diffusive separate region (above 200 km), where the densities of the species are coupled to the entire column, i.e. the species densities are influenced by the temperature variations through the column. Different data types were incorporated, such as infrared passive remote sensing, numerical weather prediction reanalysis, solar occultation, and ground-based observations of Light Detection and Ranging (LIDAR). Further details can be found in Emmert et al. (2021).

5.2.2. Overview on estimated orbit parameters

Besides the SLR RMS fits, the comparison is made over Jason-2 orbit parameters that were estimated within the orbit determination process and can be found in Table 14. In order to understand the correlation between each parameter, the mean of absolute values of the correlation matrices of 343 arcs (around 4 years between 2008 and 2011.8) is computed. As can be seen in Figure 43, there are 46 parameters. This number may vary depending on the number of stations observed at each arc. Firstly, there exists a very high correlation between the argument of perigee and the mean anomaly. This is due to the fact that Jason satellite's orbits are nearly circular, which does not allow a clear separation of both parameters. Secondly, there is a high correlation between the Earth's albedo scale factor and the semimajor axis since the Earth's albedo radiation affects the orbit's radial direction, i.e. can change the semimajor axis. On the other hand, there is a high correlation between the sine and cosine terms of the empirical accelerations since both terms can absorb similar mismodeled forces. Lastly, a very high correlation is between the polygon terms of atmospheric drag scale factor and the polygon terms of empirical acceleration in the along-track (transverse) direction since the force of atmospheric drag acts most in the along-track direction.

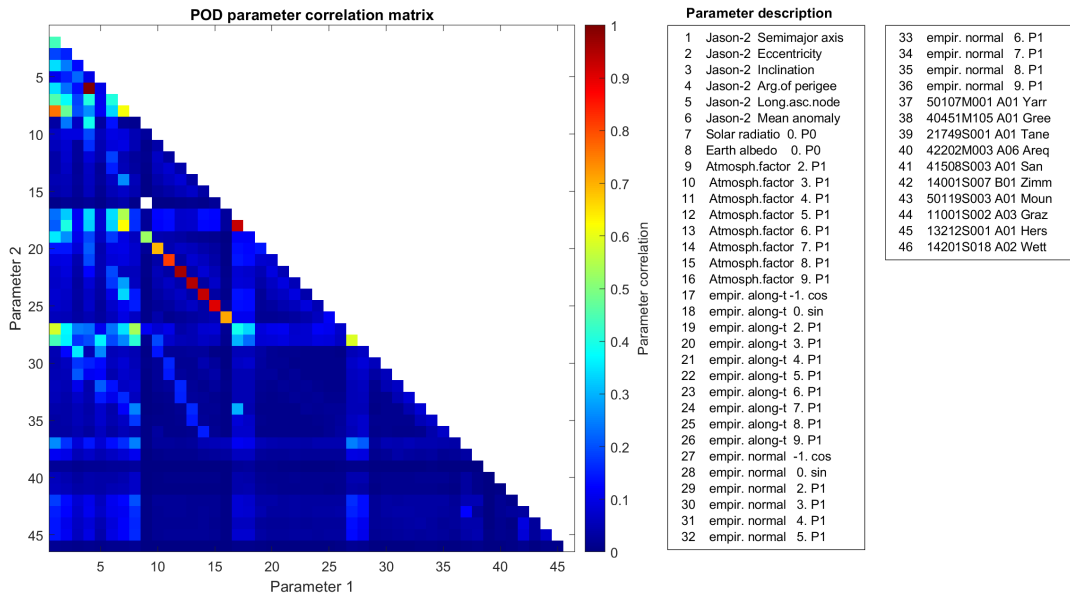


Figure 43: Mean of the absolute values of the correlation coefficients over 343 arcs.

Table 15: Force models used for POD

Force component	Model description
Earth gravity field	EIGEN-GRGS.RL04.MEAN-FIELD (Lemoine et al., 2019) Static part: up to degree/order 120 Time variable part: up to degree/order 90 Mean pole: linear mean pole convention (updated IERS 2010 Conventions; https://iers-conventions.obspm.fr/content/chapter7/icc7.pdf)
Lunar gravity field	Up to degree/order 50 (Konopliv et al., 2001)
Third body gravity effect	DE-421: Moon, Sun, Mercury, Venus, Mars, Jupiter, Saturn
Solid Earth tides	IERS Conventions 2010 (Petit and Luzum, 2010)
Permanent tide	Conventional model (IERS Conventions, 2010)
Ocean tides	EOT11a (Savcenko and Bosch, 2012) up to degree/order 30 + 62 admittance waves (Petit and Luzum, 2010)
Atmospheric tides	Biancale and Bode 2003 (Biancale and Bode, 2006)
Solid Earth pole tide	IERS Conventions, 2010
Ocean pole tide	(Desai, 2002)
Non-tidal perturbations (atmospheric, oceanic, hydrological)	Not applied
Solar radiation pressure	Constant radiation with eclipse modeling
Thermal radiation	Applied from: ftp://ftp.ids-doris.org/pub/ids/satellites/DORISSatelliteModels.pdf
Earth radiation pressure	Albedo and infrared (Knocke et al., 1988)
Atmospheric drag	NRLMSISE-00 (Picone et al., 2002) or NRLMSIS 2.0 (Emmert et al., 2021) with GFZ geomagnetic storm and solar flux indices (Matzka et al., 2021)
General relativistic correction	Schwarzschild, de Sitter, Lense-Thirring (IERS Conventions 2010)

5.2.3. Investigation on the estimation of empirical accelerations in the transverse component

Empirical accelerations are introduced to the orbit determination process to overcome uncertainties of the force models and to absorb unmodeled or mismodeled forces. In the course of this study, the effects on orbit parameters are investigated when estimating empirical accelerations in the transverse (T) direction besides atmospheric drag scale factors. By estimating the empirical acceleration in the transverse direction, the uncertainty of the models might be absorbed, and the outcome of the investigation might not be accurate. Hence, in order to avoid miscellaneous judgment, 4 Jason-2 orbits are computed over the full-time span of the mission from July 2008 to October 2019. Each of these orbits has a different parametrization in terms of the estimation of the empirical accelerations in the transverse component, and all are based on the NRLMSISE-00 thermospheric density model. As in Table 14, the empirical acceleration is divided into 2 categories, periodic and polygon terms. Therefore, one orbit includes the estimation of all the terms, a second orbit includes the estimation of the periodic terms, another orbit includes the estimation of the polygons, and the last orbit completely excludes the estimation of the empirical acceleration in the transverse component. Results of the comparison can be found in Table 16. Firstly, the percentage of observations used in the 4 cases. The comparison is possible since the 4 orbits used an almost equal number of observations (96.2%).

In Figure 44, the SLR RMS fit is significantly larger when not computing the empirical acceleration in the transverse direction compared to when estimating the polygon terms, the periodic terms and/or estimating all the terms (1.9568 cm compared to 1.6819 cm, 1.4235 cm, and 1.3499 cm, respectively). The reason is that the empirical acceleration that absorbs the mismodeled forces is excluded, and hence the differences between the dynamic orbit and observations are contained in the residuals, which are represented by the SLR RMS fit. Figures 45-49 contain plots of the estimated parameters derived with and without the estimation of empirical acceleration in the transverse direction (upper plots) and the a posteriori standard deviation of the respective parameter (Sigma value in the lower plots). Furthermore, as the most affected force when investigating the thermospheric models is the atmospheric drag, Figure 45 illustrates the scale factors of the atmospheric drag from the 4 orbits in comparison. The scale factor is a measure of how the model fits to the observations. The ideal case is when the scale factor is equal to 1. It can be seen that the mean of the scale factor when estimating the empirical acceleration in the transverse direction is closer to 1 (1.01) compared to when excluding it completely (1.28), estimating only the periodic terms (1.22), or estimating only the polygons (1.41). On the other hand, the a posteriori standard deviation of the atmospheric drag scale factor is smallest when estimating the periodic terms, i.e. the estimated parameters are better determined. A clear increase in the a posteriori standard deviation occurs when estimating polygon terms since these are highly correlated to the atmospheric drag. Other parameters, such as the Earth's albedo and the solar radiation scale factors, show a smaller standard deviation (scatter) in the case of the estimation of all terms (Figure 46 and Figure 47), whereas the a posteriori standard deviations are smaller when estimating only the polygon terms. Finally, the comparison of the empirical acceleration in the normal direction is shown in Figures 48 and 49, where the scattering is higher in the cases when not estimating the periodic terms.

As a final test, the impact on the orbit is studied. Figure 50 shows the standard deviations of orbit differences between estimating the empirical acceleration in the transverse direction (t-all-estim) and excluding it (no-t-estim), estimating only the polygon terms (t-pol-estim), and estimating only the periodic terms (t-sin-cos-estim) plotted over the whole time span of the mission. The case of excluding the T component (no-t-estim) produces a larger standard deviation of the orbit in all 3 components, where the mean of the standard deviations reaches up to 4 cm in the transverse direction. It is clear that the highest deviations are in the transverse direction since the test is conducted over this component. The values of the differences in the radial and the normal directions are close to each other, with the maximum of the mean reaching around 2 cm in the radial direction and 1.5 cm in the normal direction.

In conclusion, 1) if the goal is to assess the impact on the atmospheric drag scale factor, it is better not to estimate the polygon terms of empirical acceleration in the transverse direction and only estimate its periodic terms for 2 reasons. First, since there is a high correlation between the polygons of the atmospheric drag scale factor and the empirical acceleration in the T component, and second, since the uncertainty of the atmospheric drag scale factor is lowest when estimating only the periodic terms. 2) If the goal is to assess the impact on the solar radiation scale factor and Earth albedo scale factor, only estimating the polygon terms is suggested since there is a high correlation between the solar radiation scale factor and the periodic terms. Moreover, the uncertainty of the solar radiation scale factor and Earth albedo scale factor is the lowest when only estimating the polygon terms. Finally, if the goal is to obtain a better orbit, one should estimate all the parameters. Therefore, since the goal is to evaluate the impact of the models on the accuracy of the orbits, the comparison in the next section is based on orbits obtained with the estimation of all empirical parameters.

Table 16: Comparison of POD parameters of 4 Jason-2 orbits computed for NRLMISE-00 and estimating the empirical acceleration in the transverse direction (T) versus not estimating the polygons, not estimating the periodic terms, or not estimating both terms.

Parameter	mean					standard deviation				
	no-t-estim	t-pol-estim	t-sin-cos-estim	t-all-estim	no-t-estim	t-pol-estim	t-sin-cos-estim	t-all-estim		
Observations used (%)	96.2079	96.2051	96.2041	96.1994	-	-	-	-		
SLR RMS fit (cm)	1.9568	1.6819	1.4235	1.3499	0.8884	0.6515	0.3982	0.3656		
Mean SLR of fits (cm)	-1.6787E-08	-1.5356E-06	-2.6005E-05	-1.3331E-05	2.6695E-04	2.5719E-04	2.1920E-04	2.3130E-04		
Atmospheric drag scale factor (-)	1.2773	1.4053	1.2242	1.0075	0.9421	0.9975	0.8904	0.3538		
Solar radiation pressure scale factor (-)	1.0039	1.0053	0.9895	0.9922	0.0744	0.0663	0.0381	0.0371		
Earth albedo scale factor (-)	1.5376	1.6090	1.1513	1.2798	3.1140	2.7629	0.8314	0.6396		
Cos. term of empirical acc. in N (m/s ²)	-5.4666E-10	-3.6286E-10	-8.3788E-11	-6.5815E-11	4.1827E-09	3.9260E-09	1.7430E-09	1.5140E-09		
Sin. term of empirical acc. in N (m/s ²)	-6.0255E-10	-5.9207E-10	-7.4278E-10	-6.9024E-10	3.2250E-09	2.9647E-09	2.0250E-09	1.9220E-09		
Empirical acc. in N, polygons (m/s ²)	2.8038E-10	3.3234E-10	1.7610E-10	2.1367E-10	6.2854E-09	5.4627E-09	4.1300E-09	3.9240E-09		

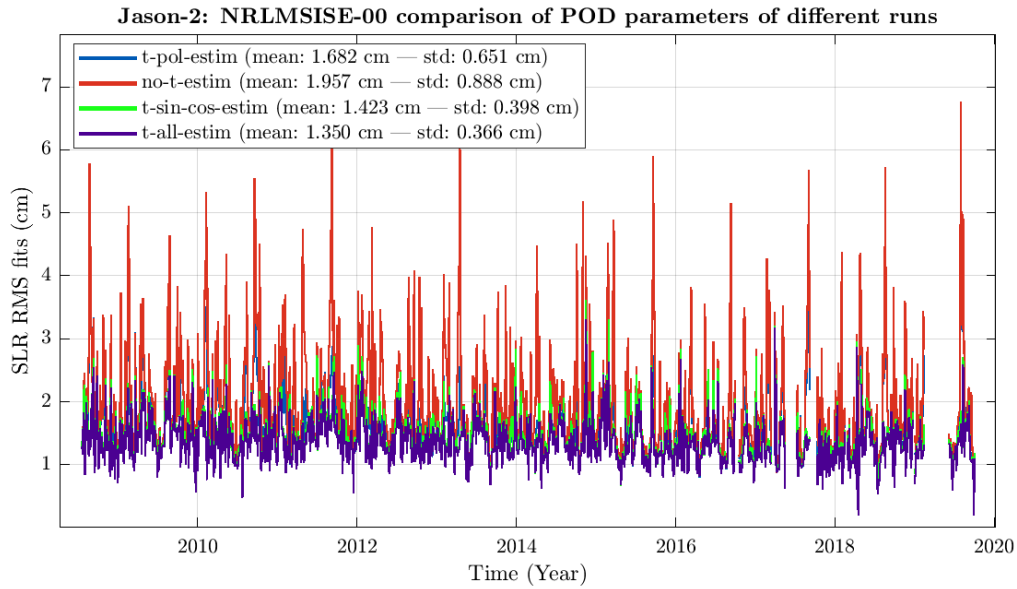


Figure 44: SLR RMS fit of Jason-2 orbit solutions computed using the models and SLR observations.

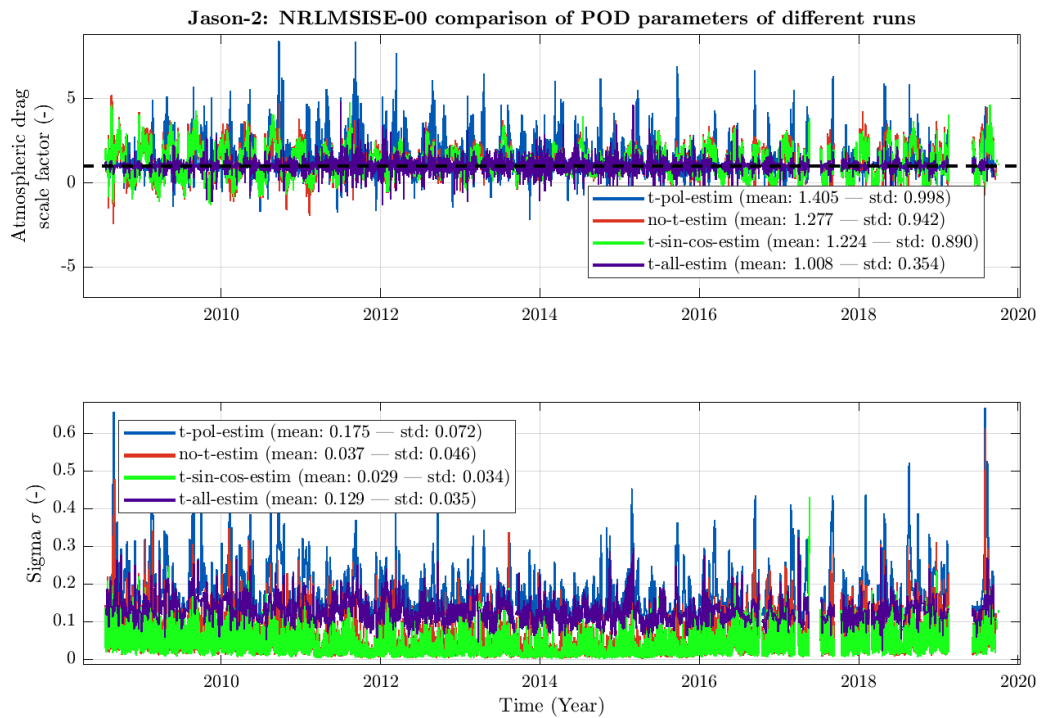


Figure 45: Atmospheric drag scale factor and its a posteriori standard deviation (Sigma) for Jason-2 orbit solutions.

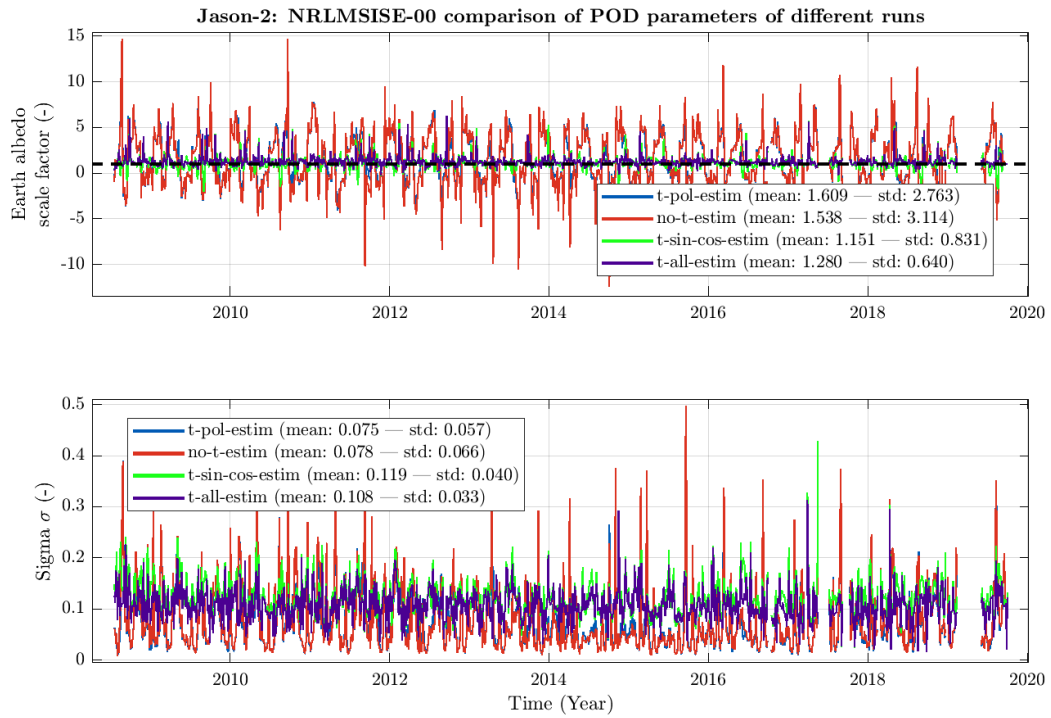


Figure 46: Earth albedo scale factor and its a posteriori standard deviation (Sigma) for Jason-2 orbit solutions.

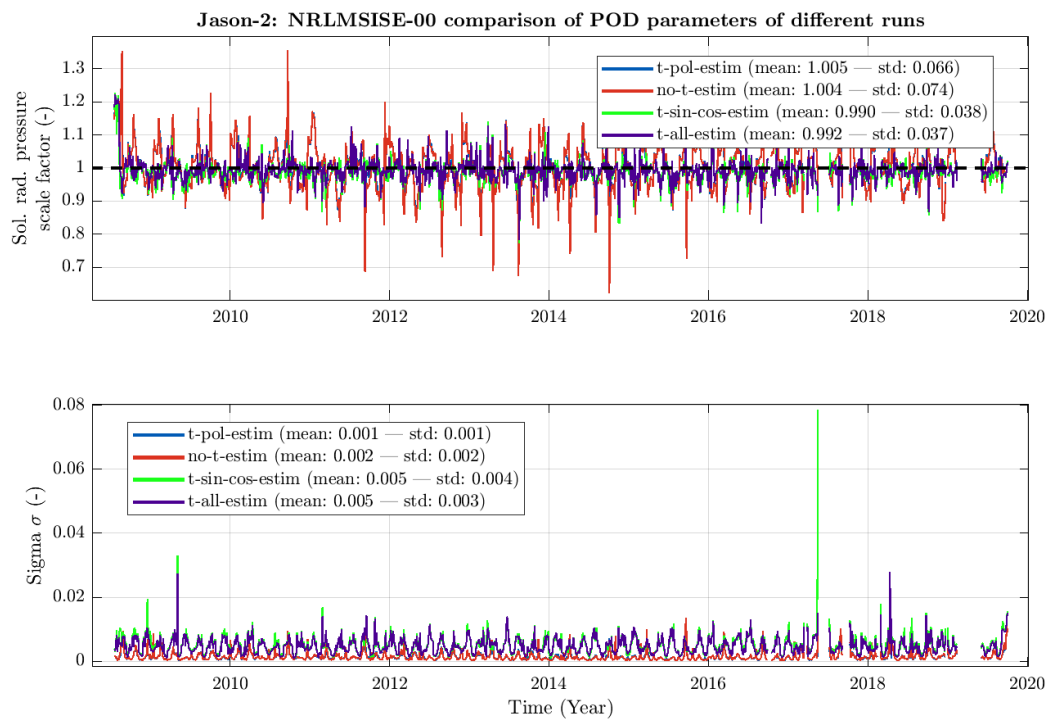


Figure 47: Solar radiation scale factor and its a posteriori standard deviation (Sigma) for Jason-2 orbit solutions.

5.2 Thermospheric density models

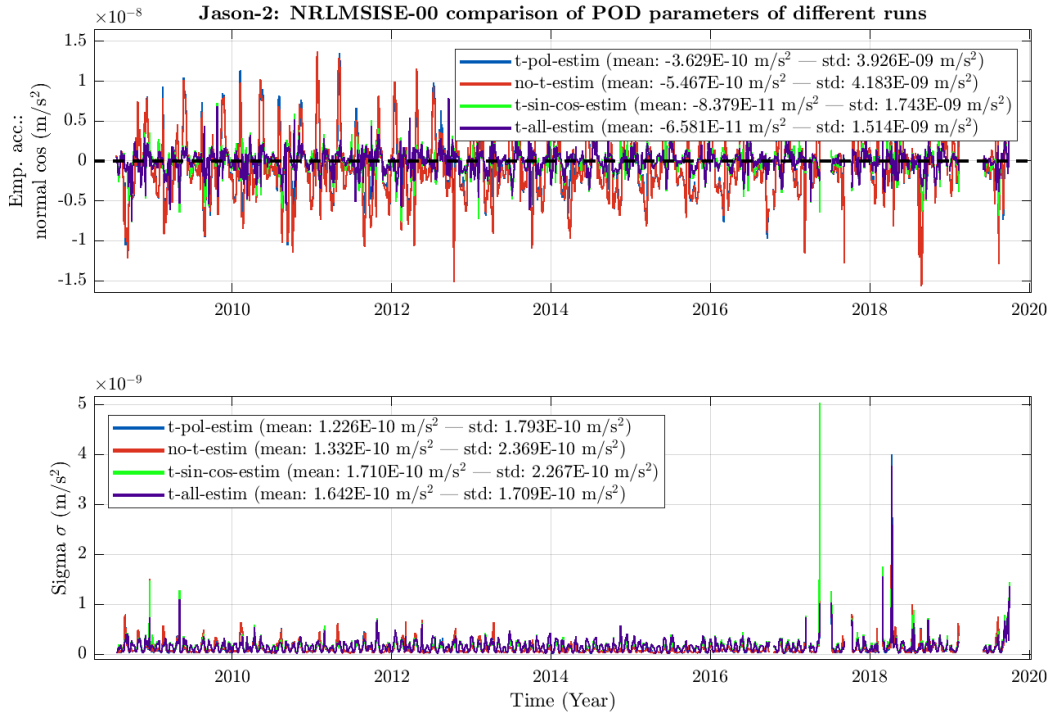


Figure 48: The amplitude of the cosine term of empirical acceleration in the normal direction and its a posteriori standard deviation (Sigma) for Jason-2 orbit solutions.

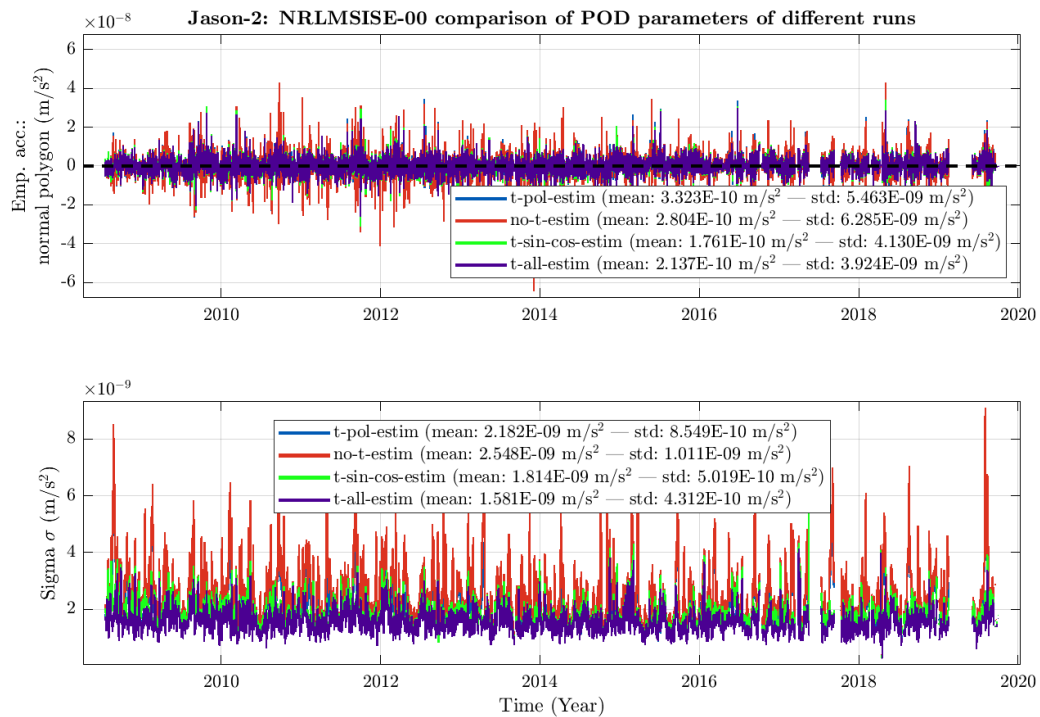


Figure 49: Empirical acceleration polygon terms in the normal direction and their a posteriori standard deviations (Sigma) for Jason-2 orbit solutions.

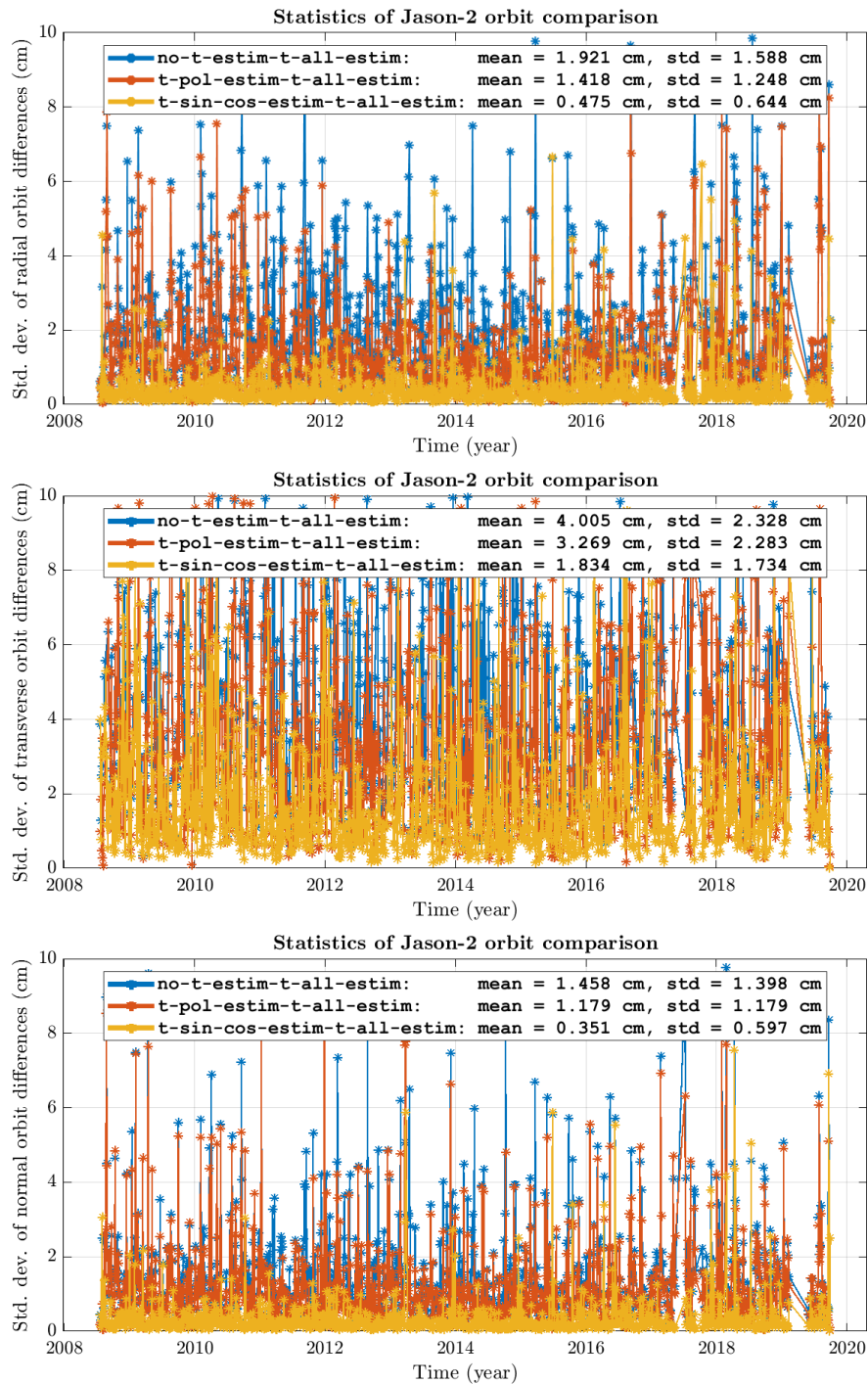


Figure 50: Standard deviations of orbit differences of the 3 cases of not estimating the transverse component against estimating it over the whole time span of the mission. (Top) The impact on the radial component, (middle) the impact on the transverse component, (bottom) the impact on the normal component.

5.2.4. Comparison of the NRLMSISE-00 and NRLMSIS 2.0 thermospheric density models

The total atmospheric densities derived using these 2 models at the positions of Jason-2 and the density differences are shown in Figure 51. In the figure, it is seen that the densities go in line with the solar activity, in other words, differences in thermospheric density are larger during the periods

of high solar activity. Furthermore, there is a 10% difference between the densities of the 2 models. In this section, the impact of this difference on altimetry satellite orbits is investigated.

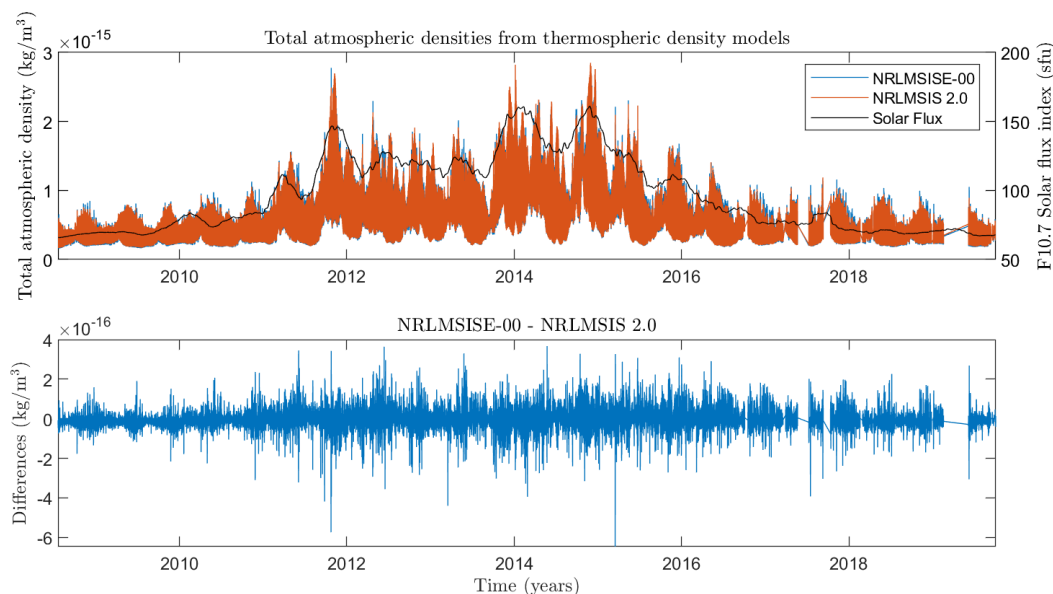


Figure 51: Atmospheric densities obtained from NRLMSISE-00 and NRLMSIS 2.0 thermospheric density models overlaid with solar flux index (top) and their differences (bottom).

For the sake of the comparison, 2 orbits are derived using similar parametrization and the same background models except for the thermospheric density models (cf. Table 15). Results of the estimated orbit parameters of TOPEX/Poseidon and the 3 Jason satellites can be found in Table 17 (TOPEX/Poseidon mission time span: from late September 1992 to October 2005), Table 18 (Jason-1 mission time span: from January 2002 to June 2013), Table 19 (Jason-2 mission time span: from July 2008 to October 2019), and Table 20 (Jason-3 mission time span: from February 2016 to October 2021). The "best" among 2 models values of the mean and standard deviation are marked bold in Tables 17-20. The results from the 2 models are very similar, the SLR RMS fit when using NRLMSISE-00 is better by 0.1% to 0.4% for the 4 satellites. The SLR RMS fit of Jason-2 can be seen in Figure 52, where the differences between the 2 models are shown in the plot on the right-hand side with a standard deviation of only 0.025 cm. Figure 53 and Figure 54 illustrate the values and their differences of the atmospheric drag scale factor and Mount Stromlo SLR station range biases, computed for Jason-2, respectively. Similarly to the SLR RMS, the values do not have a distinguishable difference. The absolute mean difference between both atmospheric drag scale factor time series is 0.006, and the difference between the 2 range bias time series is in the sub-millimeter level. Other orbit parameters, such as the solar radiation pressure scale factor, the Earth albedo scale factor, and the different terms of the empirical acceleration have comparable behavior as the atmospheric drag scale factor and the range biases.

Studying the Keplerian elements is the final step to drawing a conclusion on the 2 models. Figures 55-60 analyze the Keplerian elements computed using the 2 models. Before studying the impact of the models, it is worth looking at the behavior of the elements throughout the orbit time

span. Figure 55 shows the semimajor axis of the Jason-2 satellite. There exists a shift of the value at the end of 2017 due to an orbit maneuver performed at the end of the mission, which was done for safety reasons. The orbit after this maneuver is called the geodetic orbit¹. Another worth mentioning behavior is the linear increase in the oscillation amplitude of the inclination. This happens because of perturbations acting in the cross-track direction. An increase in the inclination means a recession of the node.

Looking back at the impact of the thermospheric density models on the Keplerian elements, the largest differences appear when there is high solar activity (in the middle of the time series). However, the magnitude of the scattering and the mean values of the differences are insignificant. Namely, the mean value of the differences in the semimajor axis is in the sub-millimeter level, and the standard deviation is 5 mm. Other Keplerian elements have very small standard deviations with the highest magnitude of 10^{-5} (degrees) in the mean anomaly and the lowest of 10^{-10} (-) in the eccentricity. In addition, the differences in the orbits computed using the 2 models produce a mean of standard deviation between 0.5 mm and 1 mm in the radial direction of the 4 satellites.

In general, all orbit parameters from the 2 models show relatively similar differences. This might be explained by the fact that the satellites are orbiting at an altitude around 1300 km and the NRLMSIS 2.0 model is extensively focused for lower altitudes (Emmert et al., 2021), which means that the 10% difference between the 2 atmospheric densities in Figure 51 does not significantly impact the orbit parameters. As a conclusion, both models can be used for POD of altimetry satellites and produce similar accuracy.

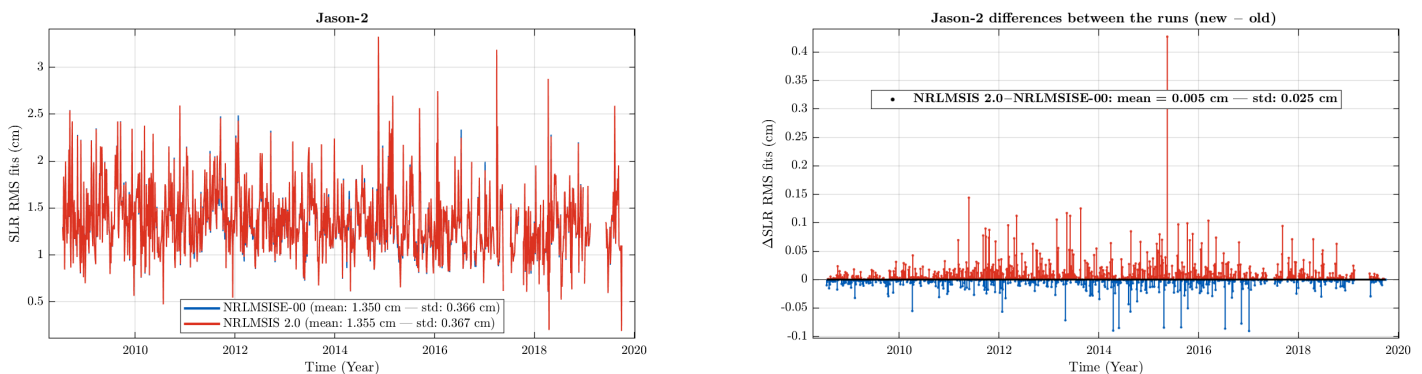


Figure 52: SLR RMS fit of Jason-2 orbits (left) and their differences (right) derived using the NRLMSISE-00 and NRLMSIS 2.0 thermospheric density models.

¹ <https://www.eoportal.org/satellite-missions/jason-2mission-status>

Table 17: Comparison of POD parameters of 2 TOPEX/Poseidon orbits computed for NRLMSISE-00 versus NRLMSIS 2.0.

Parameter	mean		standard deviation	
	NRLMSISE-00	NRLMSIS 2.0	NRLMSISE-00	NRLMSIS 2.0
Observations used (%)	95.0511	95.0514	–	–
Mission SLR RMS fits (cm)	2.5642	2.5688	0.9601	0.9595
Mission mean of SLR fits (cm)	-4.1385E-06	-1.3922E-06	2.2044E-04	2.2567E-04
Atmospheric drag scale factor (-)	1.0076	1.0002	0.4859	0.4899
Solar radiation pressure scale factor (-)	0.9773	0.9769	0.0877	0.0879
Earth's albedo scale factor (-)	0.8857	0.8871	0.5766	0.5710
Cos. term of empirical acc. in N (m/s^2)	-3.2246E-11	-2.9521E-11	1.0369E-09	1.0419E-09
Sin. term of empirical acc. in N (m/s^2)	-9.0429E-10	-9.0311E-10	1.9507E-09	1.9513E-09
Empirical acc. in N, polygon terms (m/s^2)	-4.5519E-10	-4.4274E-10	6.2282E-09	6.2366E-09
Cos. term of empirical acc. in T (m/s^2)	2.1710E-10	2.1332E-10	1.7960E-09	1.8047E-09
Sin. term of empirical acc. in T (m/s^2)	-8.7183E-11	-9.0488E-11	4.5590E-09	4.5823E-09
Empirical acc. in T, polygon terms (m/s^2)	1.9482E-11	8.9765E-12	7.6461E-10	7.7643E-10

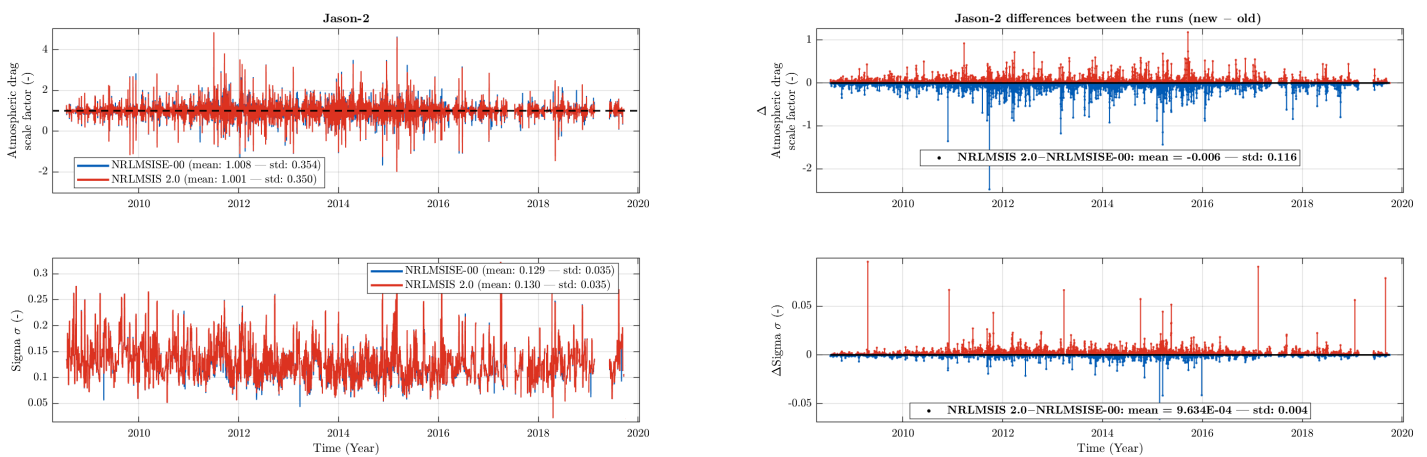


Figure 53: Atmospheric drag scale factor and its a posteriori standard deviation (Sigma) for Jason-2 orbits (left) and their differences (right) derived using the NRLMSISE-00 and NRLMSIS 2.0 thermospheric density models.

Table 18: Comparison of POD parameters of 2 Jason-1 orbits computed for NRLMSISE-00 versus NRLMSIS 2.0.

Parameter	mean		standard deviation	
	NRLMSISE-00	NRLMSIS 2.0	NRLMSISE-00	NRLMSIS 2.0
Observations used (%)	95.2028	95.2031	–	–
Mission SLR RMS fits (cm)	1.3626	1.3686	0.4102	0.41396
Mission mean of SLR fits (cm)	2.2337-05	2.6498E-05	7.3903E-04	7.3759E-04
Atmospheric drag scale factor (-)	0.9892	0.9874	0.4284	0.4250
Solar radiation pressure scale factor (-)	0.9491	0.9489	0.0462	0.04635
Earth's albedo scale factor (-)	1.0268	1.0224	0.7192	0.7230
Cos. term of empirical acc. in N (m/s^2)	-2.9305E-11	-3.5960E-11	1.4870E-09	1.4957E-09
Sin. term of empirical acc. in N (m/s^2)	-5.5079E-10	-5.5383E-10	1.8734E-09	1.8761E-09
Empirical acc. in N, polygon terms (m/s^2)	8.6640E-11	8.6586E-11	3.8605E-09	3.8722E-09
Cos. term of empirical acc. in T (m/s^2)	-6.0396E-11	-6.6057E-11	1.9254E-09	1.9363E-09
Sin. term of empirical acc. in T (m/s^2)	2.8737E-10	3.1821E-10	5.9009E-09	5.9089E-09
Empirical acc. in T, polygon terms (m/s^2)	-7.6297E-12	-1.4254E-11	7.4038E-10	7.6566E-10

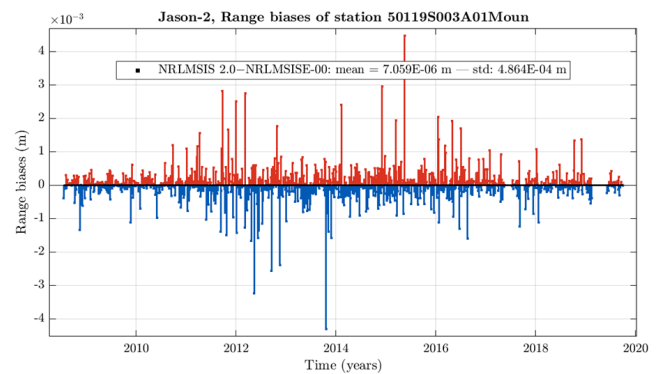
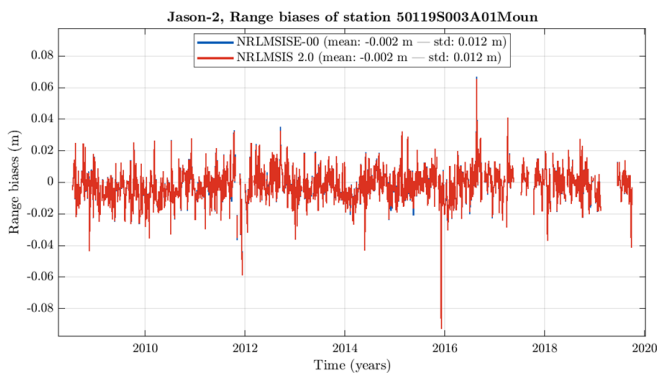


Figure 54: Mount Stromlo SLR station range biases (left) and their differences (right) derived for Jason-2 orbits using the NRLMSISE-00 and NRLMSIS 2.0 thermospheric density models.

Table 19: Comparison of POD parameters of 2 Jason-2 orbit solutions computed for NRLMSISE-00 versus NRLMSIS 2.0.

Parameter	mean		standard deviation	
	NRLMSISE-00	NRLMSIS 2.0	NRLMSISE-00	NRLMSIS 2.0
Observations used (%)	96.1994	96.1995	–	–
Mission SLR RMS fits (cm)	1.3499	1.3554	0.3656	0.3667
Mission mean of SLR fits (cm)	-1.3331E-05	-6.1957E-06	2.3135E-04	2.3374E-04
Atmospheric drag scale factor (-)	1.0075	1.0012	0.3538	0.3502
Solar radiation pressure scale factor (-)	0.9922	0.9924	0.0371	0.0371
Earth's albedo scale factor (-)	1.2798	1.2790	0.6396	0.6383
Cos. term of empirical acc. in N (m/s^2)	-6.5815E-11	-6.9301E-11	1.5138E-09	1.5117E-09
Sin. term of empirical acc. in N (m/s^2)	-6.9024E-10	-6.9026E-10	1.9222E-09	1.9214E-09
Empirical acc. in N, polygon terms (m/s^2)	2.1367E-10	2.1113E-10	3.9234E-09	3.9284E-09
Cos. term of empirical acc. in T (m/s^2)	-3.2901E-11	-3.0983E-11	1.6472E-09	1.6489E-09
Sin. term of empirical acc. in T (m/s^2)	-3.0346E-10	-3.1296E-10	3.8672E-09	3.8628E-09
Empirical acc. in T, polygon terms (m/s^2)	-1.0575E-10	-1.0775E-10	5.6914E-10	5.7190E-10

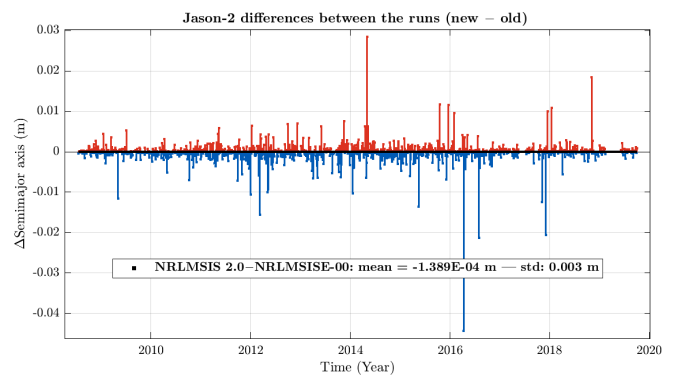
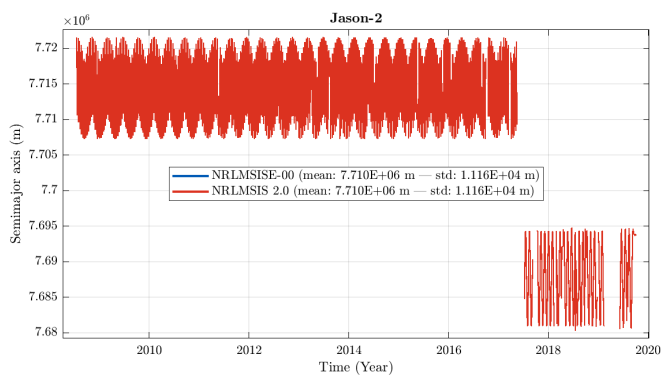


Figure 55: Semimajor axis of Jason-2 orbits computed using the NRLMSISE-00 and NRLMSIS 2.0 thermospheric density models (left) and their differences (right).

Table 20: Comparison of POD parameters of the 2 Jason-3 orbit solutions computed for NRLMSISE-00 versus NRLMSIS 2.0.

Parameter	mean		standard deviation	
	NRLMSISE-00	NRLMSIS 2.0	NRLMSISE-00	NRLMSIS 2.0
Observations used (%)	98.8388	98.8387	—	—
Mission SLR RMS fits (cm)	1.3838	1.3857	0.4041	0.4031
Mission mean of SLR fits (cm)	-5.1935E-05	-4.2911E-05	1.8646E-04	1.8682E-04
Atmospheric drag scale factor (-)	1.0001	1.0018	0.2704	0.2655
Solar radiation pressure scale factor (-)	0.9885	0.9885	0.0274	0.0274
Earth's albedo scale factor (-)	1.3026	1.3028	0.5755	0.5769
Cos. term of empirical acc. in N (m/s^2)	-1.6744E-11	-1.9200E-11	1.3469E-09	1.3457E-09
Sin. term of empirical acc. in N (m/s^2)	-6.2628E-10	-6.2652E-10	1.7663E-09	1.7651E-09
Empirical acc. in N, polygon terms (m/s^2)	4.6412E-10	4.6662E-10	4.0235E-09	4.0256E-09
Cos. term of empirical acc. in T (m/s^2)	1.3318E-10	1.3364E-10	1.3245E-09	1.3285E-09
Sin. term of empirical acc. in T (m/s^2)	-1.4244E-12	8.4487E-12	3.1785E-09	3.1792E-09
Empirical acc. in T, polygon terms (m/s^2)	-8.7121E-11	-8.0827E-11	4.2512E-10	4.2439E-10

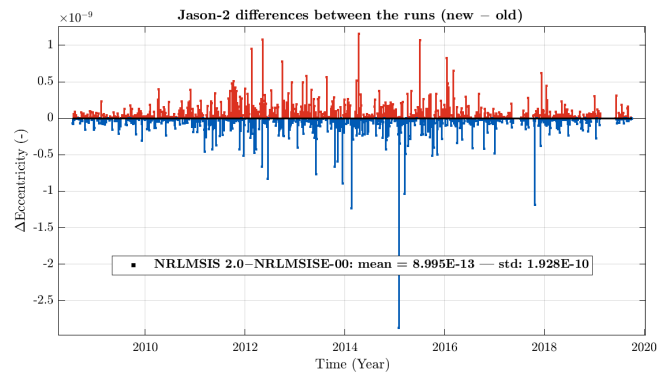
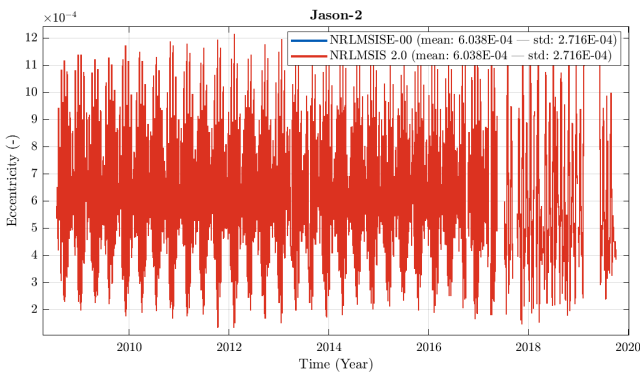


Figure 56: Eccentricity of Jason-2 orbits computed using the NRLMSISE-00 and NRLMSIS 2.0 thermospheric density models (left) and their differences (right).

5.2 Thermospheric density models

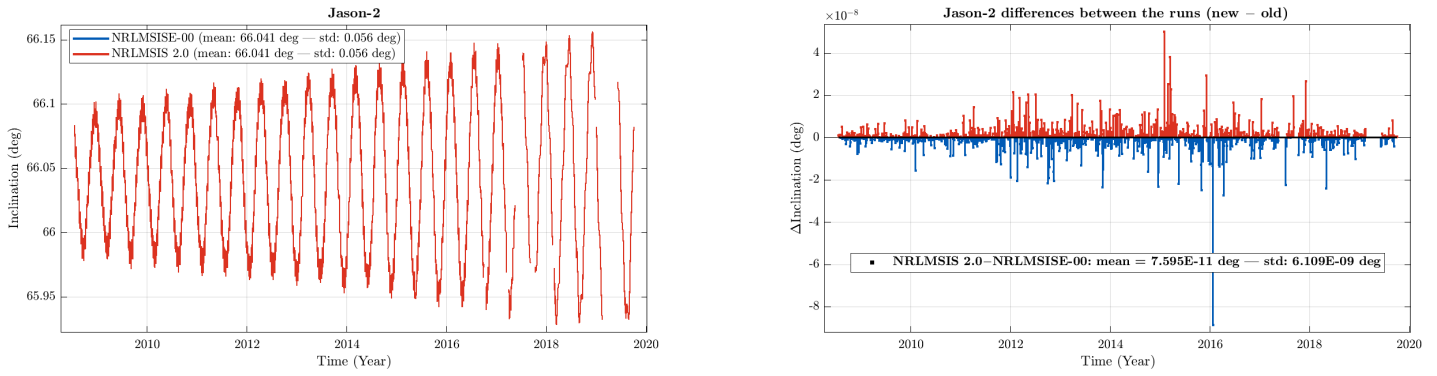


Figure 57: Inclination of Jason-2 orbits computed using the NRLMSISE-00 and NRLMSIS 2.0 thermospheric density models (left) and their differences (right).

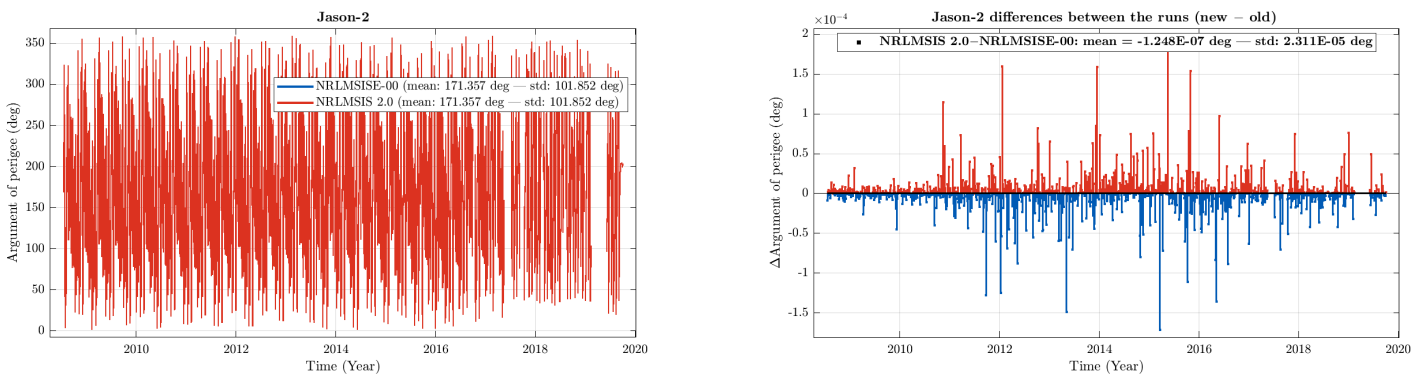


Figure 58: Argument of perigee of Jason-2 orbits computed using the NRLMSISE-00 and NRLMSIS 2.0 thermospheric density models (left) and their differences (right).

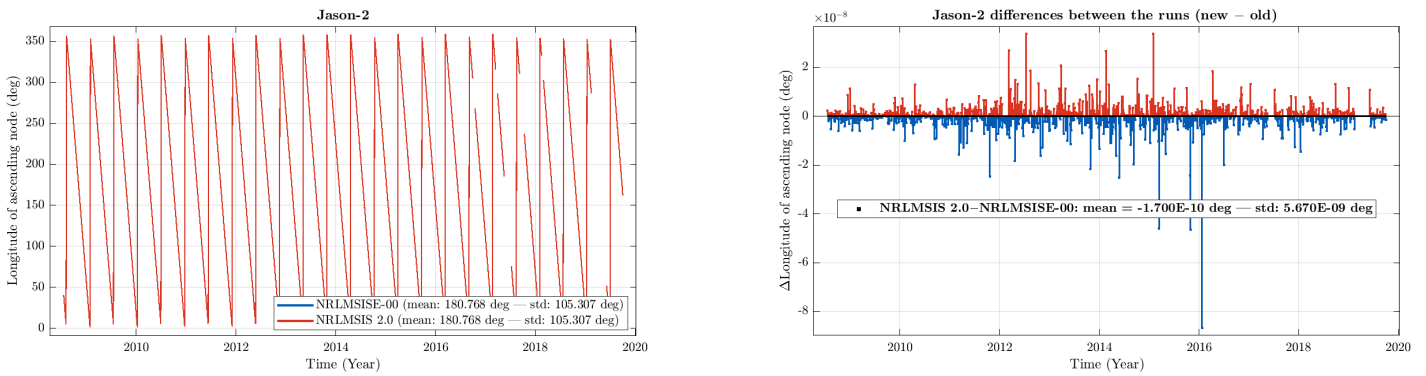


Figure 59: Longitude of ascending node of Jason-2 orbits computed using the NRLMSISE-00 and NRLMSIS 2.0 thermospheric density models (left) and their differences (right).

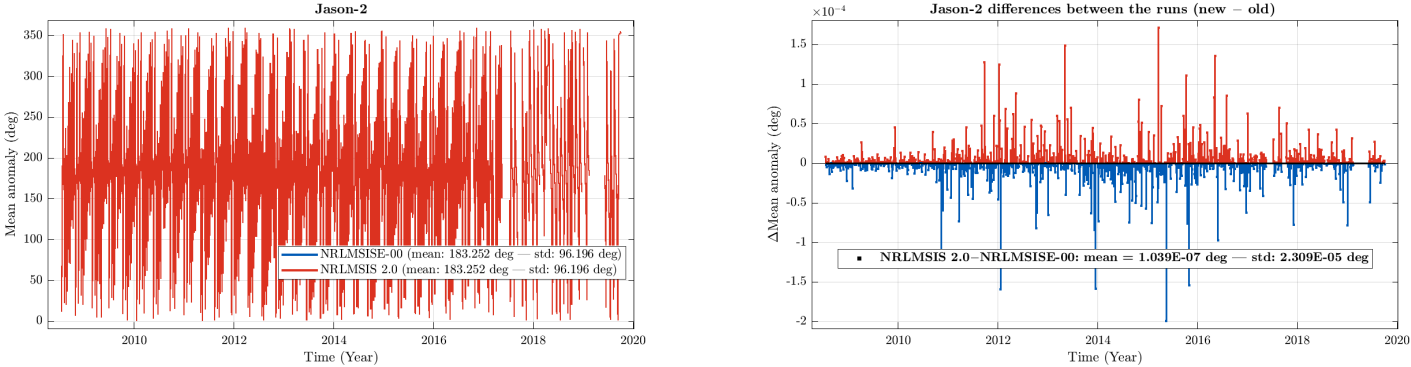


Figure 60: Mean anomaly of Jason-2 orbits computed using the NRLMSISE-00 and NRLMSIS 2.0 thermospheric density models (left) and their differences (right).

5.3. Earth's gravity field models

The relationship between the acceleration of the satellite and Earth's gravity field is described in Eq. 2.9 in Section 2.4.1.1. The perturbations due to the gravitational force and Earth's oblateness (spherical harmonic degree 2) are the major sources acting on LEO satellites. Higher degree and order coefficients also play an important role in precise orbit determination. Developments in estimating the spherical harmonic coefficients and deriving Earth's gravity field models have been in progress in the recent decades. In the previous section and as in Rudenko et al. (2023), the EIGEN-GRGS.RL04.MEAN-FIELD model developed by Lemoine et al. (2018) has been used. Recently, a new release of the model has been developed at CNES named CNES_GRGS.RL05MF_combined_GRACE_SLR_DORIS (Lemoine et al., 2023).

In this section, the new Earth's gravity field model CNES_GRGS.RL05MF_combined_GRACE_SLR_DORIS is tested as compared to the older version EIGEN-GRGS.RL04.MEAN-FIELD (will be called RL05 and RL04 henceforward, respectively) in terms of how accurate the orbits of altimetry satellites derived by implementing those models fit the SLR observations. A similar procedure is used as in the previous section. We use the same background models defined in Table 15, with the thermospheric model NRLMSISE-00. First, an overview of the 2 models is given, then, an investigation on the differences between the 2 models and their impact on the orbits of altimetry satellites is done.

5.3.1. Overview on the EIGEN-GRGS.RL04.MEAN-FIELD and CNES_GRGS.RL05MF_combined_GRACE_SLR_DORIS gravity field models

The 2 models were derived at CNES based on satellite-only observations, namely, from GRACE, GOCE, and SLR and DORIS satellites. Both models contain time-variable and static parts, the time-variable part is up to degree and order 90, and the static part is for the degree and order from 90 until 300. In this investigation, the models are taken up to degree and order 120, and the degree 1 terms (representing the center of the Earth) are set to 0 (in the geocenter). The time variable gravity field part is a mean model from monthly GRACE data, composed of a bias, a linear drift, and semi-annual and annual components that were modeled for each year between late 2002 and mid-2016 for RL04 (Lemoine et al., 2018), and between April 2002 and October 2021 for RL05 (Lemoine et al., 2023). The static part is based on GOCE-derived GOCE-DIR5 gravity model (Bruinsma et al., 2013). The treatment of the period before and after the GRACE era differs for each model. For RL04, the data was extrapolated using SLR observations from 1985 until 2002 for the low degree and order coefficients (degree 2) before 2002. For estimating other degree components before or after GRACE period, the periodic terms are based on extrapolation of 14 years GRACE data of monthly global fits coefficients. On the other hand, RL05 makes use of "super mascons", the spatial representation of the gravity field using SLR+DORIS observations. The extrapolation beyond 2022 is based on 20 years of GRACE and GRACE-FO (GRACE Follow On) data. The SLR as well as the DORIS observations were introduced from 1993 to 2023, including observations from LAGEOS-1 and LAGEOS-2, STARLETTE, Ajisai, Stella, and Lares SLR satellites, and all DORIS missions¹ except for Cryosat-2 due to an oscillation at 482 days (Lemoine et al., 2023). In addition

¹ <https://ids-doris.org/doris-system/satellites.html>

to GRACE-FO and DORIS data, new ocean tide, and atmospheric pressure dealiasing models are implemented in RL05¹. Other differences, such as making use of the latest version of accelerometer measurements, orbits, and clock corrections of GPS satellites, were used from the International GNSS Service (IGS) instead of orbit products from GRGS, in addition to the implementation of data loss minimization strategy in case of data gaps. Furthermore, in RL04, only the monthly solution of the GRACE data was used, whereas, in RL05, the monthly and 10-day solutions were added². In the following, a detailed analysis of orbit parameters is performed, similar to the analysis of the thermospheric density models.

5.3.2. Comparison of orbit parameters obtained using EIGEN-GRGS.RL04.MEAN-FIELD and CNES_GRGS.RL05MF_combined_GRACE_SLR_DORIS gravity field models

As in the case of Section 5.2.4, the same orbit parametrization and background models are used to compute 2 orbits solutions, one with the RL04 and the other with the RL05 model. The 4 satellite orbits, TOPEX/Poseidon, and the 3 Jason missions covering a time span from 1992 to 2021 are processed. The results of the orbit parameters by the 2 models are listed in Table 21 for TOPEX/Poseidon, Table 22 for Jason-1, Table 23 for Jason-2, and Table 24 for Jason-3. The "best" values of the mean and standard deviation among the 2 models are marked in bold in Tables 21-24/. The results in Tables 21, 22, and 23 are comparable, with $\pm 0.2\%$ differences in the SLR RMS fit. For the case of Jason-3, the SLR RMS fit is 2% better (lower) with the RL05 model (1.35 cm) as compared to the RL04 model (1.38 cm). The mean of SLR fits in all 4 cases has relatively small values (around 10^{-5} cm) since the SLR station range biases are estimated. Other parameters, namely, the atmospheric drag scale factor, the solar radiation pressure scale factor, the Earth albedo scale factor, and empirical accelerations in the transverse and the normal components, all show quite similar results. Therefore, only the figures of relevant differences are presented.

Figures 61, 62, 63, and 64 show the arc-wise SLR RMS fits and their differences of the 2 orbits of TOPEX/Poseidon, Jason-1, Jason-2, and Jason-3, respectively, computed with the RL04 and RL05 models. In Figure 61, the differences on the right-hand side show an improvement (in blue) for TOPEX/Poseidon in the period between 1992 and 1998 with the RL05 model, besides a slightly increased scatter between 2002 and 2004 that is also seen in Figure 62 for Jason-1. Furthermore, an enhanced behavior with the RL05 model is observed around 2012 for Jason-1 (Figure 62) and Jason-2 (Figure 63). Along the Jason-2 time span, the RL05 model shows an enhancement (in blue) in SLR RMS fits except for the period between 2016.5 and 2018.5, the period where there was a gap between GRACE and GRACE-FO data. The same behavior is observed for Jason-3 in Figure 64, where the improvement is over the mission time span except for the period 2016.5-2018.5. Another worth-noting behavior is distinguished in the sine term of the empirical acceleration in the normal direction of TOPEX/Poseidon and Jason-1 satellite orbits. In Figure 65, the amplitude of the mean value when using the RL05 model is lower than the mean value computed when using the RL04 model. In contrast, the standard deviation with the RL05 model is slightly greater than

¹ <https://grace.obs-mip.fr/variable-models-grace-lageos/introduction-grace-solutions/>

² https://grace.obs-mip.fr/variable-models-grace-lageos/grace-solutions-release-05/rl05-products-description/GRACE_data

with the RL04 model since the scatter in the periods 1992.0-1998.0 and 2002.0-2004.0 is larger.

Table 21: Comparison of POD parameters of 2 TOPEX/Poseidon orbit solutions computed using EIGEN-GRGS.RL04 vs CNES_GRGS.RL05

Parameter	mean		standard deviation	
	RL04	RL05	RL04	RL05
Observations used (%)	95.0511	95.0505	–	–
Mission SLR RMS fits (cm)	2.5642	2.5595	0.9601	0.9580
Mission mean of SLR fits (cm)	-4.1385E-06	5.3885E-07	0.0002	0.0002
Atmospheric drag scale factor (-)	1.0076	1.0099	0.4859	0.4848
Solar radiation pressure scale factor (-)	0.9773	0.9768	0.0877	0.0877
Earth's albedo scale factor (-)	0.8857	0.8897	0.5766	0.5749
Cos. term of empirical acc. in N (m/s^2)	-3.2246E-11	-4.0663E-11	1.0369E-09	1.0348E-09
Sin. term of empirical acc. in N (m/s^2)	-9.0429E-10	-2.3766E-10	1.9507E-09	2.0513E-09
Empirical acc. in N, polygon terms (m/s^2)	-4.5519E-10	-6.3331E-10	6.2282E-09	6.2298E-09
Cos. term of empirical acc. in T (m/s^2)	2.1710E-10	1.6361E-10	1.7960E-09	1.8134E-09
Sin. term of empirical acc. in T (m/s^2)	-8.7183E-11	-1.86012E-10	4.5590E-09	4.5882E-09
Empirical acc. in T, polygon terms (m/s^2)	1.9482E-11	2.1985E-11	7.6461E-10	7.6227E-10

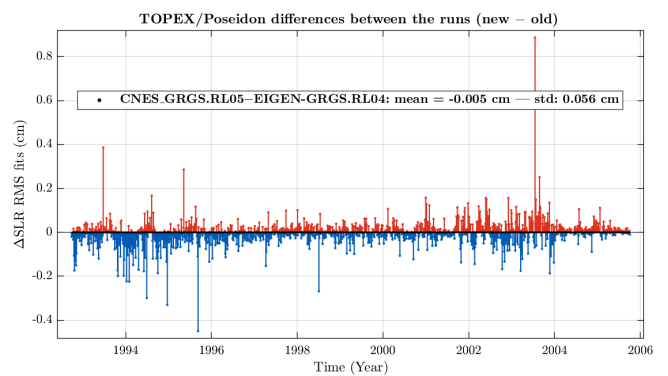
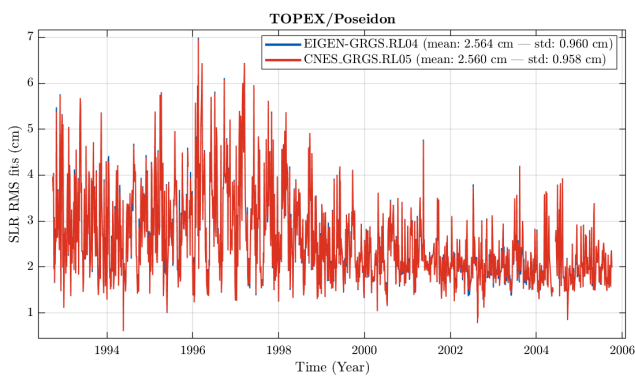


Figure 61: SLR RMS fits of TOPEX/Poseidon orbits (left) and their differences (right) derived using the EIGEN-GRGS.RL04 and CNES_GRGS.RL05 gravity field models.

Table 22: Comparison of POD parameters of 2 Jason-1 orbit solutions computed using EIGEN-GRGS.RL04 vs CNES_GRGS.RL05

Parameter	mean		standard deviation	
	RL04	RL05	RL04	RL05
Observations used (%)	95.1382	95.1391	–	–
SLR RMS fit (cm)	1.3626	1.3654	0.4102	0.4093
Mission mean of SLR fits (cm)	2.3369E-05	2.3296E-05	0.0007	0.0007
Atmospheric drag scale factor (-)	0.9892	0.9899	0.4284	0.4285
Solar radiation pressure scale factor (-)	0.9491	0.9490	0.0462	0.0462
Earth's albedo scale factor (-)	1.0268	1.0304	0.7192	0.7144
Cos. term of empirical acc. in N (m/s^2)	-2.9305E-11	-2.9943E-11	1.4870E-09	1.4756E-09
Sin. term of empirical acc. in N (m/s^2)	-5.5079E-10	-3.2216E-10	1.8734E-09	1.9641E-09
Empirical acc. in N, polygon terms (m/s^2)	8.6640E-11	5.8940E-11	3.8605E-09	3.8602E-09
Cos. term of empirical acc. in T (m/s^2)	-6.0396E-11	-1.0133E-10	1.9254E-09	1.9340E-09
Sin. term of empirical acc. in T (m/s^2)	2.8737E-10	3.0072E-10	5.9009E-09	5.9159E-09
Empirical acc. in T, polygon terms (m/s^2)	-7.6297E-12	-6.9075E-12	7.4038E-10	7.3494E-10

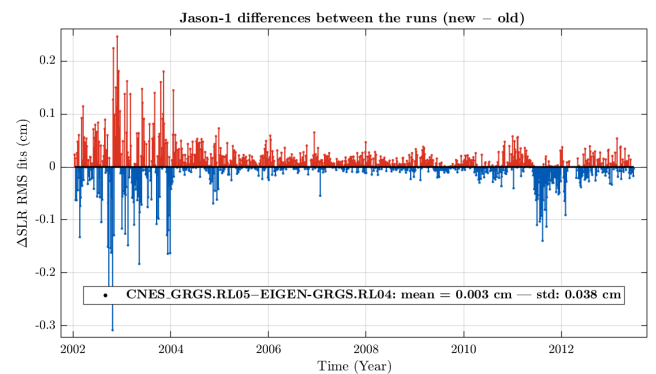
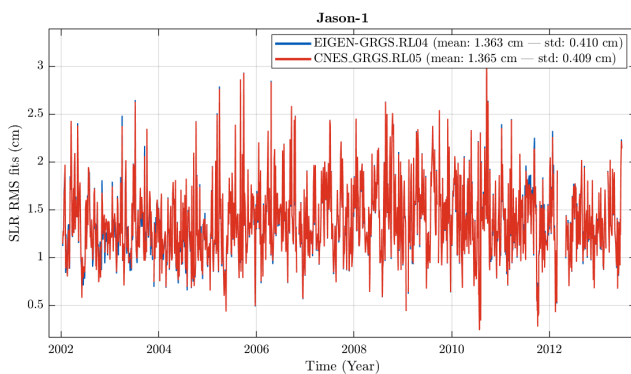


Figure 62: SLR RMS fits of Jason-1 orbits (left) and their differences (right) derived using the EIGEN-GRGS.RL04 and CNES_GRGS.RL05 gravity field models.

Table 23: Comparison of POD parameters of 2 Jason-2 orbit solutions computed using EIGEN-GRGS.RL04 vs CNES_GRGS.RL05

Parameter	mean		standard deviation	
	RL04	RL05	RL04	RL05
Observations used (%)	96.1994	96.19941	–	–
Mission SLR RMS fits (cm)	1.3499	1.3477	0.3656	0.3637
Mission mean of SLR fits (cm)	-1.3331E-05	-6.6641E-06	0.0002	0.0002
Atmospheric drag scale factor (-)	1.0075	1.0063	0.3538	0.3524
Solar radiation pressure scale factor (-)	0.9922	0.9922	0.0371	0.0372
Earth's albedo scale factor (-)	1.2798	1.2888	0.6396	0.6407
Cos. term of empirical acc. in N (m/s^2)	-6.5815E-11	-6.5819E-11	1.5138E-09	1.5094E-09
Sin. term of empirical acc. in N (m/s^2)	-6.9024E-10	-6.9741E-10	1.9222E-09	1.9327E-09
Empirical acc. in N, polygon terms (m/s^2)	2.1367E-10	8.1761E-11	3.9239E-09	3.9192E-09
Cos. term of empirical acc. in T (m/s^2)	-3.2901E-11	-2.7951E-11	1.6472E-09	1.6583E-09
Sin. term of empirical acc. in T (m/s^2)	3.0346E-10	3.2551E-10	3.8671E-09	3.9060E-09
Empirical acc. in T, polygon terms (m/s^2)	-1.0575E-10	-1.0716E-10	5.6914E-10	5.6885E-10

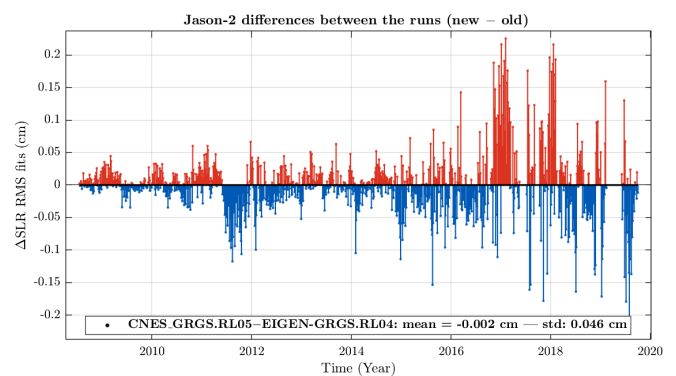
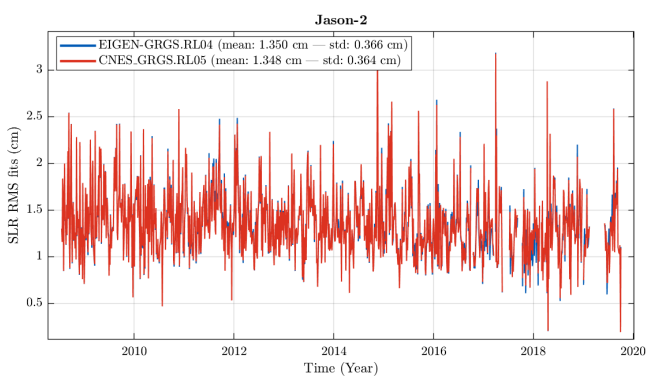


Figure 63: SLR RMS fits of Jason-2 orbits (left) and their differences (right) derived using the EIGEN-GRGS.RL04 and CNES_GRGS.RL05 gravity field models.

Table 24: Comparison of POD parameters of 2 Jason-3 orbit solutions computed using EIGEN-GRGS.RL04 vs CNES_GRGS.RL05

Parameter	mean		standard deviation	
	RL04	RL05	RL04	RL05
Observations used (%)	98.8388	98.8358	–	–
Mission SLR RMS fits (cm)	1.3838	1.3541	0.4041	0.4051
Mission mean of SLR fits (cm)	-5.1935E-05	-3.6179E-05	0.0002	0.0002
Atmospheric drag scale factor (-)	1.0001	0.9925	0.2704	0.2701
Solar radiation pressure scale factor (-)	0.9885	0.9892	0.0274	0.0263
Earth's albedo scale factor (-)	1.3026	1.3505	0.5755	0.5608
Cos. term of empirical acc. in N (m/s^2)	-1.6744E-11	-3.3681E-11	1.3469E-09	1.3103E-09
Sin. term of empirical acc. in N (m/s^2)	-6.2628E-10	-5.4413E-10	1.7663E-09	1.7624E-09
Empirical acc. in N, polygon terms (m/s^2)	4.6412E-10	1.2642E-10	4.0235E-09	3.9931E-09
Cos. term of empirical acc. in T (m/s^2)	1.3318E-10	1.0417E-10	1.3245E-09	1.2746E-09
Sin. term of empirical acc. in T (m/s^2)	-1.4244E-12	3.4939E-11	3.1785E-09	3.0494E-09
Empirical acc. in T, polygon terms (m/s^2)	-8.7121E-11	-9.1348E-11	4.2512E-10	4.0733E-10

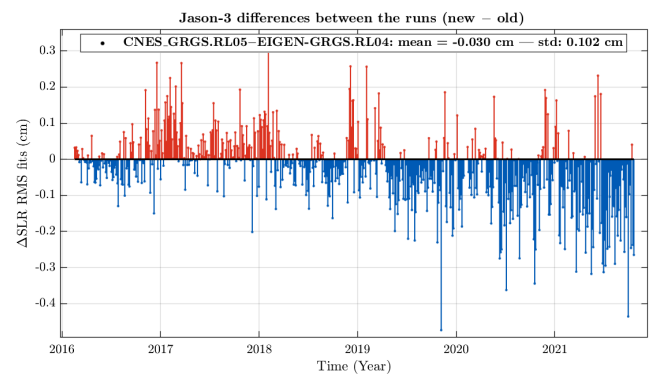
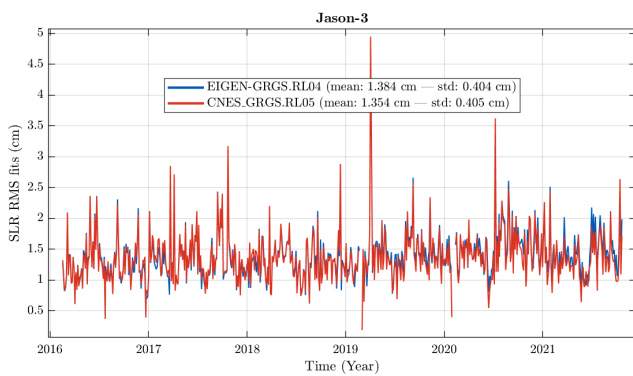


Figure 64: SLR RMS fits of Jason-3 orbits (left) and their differences (right) derived using the EIGEN-GRGS.RL04 and CNES_GRGS.RL05 gravity field models.

5.3 Earth's gravity field models

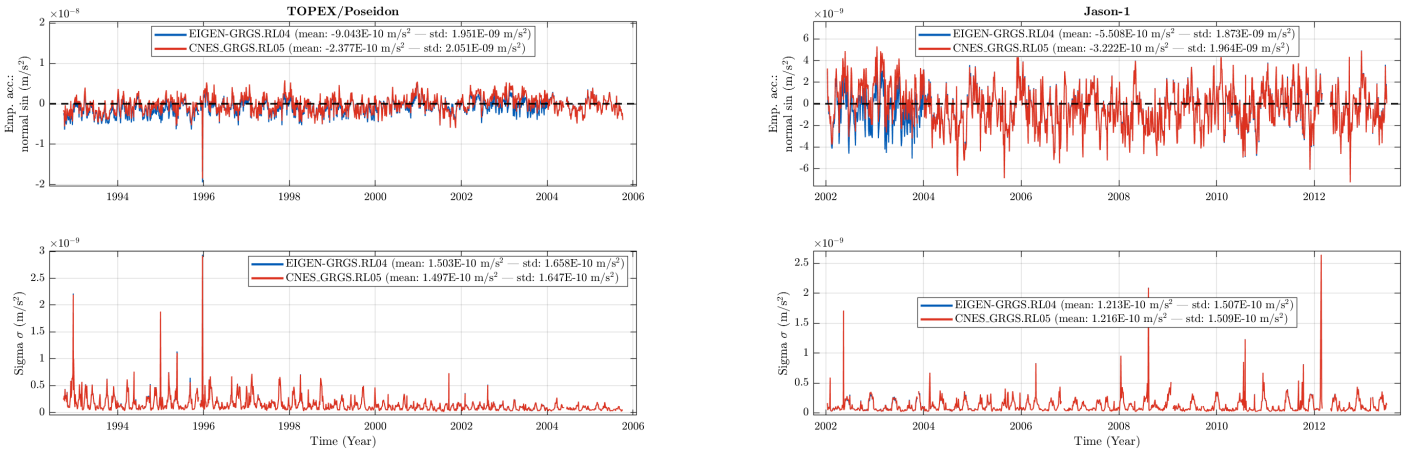


Figure 65: Empirical acceleration: amplitude of the normal sine term and its a posteriori standard deviation of TOPEX/Poseidon orbit (left) and Jason-1 orbit (right) derived using the EIGEN-GRGS.RL04 and CNES_GRGS.RL05 gravity field models.

The observed behavior in the periods 2002.0-2004.0 and 2016.5-2018.5 is also reflected in the SLR station range biases obtained with the 2 models. Figures 66 through 69 show the Yarragadee station range biases and the differences of the range biases estimated for the 4 satellites using the 2 gravity field models. For the case of TOPEX/Poseidon (Figure 66) and Jason-1 (Figure 67), an increased scatter of the range bias differences is observed between 2002 and 2004. The amplitude of the mean of the range biases for TOPEX/Poseidon is larger with RL05 than with RL04, whereas the mean is equal for the case of Jason-1. Figure 68 illustrates the largest deviations when using the 2 gravity field models for the period 2016.5-2018.5, where the RL05 model provides a lower amplitude of the mean value. Finally, for Jason-3 (Figure 69), a reduction of 3 mm in the SLR station range biases is clearly visible when using RL05 as compared to RL04.

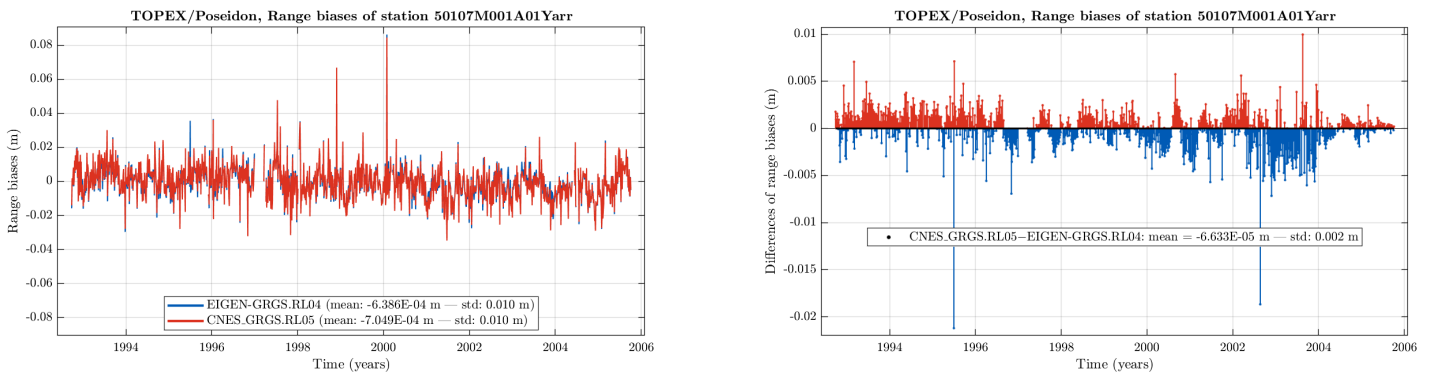


Figure 66: Yarragadee SLR station range biases (left) and their differences (right) derived for TOPEX/Poseidon orbits using the EIGEN-GRGS.RL04 and CNES_GRGS.RL05 gravity field models.

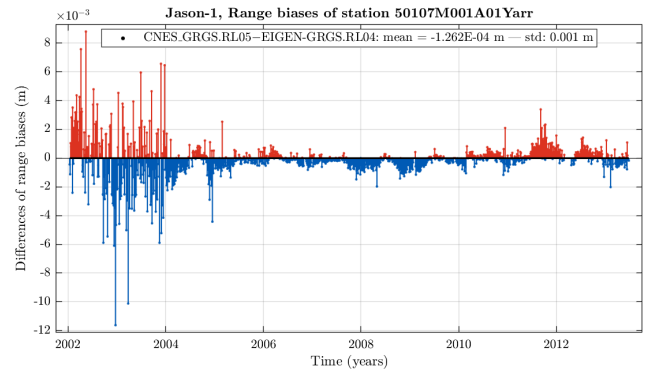
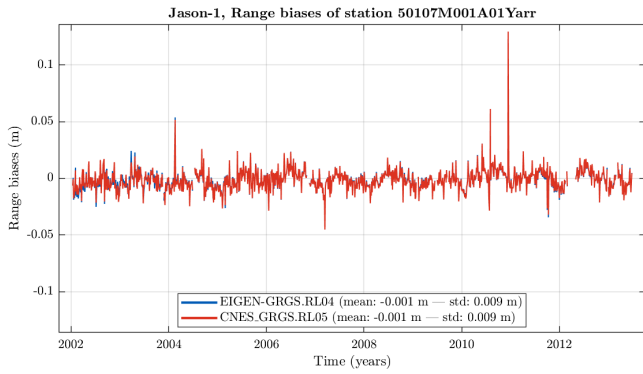


Figure 67: Yarragadee SLR station range biases (left) and their differences (right) derived for Jason-1 orbits using the EIGEN-GRGS.RL04 and CNES_GRGS.RL05 gravity field models.

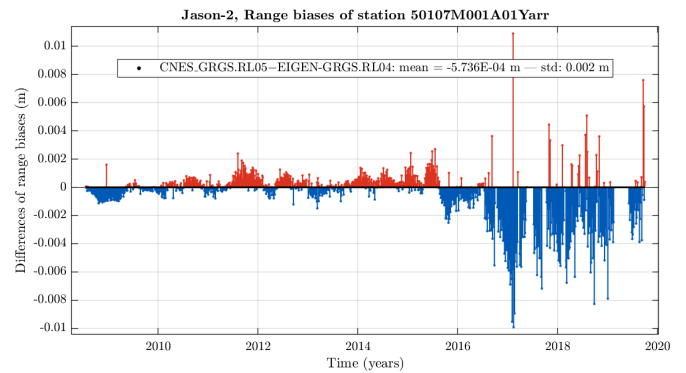
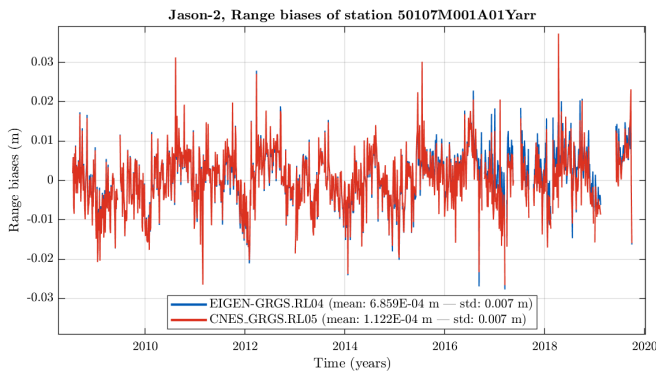


Figure 68: Yarragadee SLR station range biases (left) and their differences (right) derived for Jason-2 orbits using the EIGEN-GRGS.RL04 and CNES_GRGS.RL05 gravity field models.

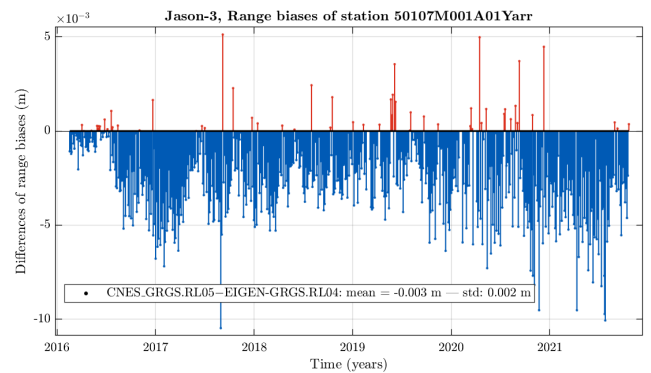
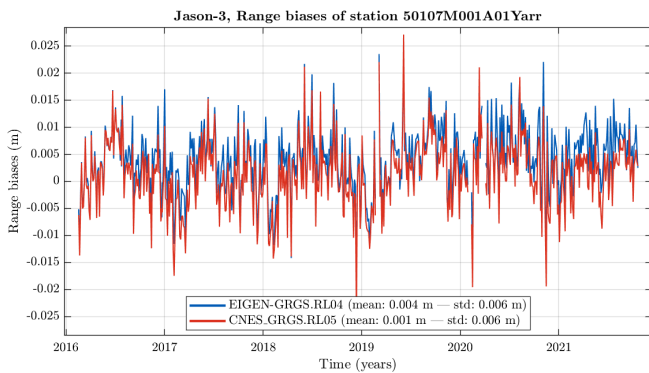


Figure 69: Yarragadee SLR station range biases (left) and their differences (right) derived for Jason-3 orbits using the EIGEN-GRGS.RL04 and CNES_GRGS.RL05 gravity field models.

The impact of the 2 models on the orbits of altimetry satellites can also be assessed by computing the orbit differences, specifically in the radial direction. Hence, the 2 orbits computed with the 2 models are compared using the MATLAB orbit comparison script (cf. Section 4.1). Figures 70 and 71 illustrate arc-wise standard deviations of the orbit differences in the radial direction for all 4

5.3 Earth's gravity field models

satellites. The mean of the standard deviations is around 0.4 cm for TOPEX/Poseidon, 0.2 cm for Jason-1, 0.3 cm for Jason-2, and 0.7 cm for Jason-3. The figures show a noticeable behavior in the periods discussed earlier. In Figure 70, an offset at 2004.0 is distinguished, this is the time when the data from GRACE satellites started to be derived accurately after the start of the mission in 2002. Similarly, Figure 71 shows an increase in the orbit differences after the retirement of the GRACE satellite mission in mid-2016. In addition, a linear trend is detected after mid-2016 for Jason-3 due to employing GRACE-FO data after 2018.5 in the derivation of the new model (RL05), whereas using extrapolation techniques during this period for the derivation of the old model (RL04).

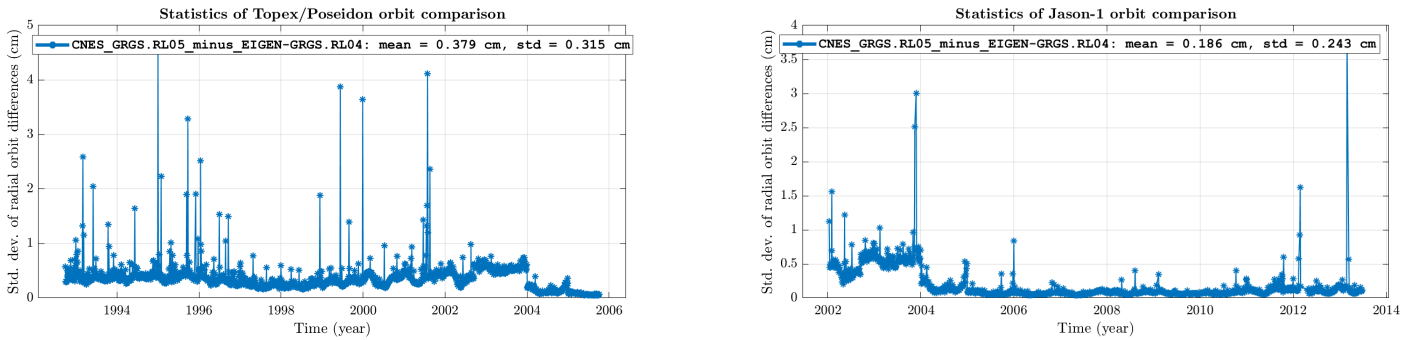


Figure 70: Standard deviations of orbit differences in the radial direction of TOPEX/Poseidon (left) and Jason-1 (right) satellites.

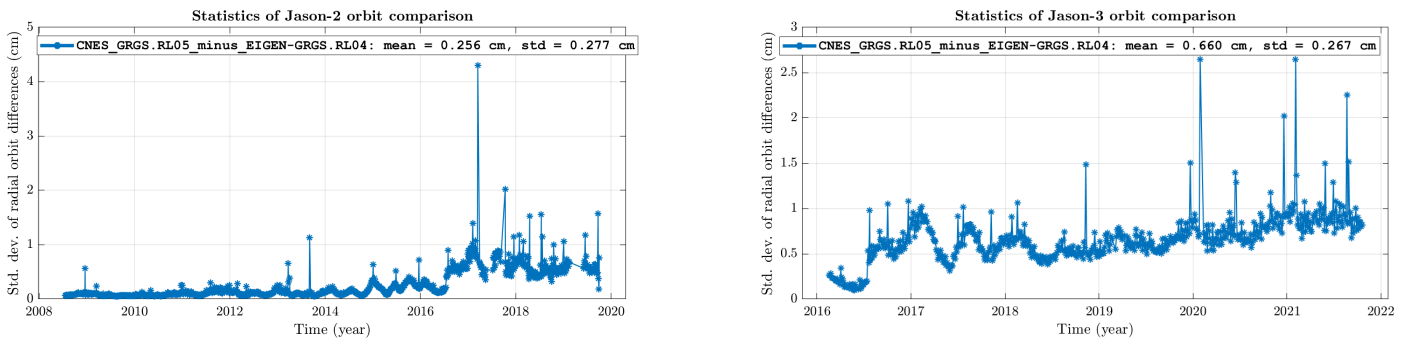


Figure 71: Standard deviations of orbit differences in the radial direction of Jason-2 (left) and Jason-3 (right) satellites.

Another study is performed on the orbit differences in terms of their geographical distribution and spectral behavior. Figures 72 and 73 illustrate the geographical distribution of the radial orbit differences of TOPEX/Poseidon and Jason satellites over a $1^\circ \times 1^\circ$ grid of latitude and longitude along the entire mission time spans. The range of the differences is between -1.5 and 1.5 cm, where it is seen that it reaches the maximum values in the case of Jason-3. This is explained by the fact that the largest differences are in the period of Jason-3 (between 2016.5 and 2021.8). Furthermore, a dipole behavior is observed between the east and the west of the world map, this is also observed in the assessment of the radial drift of TOPEX/Poseidon by the developing group (Lemoine et al., 2023).

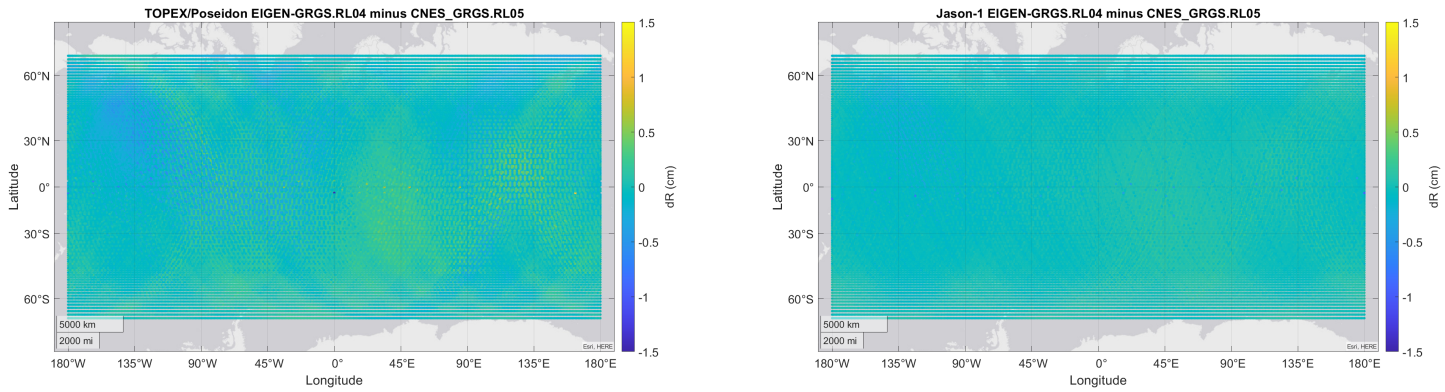


Figure 72: Geographical distribution of orbit differences in the radial direction of TOPEX/Poseidon (left) and Jason-1 (right) satellites averaged over a $1^\circ \times 1^\circ$ grid of latitude and longitude.

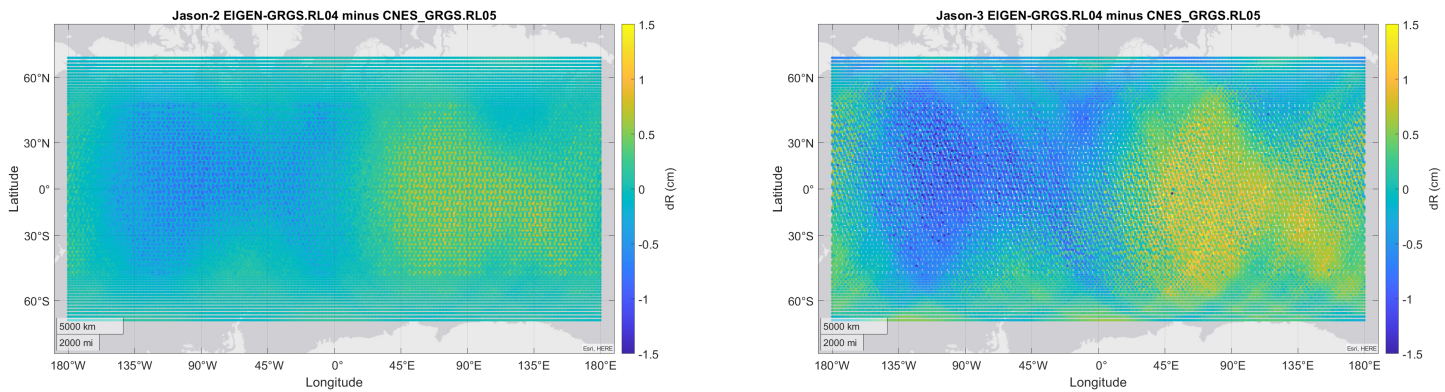


Figure 73: Geographical distribution of orbit differences in the radial direction of Jason-2 (left) and Jason-3 (right) satellites averaged over a $1^\circ \times 1^\circ$ grid of latitude and longitude.

In order to learn about the prominent periods and the amplitudes of the orbit differences, a spectral analysis is performed as discussed in Section 4.2. For this aim, outliers larger than the 5 sigma value are excluded, where the limit is defined as in Eq. 4.1. The wavelet transform is used to detect the periods arising in the problematic time spans discussed earlier, specifically between 2002.0 and 2004.0 and between 2016.5 and 2018.5. Figures 74 and 75 visualize the results of the wavelet transform of the radial orbit differences for all 4 satellites. In Figure 74, the time span between 2002.7 and 2005.8 is studied for TOPEX/Poseidon and Jason-1. The magnitude of the differences at around the revolution period (112.54 minutes) is approximately 1 cm and lasts for 400 days and continues in a lower magnitude until 800 days, then starts to disappear by 1000 days, that is by 2005. Another period that appears to be only in the time between 2002 and 2004 is at approximately 6 hours with a magnitude of around 0.4 cm. This period might be due to the combination of the revolution periods of the SLR and DORIS satellites that are used in the processing of the gravity field model. In Figure 75, the time span between 2016.5 and 2019.8 is studied for Jason-2 and Jason-3. The most prominent period is, as with the other satellites, at around 112.54 minutes. The magnitude of the orbit differences reaches 1 cm at this period which starts to increase after the day 200, that is at the end of 2016, and continues until the end of the tested time series.

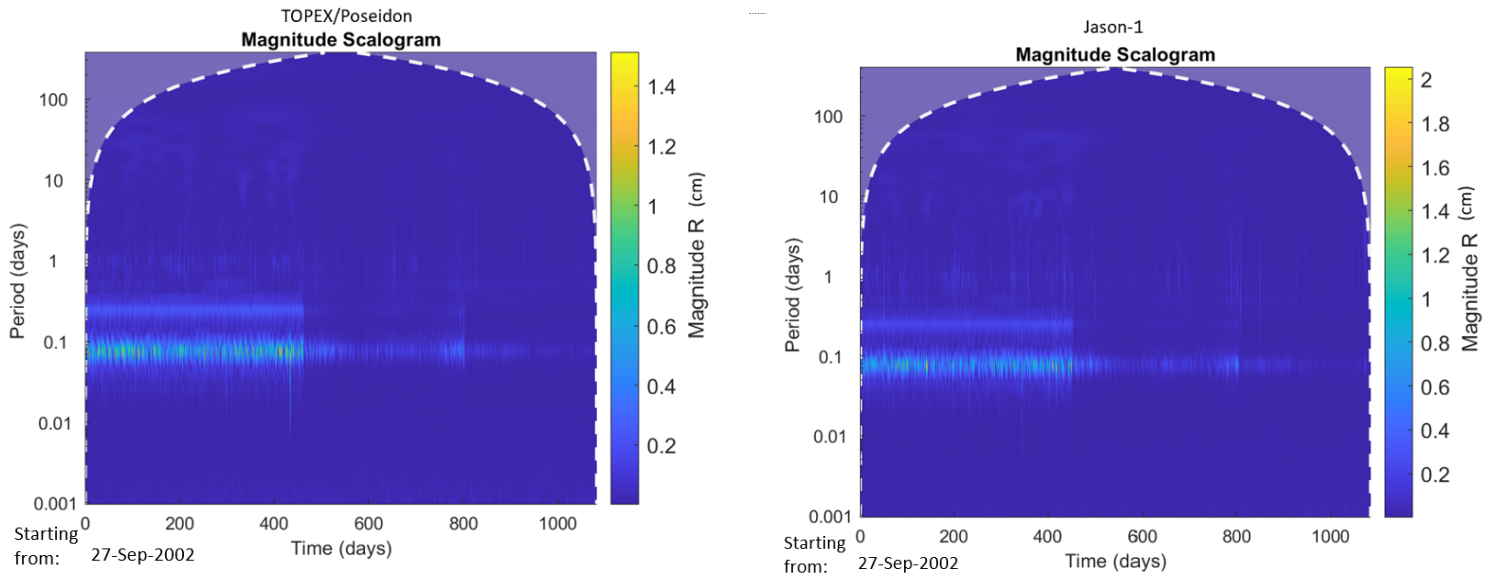


Figure 74: Magnitude scalogram of the wavelet transform over the time span between 2002.7 and 2005.8 of the TOPEX/Poseidon (left) and Jason-1 (right) orbit differences.

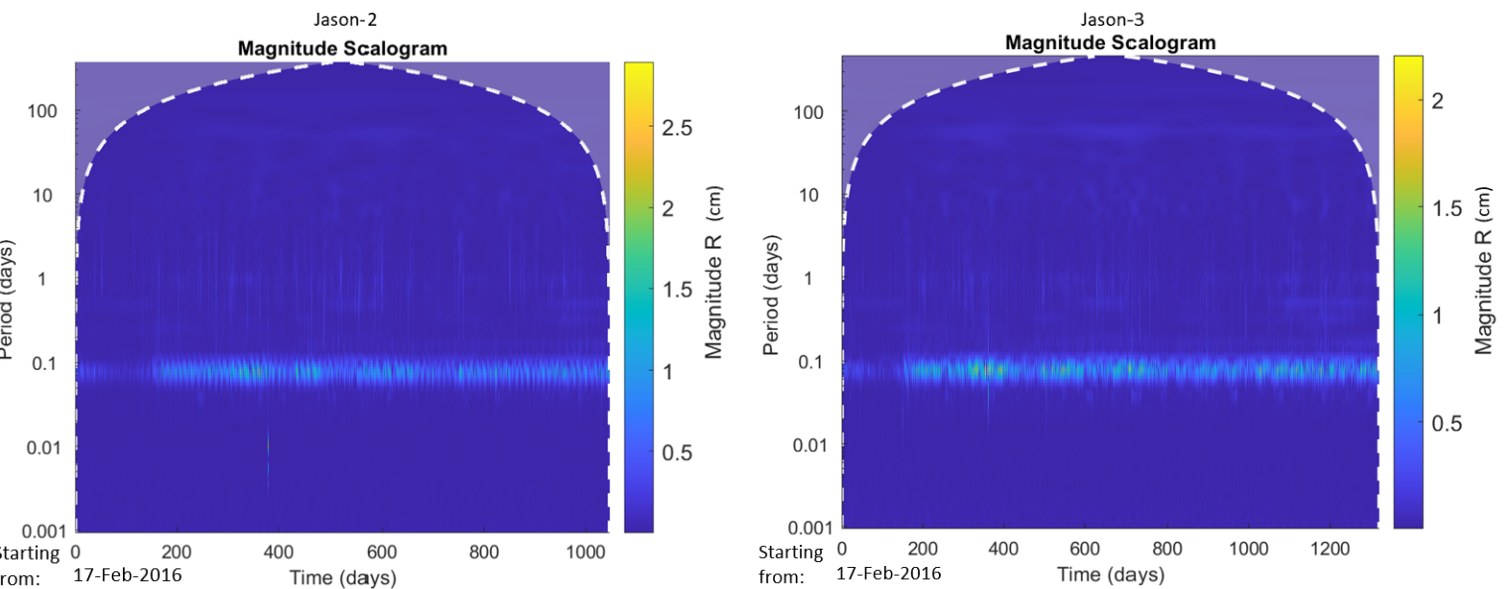


Figure 75: Magnitude scalogram of the wavelet transform over the time span between 2016.5 and 2019.8 of the Jason-2 (left) and Jason-3 (right) orbit differences.

As a final study, the Lomb-Scargle periodogram (Section 4.2.2) is used for the spectral analysis of the entire time spans of the 4 missions. Figures 76 and 77 visualize the radial orbit differences (on the top) and their spectral behavior in the logarithmic timescale. The highest amplitudes of the orbit differences in the radial direction can be observed clearly in the figures. These are 0.14 cm for TOPEX/Poseidon, 0.05 cm for Jason-1, 0.06 cm for Jason-2, and 0.41 cm for Jason-3. These maximum amplitudes are recovered at the period of approximately 100 minutes, which is close to 112.54 minutes of the orbital revolution period. The maximum amplitude obtained over the whole mission using the Lomb-Scargle periodogram is lower as compared to the amplitude (magnitude) obtained over the studied time span with the wavelet transform, which reaches up to 1.4 cm for

TOPEX/Poseidon and 2 cm for the 3 Jason missions. Other periods, such as 6 hours and half of the draconitic period 58 days are also detected with the Lomb-Scargle periodogram and can be distinguished in the figures as small peaks with amplitudes lower than 0.3 mm. The reason behind the difference between the recovered amplitudes from the 2 methods is that the Lomb-Scargle periodogram does not take into account the evolutionary signal, as it was proven in Section 4.2, and averages the amplitude over the whole time series, which results in smaller amplitudes than the real value.

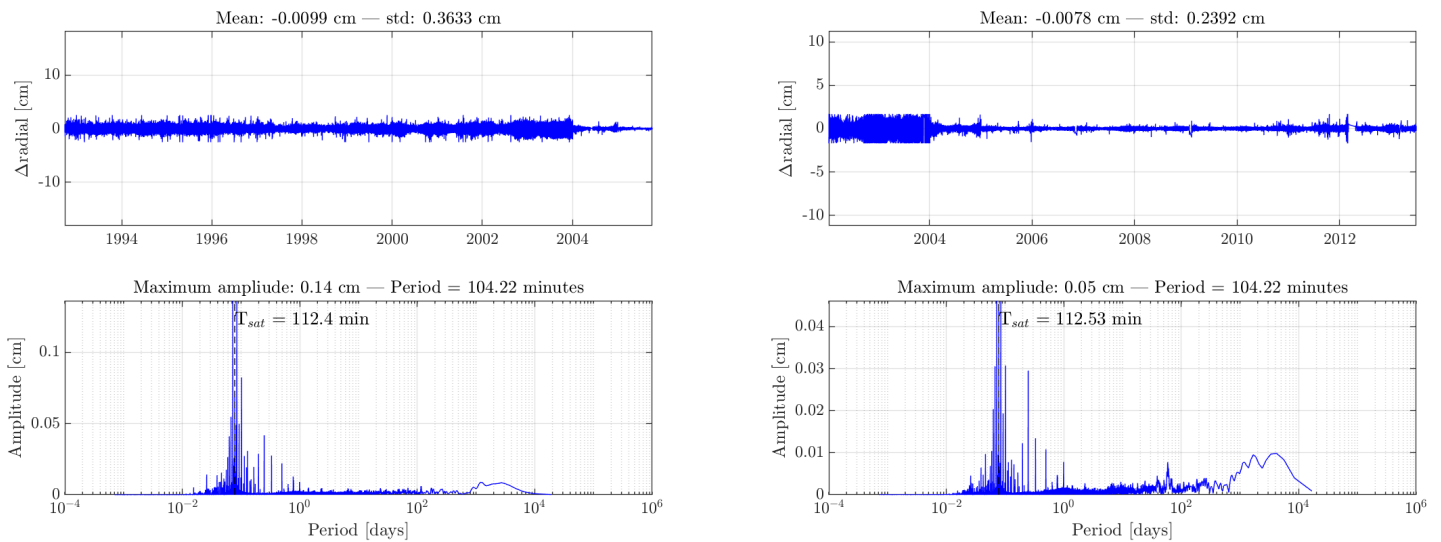


Figure 76: Radial orbit differences (top) of TOPEX/Poseidon (left) and Jason-1 (right) and their spectral analysis results using the Lomb-Scargle periodogram (bottom).

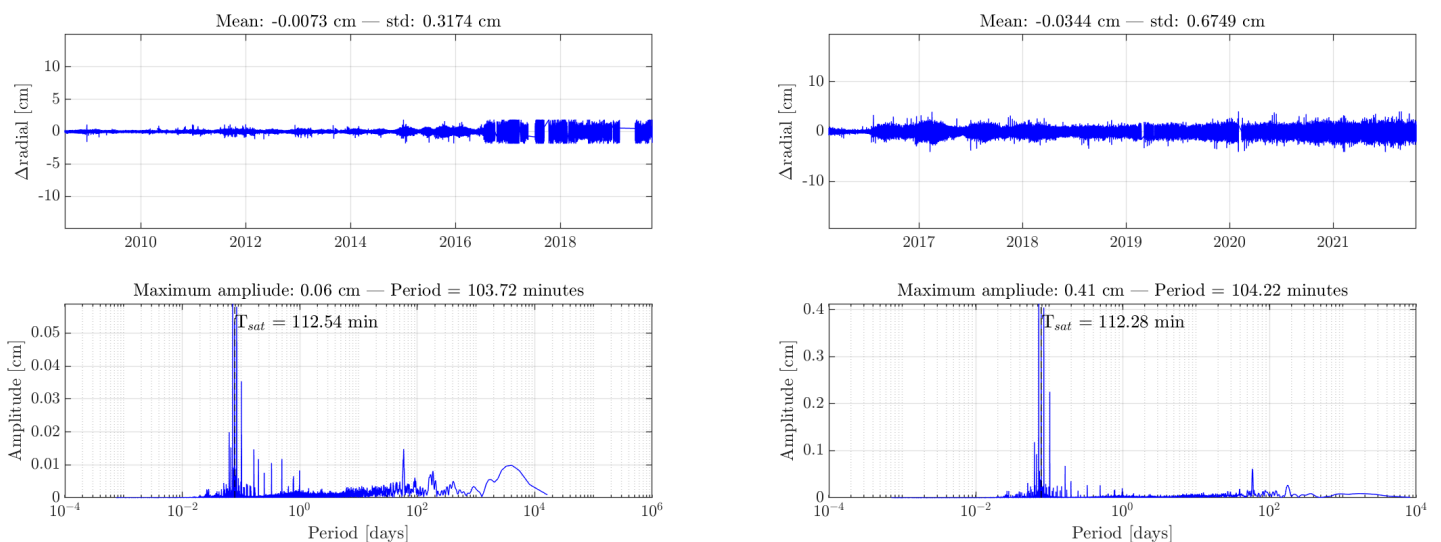


Figure 77: Radial orbit differences (top) of Jason-2 (left) and Jason-3 (right) and their spectral analysis results using the Lomb-Scargle periodogram (bottom).

In conclusion, the new Earth's mean gravity field model (RL05) provides improved performance over the older version (RL04) between 1992 and 1998, between 2011 and 2016.5, and between

2018.5 and 2021.8. There are 2 main problematic periods where the scatter of the SLR RMS fit and also the empirical acceleration in the normal direction is increased, which are between 2002.0 and 2004.0 and between 2016.5 and 2018.5. Other parameters, such as the atmospheric drag, the solar radiation pressure, and the Earth's albedo scale factors do not show significant differences when changing the gravity field model. Some SLR station range biases are impacted at the millimeter level due to the replacement of the gravity model, such as the Yarragadee station. The impact on orbit differences in the radial direction reaches up to 0.7 cm on average for the Jason-3 satellite. However, for the defined problematic periods, it reaches up to 1 cm for all 4 satellites. The most prominent period with the maximum amplitude of the orbit differences is the revolution period, detected at around 100 minutes. Another period of 6 hours appeared in the time span between 2002 and 2004, which might be due to the combination of SLR and DORIS measurements in the derivation of the new gravity field model. Therefore, careful revision of the combination of SLR and DORIS measurements used in the derivation of the new gravity field model and the extrapolation methods used in the period between 2016.5 and 2018.5 when there was no GRACE and GRACE-FO data is suggested.

6. Conclusions

This thesis is divided into 3 main tasks that aim to enhance the current analysis techniques of the altimetry satellite orbits and to investigate the impact of the new background models on the orbits of these satellites. The analysis of the altimetry satellite orbits has an important role in improving the orbit accuracy since it allows a validation of the orbit solutions and provides feedback on where improvements can be made. In most cases, the compared orbit solutions derived by external institutions do not have common time instants and step sizes. Therefore, an essential step in the analysis of these orbit solutions is the interpolation of the satellite positions at the desired time instants. The thesis explored 4 different interpolation methods, namely, the Lagrange, Newton, Hermite, and spline methods. First, the choice of the interpolation order is examined on the Newton method. For the orbit differences application, the order depends on the step sizes of the solutions. Higher order of interpolation, i.e. 6, 7, or 8, can provide the most accurate results within the middle interval of the tested time window. The standard deviation is used as a measure of the accuracy of the interpolation method. In the radial direction, the accuracy is found to be between 0.27 mm and 0.32 mm for a window size of 7 to 9 points. Over the entire orbit interval, the best interpolation results are provided by the 8th order Hermite interpolation with an accuracy of 0.34 mm in the radial direction using the sliding window approach and the middle-point approach. However, although Hermite interpolation proved to be faster than the Lagrange and Newton methods, the spline interpolation method is the fastest among all the other tested methods. Therefore, if the speed of the computation is more important than the accuracy, it is recommended to use the middle-point spline interpolation with unified step sizes. The standard deviation in the radial direction by the middle-point spline interpolation is 0.46 mm.

The second task is to investigate the spectral analysis methods for detecting dominant frequencies and periodicities and estimating the amplitudes of the orbit differences. Since the orbits are subject to orbit maneuvers, gaps, and other influences, the choice of the spectral analysis method is crucial. The standard fast Fourier transform, the zero-padding fast Fourier transform, the Lomb-Scargle periodogram, and the wavelet transform are studied. An artificial "sine" signal is used for the purpose of testing the methods. Since the Lomb-Scargle method is designed for non-uniformly sampled data, it outperforms the standard and the zero-padding fast Fourier transform when the signal contains gaps and noise, which is mostly the case in the orbit analysis application. The maximum deviation from the intended values using the Lomb-Scargle method can reach up to 0.5% in the period and up to 4% in the amplitude reconstruction. The zero-padding and the standard fast Fourier transform methods show variations of the reconstructed periods of 5% and 7% and amplitudes of 41% and 53%, respectively. Therefore, for the spectral analysis of orbit differences, the Lomb-Scargle method is recommended. On the other hand, when the orbit differences signal is not stable over time due to factors such as attitude variations, the wavelet transform is the optimal method for detecting periods and amplitudes in such a signal. When excluding the time series of the signal that include gaps, the relative accuracy of 2.4% of the period and 2% of the amplitude reconstruction is obtained. However, the wavelet transform is time and memory-consuming, there-

fore, it is suggested to use it for shorter time spans than using the Lomb-Scargle periodogram over the entire time span of the mission. This can help to understand the behavior of the signal over the time series, then make exact conclusions from the Lomb-Scargle method.

The final task is to study the impact of the new thermospheric density model (NRLMSIS 2.0) compared to the older version (NRLMSISE-00) and the new Earth's mean gravity field (CNES_-GRGS.RL05MF_combined_GRACE_SLR_DORIS) compared to the older release (EIGEN-GRGS.-RL04.MEANFIELD) on the orbits of altimetry satellites. Orbits of TOPEX/Poseidon and the first 3 missions of the Jason series are computed with DOGS-OC program in order to have a full picture of the impact of the new models over the time series between September 1992 (when TOPEX/Poseidon mission began) and October 2021 (until the availability of Jason-3 solutions). Similar parametrization is defined, and the same background models are used except for the models in comparison.

Within the investigation on the thermospheric density models, one should be careful in the choice of the orbit parameters to be estimated. Since the impact of the atmospheric drag is the largest in the transverse direction, the following question was posed: does the estimation of the empirical acceleration in the transverse component increase or decrease the accuracy of the comparison?

The answer depends on the goal of the study. If the goal is to assess the impact on the atmospheric drag scale factor, it is better not to estimate the polygon terms and only the periodic terms of the empirical acceleration in the transverse direction for 2 reasons. First, a high correlation between the polygons of the atmospheric drag scale factor and the empirical acceleration in the transverse component is found. Second, the uncertainty of the atmospheric drag scale factor is lowest when estimating only the periodic terms. On the other hand, if the goal is to assess the impact on the solar radiation scale factor and Earth's albedo scale factor, only estimating the polygon terms is suggested, as there is a high correlation between the solar radiation scale factor and the periodic terms, and the uncertainty for the cases in the solar radiation scale factor and Earth's albedo scale factor is the lowest when only estimating the polygon terms of the empirical acceleration in the transverse direction.

Finally, since the basic goal of the thesis is to study the impact on the final accuracy of the orbits, it is proven that one should estimate all the parameters in order to obtain the highest orbit accuracy. When comparing the 2 thermospheric density models based on their impact on the orbit parameters, the 2 models produced relatively similar results with a maximum relative difference of 0.4% of the mission SLR RMS fits. The impact on the orbit differences in the radial direction does not exceed 1 mm. The similar behavior of the 2 models might be explained by the fact that the satellites are orbiting in altitudes around 1300 km and NRLMSIS 2.0 is extensively focused for lower altitudes (Emmert et al., 2021). In conclusion, both models can be used for POD of altimetry satellites and produce similar accuracy.

The last investigation is on the new CNES/GRGS release of the Earth's mean gravity field (RL05). An improved performance is found for the new release (RL05) over the older version (RL04) between 1992 and 1998, between 2011 and 2016.5, and between 2018.5 and 2021.8. There are 2 main problematic periods where the scatter of the SLR RMS fit and also the empirical acceleration

in the normal direction is increased, which are between 2002.0 and 2004.0 and between 2016.5 and 2018.5. This might be explained by the different extrapolation methods that were implemented in the 2 models when no GRACE and GRACE-FO data was available and due to using the SLR and DORIS data together in the new release. Other orbit parameters are not significantly affected by the replacement of the model. However, some SLR station range biases are impacted at the millimeter level due to the replacement of the gravity model, such as of the Yarragadee station. In addition, the impact on orbit differences in the radial direction can reach up to 0.7 cm on average for the Jason-3 satellite. It can reach up to 1 cm for all 4 satellites for the defined problematic periods. Lomb-Scargle periodogram and wavelet transform are applied to the orbit differences. The revolution period is the most prominent period with the maximum amplitude of the orbit differences. Another period of 6 hours appeared in the time span between 2002 and 2004. As a conclusion of this investigation, careful revision of the combination of SLR and DORIS measurements used in the derivation of the new gravity model and the extrapolation methods used in the period between 2016.5 and 2018.5 when there was no GRACE data is suggested.

All in all, the outcomes of the thesis are as follows:

1. The 8^{th} order Hermite or the middle-point spline interpolation methods are suggested to be used for the interpolation of the satellite coordinates of the orbit solutions, according to the speed and accuracy requirement.
2. For the spectral analysis of the orbit differences, the Lomb-Scargle periodogram and wavelet transform can be used by taking care of the length of the time span when using the wavelet transform method.
3. The 2 thermospheric density models (NRLMSISE-00 and NRLMSIS 2.0) provide similar orbit accuracy.
4. The new CNES/GRGS release of Earth's mean gravity field model (RL05) brings a 2% improvement of RMS fits of SLR observations of the Jason-3 orbit as compared to RL04. However, further investigation on the extrapolation methods used at the periods without data from GRACE and GRACE-FO satellites is suggested.

List of Abbreviations

AU	Astronomical Unit	12
BIH	Bureau International de l'Heure	5
CHAMP	Challenging Minisatellite Payload	8
CNES	Centre National D'Etudes Spatiales	1, 2, 8, 76, 90, 91
DGFI-TUM	Deutsches Geodätisches Forschungsinstitut der Technischen Universität München	2, 6, 18, 41, 57
DOGS	DGFI Orbit and Geodetic Parameter Estimation Software	57
DOGS-OC	Orbit Computation library of DOGS	2, 18, 57, 90
DORIS	Doppler Orbitography and Radiopositioning Integrated by Satellite	1, 3, 4, 5, 6, 8, 9, 57, 76, 77, 85, 88, 91
DTM	Drag Temperature Model	12
ECV	Essential Climate Variables	1
EIGEN	European Improved Gravity model of the Earth by New techniques	8, 9
EOP	Earth Orientation Parameters	4
ERS	European Remote Sensing satellite	1
GCOS	Global Climate Observing System	1
GEOS	Geodynamic Experimental Ocean Satellite	1
GMSL	Global Mean Sea Level	6
GNSS	Global Navigation Satellite System	1, 3, 6
GOCE	Gravity field and Ocean Circulation Explorer	8, 76
GPS	Global Positioning System	2, 3, 8, 14, 15, 16, 17, 18, 77
GRACE	Gravity Recovery and Climate Experiment	8, 9, 76, 77, 84, 88, 91
GRACE-FO	Gravity Recovery and Climate Experiment Follow On	76, 77, 88, 91

GRGS	Groupe de Recherche de Géodésie Spatiale	I, 2, 77, 90, 91
IERS	International Earth Rotation and Reference Systems Service	5, 6, 10
IGN	Institute Nationale de l'Information Géographique et Forestière	6
IGS	International GNSS Service	77
ISR	Incoherent Scatter Radar	58
ITRS	International Terrestrial Reference System	2, 3, 4, 5, 6
JPL	Jet Propulsion Laboratory	6, 8
LAGEOS	LAser GEOdynamic Satellite	8, 76
LEO	Low Earth Orbit	3, 8, 76
LIDAR	Light Detection and Ranging	59
MSIS	Mass Spectrometer Incoherent Scatter	2, 12, 58
NASA	National Aeronautics and Space Administration	1
NRL	Naval Research Laboratory	2
NTL	Non-Tidal Loading	6
POD	Precise Orbit Determination	IV, XIII, 1, 2, 3, 4, 5, 6, 10, 11, 12, 13, 57, 63, 69, 70, 71, 72, 73, 78, 79, 80, 81, 90
PRARE	Precise Range and Range Rate Equipment	1
RMS	Root Mean Square	VIII, IX, X, 6, 8, 10, 16, 58, 59, 61, 63, 64, 68, 69, 70, 71, 72, 73, 77, 78, 79, 80, 81, 88, 90, 91
RTN	Radial, Transverse, and Normal	VI, VII, 19, 21, 31, 34, 35, 36, 41
SI	Système International d'Unités (International System of Units)	5

List of Abbreviations

SLR	Satellite Laser Ranging	VIII, IX, X, 1, 2, 3, 4, 5, 6, 8, 9, 10, 57, 58, 59, 61, 63, 64, 68, 69, 70, 71, 72, 73, 76, 77, 78, 79, 80, 81, 82, 83, 85, 88, 90, 91
SST	Satellite to Satellite Tracking	8
STARLETTE	Satellite de Taille Adaptée avec Réflecteurs Laser pour les Études de la Terre	8, 76
STD	Standard Deviation	19
TAI	Temps Atomique International (English: International Atomic Time)	V, VI, 19, 20, 21, 23, 24, 25, 26, 27, 28
TDRSS	Tracking and Data Relay Satellite System	1
TOPEX	TOPography EXperiment	I, VI, VII, X, XI, XIII, 1, 3, 5, 8, 13, 18, 31, 34, 35, 36, 68, 70, 77, 78, 82, 84, 85, 86, 87, 90
USO	Ultra-Stable Oscillator	5
UTC	Temps universel coordonné (English: Coordinated Universal Time)	19, 21, 25
VLBI	Very Long Baseline Interferometry	3

Bibliography

- Arnold, D., Montenbruck, O., Hackel, S., and Sośnica, K. (2019). Satellite laser ranging to low earth orbiters: orbit and network validation. *Journal of Geodesy*, 93(11):2315–2334. doi: 10.1007/s00190-018-1140-4.
- Beutler, G. (2005). *Methods of Celestial Mechanics*, volume 1. Springer, Berlin Heidelberg. <https://doi.org/10.1016/C2013-0-08160-1>.
- Biancale, R. and Bode, A. (2006). Mean annual and seasonal atmospheric tide models based on 3-hourly and 6-hourly ECMWF surface pressure data. (scientific technical report STR ; 06/01). *Deutsches GeoForschungsZentrum GFZ*, (33 S. p.). <https://doi.org/10.2312/GFZ.b103-06011>.
- Bloßfeld, M. (2015). *The key role of Satellite Laser Ranging towards the integrated estimation of geometry, rotation and gravitational field of the Earth*. PhD thesis, Technical University of Munich, and Reihe C der Deutschen Geodätischen Kommission, Munich, Germany.
- Bowman, B., Tobiska, W. K., Marcos, F., Huang, C., Lin, C., and Burke, W. (2008). A new empirical thermospheric density model JB2008 using new solar and geomagnetic indices. In *AIAA/AAS Astrodynamics Specialist Conference and Exhibit*. American Institute of Aeronautics and Astronautics. doi: 10.2514/6.2008-6438.
- Bruinsma, S. (2015). The DTM-2013 thermosphere model. *Journal of Space Weather and Space Climate*, 5:A1. <https://doi.org/10.1051/swsc/2015001>.
- Bruinsma, S., Lemoine, J.-M., Biancale, R., and Valès, N. (2010). CNES/GRGS 10-day gravity field models (release 2) and their evaluation. *Advances in Space Research*, 45(4):587–601. <https://doi.org/10.1016/j.asr.2009.10.012>.
- Bruinsma, S. L., Förste, C., Abrikosov, O., Marty, J.-C., Rio, M.-H., Mulet, S., and Bonvalot, S. (2013). The new ESA satellite-only gravity field model via the direct approach. *Geophysical Research Letters*, 40(14):3607–3612. <https://doi.org/10.1002/grl.50716>.
- Cerri, L., Berthias, J. P., Bertiger, W. I., Haines, B. J., Lemoine, F. G., Mercier, F., Ries, J. C., Willis, P., Zelensky, N. P., and Ziebart, M. (2010). Precision orbit determination standards for the Jason series of altimeter missions. *Marine Geodesy*, 33(sup1):379–418. doi: 10.1080/01490419.2010.488966.
- Couhert, A., Cerri, L., Legeais, J.-F., Ablain, M., Zelensky, N. P., Haines, B. J., Lemoine, F. G., Bertiger, W. I., Desai, S. D., and Otten, M. (2015). Towards the 1 mm/y stability of the radial orbit error at regional scales. *Advances in Space Research*, 55(1):2–23. <https://doi.org/10.1016/j.asr.2014.06.041>.
- Desai, S. D. (2002). Observing the pole tide with satellite altimetry. *Journal of Geophysical Research: Oceans*, 107(C11):7–1–7–13. <https://doi.org/10.1029/2001JC001224>.

- Doornbos, E. (2011). *Thermospheric density and wind determination from satellite dynamics*. PhD thesis, Technical University of Delft, Delft, Netherlands. Accessed: 2023-05-02 URL: <http://resolver.tudelft.nl/uuid:33002be1-1498-4bec-a440-4c90ec149aea>.
- Emmert, J. T., Drob, D. P., Picone, J. M., Siskind, D. E., Jones Jr., M., Mlynczak, M. G., Bernath, P. F., Chu, X., Doornbos, E., Funke, B., Goncharenko, L. P., Hervig, M. E., Schwartz, M. J., Sheese, P. E., Vargas, F., Williams, B. P., and Yuan, T. (2021). NRLMSIS 2.0: A whole-atmosphere empirical model of temperature and neutral species densities. *Earth and Space Science*, 8(3):e2020EA001321. <https://doi.org/10.1029/2020EA001321>.
- Esselborn, S., Rudenko, S., and Schöne, T. (2018). Orbit-related sea level errors for TOPEX altimetry at seasonal to decadal timescales. *Ocean Sci.*, 14(2):205–223. doi: 10.5194/os-14-205-2018.
- Feng, Y. and Zheng, Y. (2005). Efficient interpolations to GPS orbits for precise wide area applications. *GPS Solutions*, 9:273–282. doi: 10.1007/s10291-005-0133-y.
- Floberghagen, R., Fehring, M., Lamarre, D., Muzi, D., Frommknecht, B., Steiger, C., Piñeiro, J., and da Costa, A. (2011). Mission design, operation and exploitation of the gravity field and steady-state ocean circulation explorer mission. *Journal of Geodesy*, 85(11):749–758. doi: 10.1007/s00190-011-0498-3.
- Gruber, T. and Willberg, M. (2019). Signal and error assessment of GOCE-based high resolution gravity field models. *Journal of Geodetic Science*, 9(1):71–86. doi: 10.1515/jogs-2019-0008.
- Hedin, A. E. (1991). Extension of the MSIS thermosphere model into the middle and lower atmosphere. *Journal of Geophysical Research: Space Physics*, 96(A2):1159–1172. <https://doi.org/10.1029/90JA02125>.
- Hofmann-Wellenhof, B. and Moritz, H. (2006). *Physical Geodesy*. Springer, Vienna. doi: 10.1007/b139113.
- Hugentobler, U. (2020). Lecture notes in orbital mechanics. Module BGU61029 Introduction to Satellite Navigation and Orbit Mechanics.
- Jayles, C., Nhun-Fat, B., and Tourain, C. (2006). DORIS: System description and control of the signal integrity. *Journal of Geodesy*, 80(8):457–472. doi: 10.1007/s00190-006-0046-8.
- Kalicinsky, C., Reisch, R., Knieling, P., and Koppmann, R. (2020). Determination of time-varying periodicities in unequally spaced time series of OH* temperatures using a moving Lomb–Scargle periodogram and a fast calculation of the false alarm probabilities. *Atmospheric Measurement Techniques*, 13(2):467–477. doi: 10.5194/amt-13-467-2020.
- Karepova, E. D. and Kornienko, V. S. (2019). The comparison of several approaches to the interpolation of a trajectory of a navigation satellite. *IOP Conference Series: Materials Science and Engineering*, 537. doi: 10.1088/1757-899X/537/2/022054.
- Kaula, W. M. (1966). *Theory of satellite geodesy. Applications of satellites to geodesy*. Dover Publications, Mineola, New York.

- Knocke, P., Ries, J., and Tapley, B. (1988). Earth radiation pressure effects on satellites. In *Astrodynamics Conference*, pages 577–587. American Institute of Aeronautics and Astronautics. doi: 10.2514/6.1988-4292.
- Konopliv, A., Asmar, S., Carranza, E., Sjogren, W., and Yuan, D. (2001). Recent gravity models as a result of the lunar prospector mission. *Icarus*, 150(1):1–18. <https://doi.org/10.1006/icar.2000.6573>.
- Lemoine, J.-M., Biancale, R., Reinquin, F., Bourgogne, S., and Gégout, P. (2018). The new time-variable gravity field model for pod of altimetric satellites based on GRACE+SLR RL04 from CNES/GRGS. In *IDS Workshop*, Ponta Delgada, São Miguel Island, Azores Archipelago (Portugal). Accessed: 2023-04-25 URL: https://ids-doris.org/images/documents/report/ids_workshop_2018/IDS18_s3_LemoineJM_NewtimeVariableGravityFieldModelForPOD.pdf.
- Lemoine, J.-M., Biancale, R., Reinquin, F., Bourgogne, S., and Gégout, P. (2019). CNES/GRGS RL04 Earth gravity field models, from GRACE and SLR data. *GFZ Data Services*. <https://doi.org/10.5880/ICGEM.2019.010>.
- Lemoine, J.-M., Bourgogne, S., Reinquin, F., and Capdeville, H. (2023). New mean gravity field model CNES_GRGS.RL05MF_combined_GRACE_SLR_DORIS. In *IDS AWG*, Online. Accessed: 2023-04-25 URL: <https://ids-doris.org/images/documents/report/AWG202304/IDSAWG202304-LemoineJM-NewMeanGravityModel.pdf>.
- Lerch, F., Nerem, R., Putney, B., Felsentreger, T., Sanchez, B., Klosko, S., Patel, G., Williamson, R., Chinn, D., Chan, J., Rachlin, K., Chandler, N., McCarthy, J., Marshall, J., Luthcke, S., Pavlis, D., Robbins, J., Kapoor, S., and Pavlis, E. (1992). Geopotential models of the earth from satellite tracking, altimeter and surface gravity observations: GEM-T3 and GEM-T3S. Technical Report NASA Technical Memorandum 104555, NASA, Goddard Space Flight Center Greenbelt, MD.
- Love, A. E. H. (1909). The yielding of the earth to disturbing forces. *Proceedings of the Royal Society of London. Series A, Containing Papers of a Mathematical and Physical Character*, 82(551):73–88. doi: 10.1098/rspa.1909.0008.
- Luthcke, S. B., Zelensky, N. P., Rowlands, D. D., Lemoine, F. G., and Williams, T. A. (2003). The 1-centimeter orbit: Jason-1 precision orbit determination using GPS, SLR, DORIS, and altimeter data special issue: Jason-1 calibration/validation. *Marine Geodesy*, 26(3-4):399–421. doi: 10.1080/714044529.
- Matzka, J., Stolle, C., Yamazaki, Y., Bronkalla, O., and Morschhauser, A. (2021). The geomagnetic Kp index and derived indices of geomagnetic activity. *Space Weather*, 19(5):e2020SW002641. <https://doi.org/10.1029/2020SW002641>.
- Montenbruck, O. and Gill, E. (2000). *Satellite Orbits: Models, Methods and Applications*. Springer, Berlin, Heidelberg, 1st edition. <https://doi.org/10.1007/978-3-642-58351-3>.
- Nerem, R., Putney, B., Marshall, J., Lerch, F., Pavlis, E., Klosko, S., Luthcke, S., Patel, G., Williamson, R., and Zelensky, N. (1993). Expected orbit determination performance for the

- topex/poseidon mission. *IEEE Transactions on Geoscience and Remote Sensing*, 31(2):333–354. doi: 10.1109/36.214910.
- Neta, B., Clynch, J., Danielson, D., and Sagovac, C. (1996). Fast interpolation for global positioning system (GPS) satellite orbits. In *Proceedings of AIAA/AAS astrodynamics specialist conference*. AIAA/AAS, San Diego. Accessed: 2023-05-05 URL: <http://faculty.nps.edu/bneta/papers/interp.pdf>.
- Panzetta, F., Bloßfeld, M., Erdogan, E., Rudenko, S., Schmidt, M., and Müller, H. (2019). Towards thermospheric density estimation from SLR observations of LEO satellites: a case study with ANDE-Pollux satellite. *Journal of Geodesy*, 93(3):353–368. doi: 10.1007/s00190-018-1165-8.
- Petit, G. and Luzum, B. (2010). IERS Conventions (2010). *IERS Technical Note*, 36:1.
- Picone, J. M., Hedin, A. E., Drob, D. P., and Aikin, A. C. (2002). NRLMSISE-00 empirical model of the atmosphere: Statistical comparisons and scientific issues. *Journal of Geophysical Research: Space Physics*, 107(A12):SIA 15–1–SIA 15–16. <https://doi.org/10.1029/2002JA009430>.
- Reigber, C., Balmino, G., Schwintzer, P., Biancale, R., Bode, A., Lemoine, J.-M., König, R., Loyer, S., Neumayer, H., Marty, J.-C., Barthelmes, F., and Perosanz, F. (2002). A high-quality global gravity field model from CHAMP GPS tracking data and accelerometry (EIGEN1S). *Geophysical Research Letters*, 29:37–1. doi: 10.1029/2002GL015064.
- Rosborough, G. W. and Tapley, B. D. (1987). Radial, transverse and normal satellite position perturbations due to the geopotential. *Celestial mechanics*, 40(3):409–421. doi: 10.1007/BF01235855.
- Rudenko, S., Bloßfeld, M., Müller, H., Dettmering, D., Angermann, D., and Seitz, M. (2018). Evaluation of DTRF2014, ITRF2014, and JTRF2014 by precise orbit determination of SLR satellites. *IEEE Transactions on Geoscience and Remote Sensing*, 56(6):3148–3158. doi: 10.1109/TGRS.2018.2793358.
- Rudenko, S., Dettmering, D., Esselborn, S., Schöne, T., Förste, C., Lemoine, J.-M., Ablain, M., Alexandre, D., and Neumayer, K.-H. (2014). Influence of time variable geopotential models on precise orbits of altimetry satellites, global and regional mean sea level trends. *Advances in Space Research*, 54:92–118. doi: 10.1016/j.asr.2014.03.010.
- Rudenko, S., Dettmering, D., Zeitlhöfler, J., Alkahal, R., Upadhyay, D., and Bloßfeld, M. (2023). Radial orbit errors of contemporary altimetry satellite orbits. *Surveys in Geophysics*. doi: 10.1007/s10712-022-09758-5.
- Rudenko, S., Esselborn, S., Schöne, T., and Dettmering, D. (2019). Impact of terrestrial reference frame realizations on altimetry satellite orbit quality and global and regional sea level trends: a switch from ITRF2008 to ITRF2014. *Solid Earth*, 10(1):293–305. doi: 10.5194/se-10-293-2019.
- Rudenko, S., Neumayer, K. H., Dettmering, D., Esselborn, S., Schöne, T., and Raimondo, J. C. (2017). Improvements in precise orbits of altimetry satellites and their impact on mean sea level monitoring. *IEEE Transactions on Geoscience and Remote Sensing*, 55(6):3382–3395. doi: 10.1109/TGRS.2017.2670061.

- Savcenko, R. and Bosch, W. (2012). EOT11A – empirical ocean tide model from multi-mission satellite altimetry. *Deutsches Geodatisches Forschungsinstitut der Technische Universität München (DGFI-TUM)*, (Report no. 89). hdl: 10013/epic.43894.d001.
- Schenewerk, M. (2003). A brief review of basic GPS orbit interpolation strategies. *GPS solutions*, 6:265–267. <https://doi.org/10.1007/s10291-002-0036-0>.
- Seeber, G. (2003). *Satellite Geodesy*. Walter de Gruyter, 2nd edition. <https://doi.org/10.1515/9783110200089>.
- Seitz, M., Angermann, D., Bloßfeld, M., Drewes, H., and Gerstl, M. (2012). The 2008 DGFI realization of the ITRS: DTRF2008. *Journal of Geodesy*, 86:1097–1123. doi: 10.1007/s00190-012-0567-2.
- Song, C., Chen, H., Jiang, W., An, X., Chen, Q., and Li, W. (2021). An effective interpolation strategy for mitigating the day boundary discontinuities of precise GNSS orbit products. *GPS solutions*, 25:99. <https://doi.org/10.1007/s10291-021-01130-1>.
- Stammer, D. and Cazenave, A. (2017). *Satellite Altimetry over Oceans and Land Surfaces*. CRC Press Taylor and Francis Group, Boca Raton, London, New, 1st edition. <https://doi.org/10.1201/9781315151779>.
- Tapley, B. D., Bettadpur, S., Watkins, M., and Reigber, C. (2004). The gravity recovery and climate experiment: Mission overview and early results. *Geophysical Research Letters*, 31:9. L09607, <https://doi.org/10.1029/2004GL019920>.
- Tapley, B. D., Watkins, M. M., Ries, J. C., Davis, G. W., Eanes, R. J., Poole, S. R., Rim, H. J., Schutz, B. E., Shum, C. K., Nerem, R. S., Lerch, F. J., Marshall, J. A., Klosko, S. M., Pavlis, N. K., and Williamson, R. G. (1996). The joint gravity model 3. *Journal of Geophysical Research: Solid Earth*, 101(B12):28029–28049. <https://doi.org/10.1029/96JB01645>.
- Tavernier, G., Fagard, H., Feissel-Vernier, M., Bail, K. L., Lemoine, F., Noll, C., Noomen, R., Ries, J. C., Soudarin, L., Valette, J. J., and Willis, P. (2006). The international DORIS service: genesis and early achievements. *Journal of Geodesy*, 80(8):403–417. <https://doi.org/10.1007/s00190-006-0082-4>.
- Torrence, C. and Compo, G. P. (1998). A practical guide to wavelet analysis. *Bulletin of the American Meteorological Society*, 79(1):61–78. [https://doi.org/10.1175/1520-0477\(1998\)079<0061:APGTWA>2.0.CO;2](https://doi.org/10.1175/1520-0477(1998)079<0061:APGTWA>2.0.CO;2).
- Trauth, M. H. (2020). *MATLAB Recipes for Earth Sciences*. Springer Cham, 5th edition. <https://doi.org/10.1007/978-3-030-38441-8>.
- VanderPlas, J. T. (2018). Understanding the Lomb-Scargle periodogram. *The Astrophysical Journal Supplement Series*, 236(1):16. doi: 10.3847/1538-4365/aab766.
- Wang, J., Li, Y., Zhu, H., and Ma, T. (2018). Interpolation method research and precision analysis of GPS satellite position. *Journal of Systems Science and Information*, 6(3):277–288. doi: 10.21078/JSSI-2018-277-12.

- Willis, P., Jayles, C., and Bar-Sever, Y. (2006). DORIS: From orbit determination for altimeter missions to geodesy. *Comptes Rendus Geoscience*, 338(14):968–979. <https://doi.org/10.1016/j.crte.2005.11.013>.
- Wu, S.-C., Yunck, T. P., and Thornton, C. L. (1991). Reduced-dynamic technique for precise orbit determination of low earth satellites. *Journal of Guidance Control and Dynamics*, 14:24–30. <https://doi.org/10.2514/3.20600>.
- Yousif, H. and El-Rabbany, A. (2007). Assessment of several interpolation methods for precise GPS orbit. *Journal of Navigation*, 60(3):443–455. doi: 10.1017/S0373463307004250.
- Zechmeister, M. and Kurster, M. (2009). The generalised Lomb-Scargle periodogram - a new formalism for the floating-mean and keplerian periodograms. *A&A*, 496(2):577–584. doi: 10.1051/0004-6361:200811296.
- Zeithöfler, J. (2019). Nominal and observation-based attitude realization for precise orbit determination of the Jason satellites. Master's thesis, Technische Universität München, Munich, Germany.
- Zeithöfler, J., Bloßfeld, M., Rudenko, S., Dettmering, D., and Seitz, F. (2023). Station-dependent satellite laser ranging measurement corrections for TOPEX/Poseidon. *Advances in Space Research*, 71(1):975–996. <https://doi.org/10.1016/j.asr.2022.09.002>.
- Zheng, Y. and Zhang, J. (2020). Satellite orbit interpolation algorithm analysis for GNSS terminals. In Sun, J., Yang, C., and Xie, J., editors, *China Satellite Navigation Conference (CSNC) 2020 Proceedings: Volume III*, pages 310–321, Singapore. Springer Singapore. https://doi.org/10.1007/978-981-15-3715-8_29.

